PEOPLE'S DEMOCRATIC REPUBLIC OF ALGERIA
MINISTRY OF HIGHER EDUCATION AND SCIENTIFIC RESEARCH
ABOU BEKR BELKAID TLEMCEN UNIVERSITY

FACULTY OF TECHNOLOGY

THESIS

Presented for obtaining the degree of DOCTORATE 3rd Cycle LMD

In: automatic

Specialty: Automatic

BY: SAIDI FARAH

Theme

Conception of a surgery simulator

Supported on 19/09/2021, in front of the jury composed of:

Mr Mechernene Abdelkader	University of Tlemcen	MCA	President
Mr Tahour Ahmed	Tlemcen School of Applied Sciences	Professor	Examiner
Mr Djebbari Abdelghani	University of Tlemcen	Professor	Examiner
Mr Malti Abed	University of Tlemcen	MCA	Director

Contents

DEDICATION

I wish to express my profound gratitude and indebtedness to Dr **Abed Malti**, for introducing the present work and for his inspiring guidance, constructive criticism and valuable suggestion throughout this project.

To my colleague "Yasser" and "Malik" for their support.

To all my family (My parents, my sisters and my husband) who has patiently extended all sorts of help for accomplishing this work.

Lastly, to my darling son "Mohammed Yacine"

ACKNOWLEDGEMENT

Abstract

English

Surgical simulation involves making deformations and incisions on human organs. These simulators require fast and precise numerical calculation algorithms to perform deformations in real time. The deformations applied to the organs are nonlinear where these organs have hyperelastic mechanical characteristics. Therefore, the nonlinear deformation of hyperelastic tissues is the subject of extensive research. In this thesis, we propose a new technique to improve the speed and the precision of the nonlinear deformation algorithm. This technique is based on the modification of the classical Newton-Raphson method by a partially updated stiffness matrix. Proposed method has proven to have high convergence speed without losing precision. We provided sufficient conditions for the convergence of these algorithms by giving explicit upper limit constraints using the Kantorovich's theorem.

keywords: Nonlinear hyperelastic deformation; Mooney-Rivilin model; nonlinear finite element; Newton-Raphson method; Biomechanical modeling; Virtual reality; Surgical simulation.

Français

La simulation chirurgicale basée sur la réalité virtuelle nécessite des modèles de déformation en temps réel et précis pour un réalisme interactif. La déformation des tissus mous est généralement non-linéaire. Ces non-linéarité complique le calcul de la matrice de rigidité tangentielle dans une formulation d'éléments finis non-linéaire. Dans cette thèse, nous proposons une nouvelle technique pour réduire cette complexité. Notre technique consiste à mettre à jour une partition choisie de la matrice de rigidité tangentielle au lieu de la matrice entière lors d'un processus itérative de la méthode classiques de Newton-Raphson. Dans cette étude nous utilisons la déformation géométrique non linéaire et le modèle hyperélastique non linéaire de Mooney-Rivilin. Notre technique a prouvé d'avoir une vitesse de convergence élevée sans perte de précision. Nous avons fourni des conditions suffisantes pour la convergence de notre algorithme en donnant des contraintes de limite supérieure explicites en utilisant le théorème de Kantorovich.

Mots clé: Déformation non-linéaire hyperélastique; modèle de Mooney-Rivilin; élément finis non-linéaire; Newton-Raphson méthode; Modélisation biomécanique; réalité virtuelle; simulation chirurgicale.

Notation

- F The deformation Gradient

- $\mathbf{C}$ The right Cauchy-Green deformation

- $\mathscr{E}$ The Strain

- σ The Cauchy stress tensor

- P The first Piola-Kirchhoff stress tensor

- $\mathscr{S}$ The second Piola-Kirchhoff stress tensor

- $\mathscr{W}$ The strain energy density

- $\mathscr{D}$ The fourth-order constitutive tensor for isotropic materials

- $\mathscr{P}(u)$ The total energy

- $\mathscr{P}^{int}$ The stored strain energy

- $\mathscr{P}^{ext}$ The work done by external forces

- $\bar{\mathscr{P}}$ The first-order variation of $\mathscr{P}$

- f^b The external body force

- u The displacement

- $\hat{u}$ The perturbation

- u_ν The perturbed displacement

- $a(u,\hat{u})$ The energy form

- $l(\hat{u})$ The load form

- sym(.) The symmetry operator for matrices

- ∇_0 The gradient operator with the respect to the coordinate frame of the organ at rest

- $\mathbf{r}$ The residual of the total energy linearizion

- R The nonlinear functional

- $\{\cdot,\cdot\}$ The bilinear operator

- N_i The shape function

- C_{ij} The material constants

- D_i The material constants

- J The elastic volume ratio

- μ_i,α_i The characteristic constants of the material

- λ_i The principal stretch ratio

- I The invariants of the right Cauchy-Green strain tensor

- λ_i^2 The three eigenvalues of $\mathbf{C}$ with $(i = 1, 2, 3)$

- $tr()$ The trace of a matrix

- $det()$ The determinant of a matrix

- $J(u)$ The Jacobian matrix

- J_i The reduced invariants with $(i = 1, 2, 3)$

- $J_{i,\mathscr{E}}$ The derivatives of the reduced invariants with respect to Lagrangian strain with $(i = 1, 2, 3)$

- $\mathbf{I}$ The 3×3 identity tensor

- Ω_0 The domain occupied by the organ at rest

- $\mathbb{B}$ The Banach space

- $L^2(\Omega_0)$ The Hilbert space of square integrable functionals overs Ω_0

- $< ., . >$ The inner product

- $\mathcal{V}, \mathcal{V}_0$ The Sobolev space

- $\mathscr{M}(x)$ The tensor function

- $\{.\}$ The represent tensor

- $\|.\|_F$ The Frobenius norm

- $\partial \Omega_0$ The boundary of the organ

- Γ The fixed part

- Ω_h The sub-discretized organ becomes

- ω_h^e The e-th element

- $\mathcal{V}_h(\Omega_h)$ The Sobolev spaces of the sub-discretized organ

- ϵ_{ij} The kronecker symbol

- x_I The 3D coordonate of node

- $\mathrm{span}()$ The set of linear combinations of elements of a set

- φ_I The shape function

- Π_h The projection space

- $\mathcal{F}_a$ The Fréchet derivative of a

- $\lfloor \cdot \rfloor$ The operator transforms the 4-tensor to a 2-tensor

- $\otimes$ The dyadic product

- $\mathrm{sym}(.)$ The symmetry operator for matrices

- $:$ The contraction operator

Introduction

The domain of computer simulation and virtual reality is very deeply rooted in the world. In this work, we are interested in surgical simulation based on virtual reality. Surgical simulation is a modus operandi that offers a realistic training to promote the practice of innovative and less invasive procedures while improving the surgeon's learning. The latter can help surgeons to preoperatively assess an operation and perform complex operations. However, there are several mechanism issues in surgical simulators regarding the precision, speed, and realism of soft tissue deformation or cutting.

Surgical simulation in virtual reality has advantages such as: The simulations can be repeated as many times as the user wishes, practice on different levels from easy to complex situation, possibility of self-training and the simulation platform can be installed in any structure. And it also has disadvantages related to the cost of the purchase which is very high, the installation and the feeling of force feedback which is different from the reality and problem of the graphics. Surgical simulation has become increasingly important in recent years. The main objective of these simulators is never practice the first time on a patient. Therefore, it requires real-time perception for user gestures to mimic reality. The major problems observed in the realization of these simulators are: Geometric and physical modeling of organs, identification of mechanical characteristics and resolution of nonlinear problems. Our objective in this thesis is the resolution of nonlinear problems. We are interested in the problem of simulation accuracy and speed. More precisely, the speed of computing accurate deformations of hyperelastic soft tissues (Soft tissue is extra-skeletal support tissue, such as adipose tissue, tendons, ligaments, fascia, skin). It is well known that the deformation of soft tissues by a large displacement is nonlinear and that complicates the resolution and the integration of this deformation in a realistic simulator. So, the question that must be asked in this case is what is the most efficient, quickest, and accurate method of solving among the solving methods used in the literature? To answer this problem we chose the nonlinear finite element method for geometric modeling and the classic Newton-Raphson method of resolution. The finite element method is known for its precision and its drawback on the speed in resolution with iterative methods for larger meshes. For this reason we try to improve the speed of resolution without losing the precision. We propose a partial updated stiffness matrix for optimize the computation time. Also, we propose to improve the computation of radius of convergence by applying Kantorovich's theorem in the discretized domain by the nonlinear finite element method.

In the first chapter contains an introduction of the biomechanical model of hyperelastic tissues in the continuous medium. In surgical simulation, these hyperelstic tissues are modeled by complex geometry. In this case, the study and resolution of the nonlinear problems of these tissues in the continuous medium is difficult [30]. This difficulty is solved by the discretization of the complex geometry in the continuous medium into a simple geometric element [56]. The discretization method chosen in this thesis is the nonlinear finite element method. This method is known for its precision and efficiency in solving nonlinear problems. The major problems related to surgical simulation consist on the identification of the constitutive model, the geometrical nonlinearity and the identification of the properties of the soft tissues. The precise geometric and physical information provided by the medical images can be used to create an average virtual patient model, to train the surgeon on different types of surgical procedures. The second chapter presents the classical method of Newton-Raphson for the numerical convergence of

solutions. The algorithms of resolution used for the nonlinear finite element method are incremental and iterative which often presents difficulties of convergence related to the existence of a limit point in load or in position [45]. This difficult can be solved by using Kantorovich's theorem. This theorem makes it possible to verify the convergence of the solution in the continuous domain. For their application in the discretized domain, we introduce hypotheses and propositions to calculate and improve the convergence radius.

The third chapter shows the drawback of the Newton-Raphson resolution method in their use in the nonlinear finite element method. Such that, for a large mesh the total tangential stiffness matrix is calculated at each iteration which influences on the cost and the speed of calculation. In the surgical simulation, human organs are represented by complex geometry. Also, operations are done on a specific region which presents another constraint. With these constraints, we propose a modification in Newton-Raphson method by a partially updated tangential stiffness matrix. This proposition is tested by different regular meshed cube and non-regular liver mesh with nonlinear hyperelastic constitutive models such as Mooney-Rivlin, NeoHooken and Saint Venant Kirchoff.

In the last chapter, we present the surgical simulation based on virtual reality. We show some surgical simulator in the state of the art section and we define the material used for operation in virtual reality. For tested the effectiveness of our approach of modified Newton-Raphson method with a partially updated stiffness matrix on a surgical simulator. We integrate it in our simulator via unity 3D platform. In this part, we show the result of liver and gallbladder tests.

In this thesis, we are interested in improving the computation and the speed of the radius of convergence using Kantorovich's theorem in the discretized domain with nonlinear finite element method. Also, to improve the cost of computation the tangentiel stiffness matrix with partially updated.

Chapter 1

Biomechanical modeling of soft tissue

1.1 Introduction

Biomechanics is by definition a mechanics applied to biology. More specifically, The Study of the human body in motion, of the external forces (ground reaction force) which act on it and of the internal forces. The biomechanics is the product of mechanical technological advances and other sciences such as health, anatomy and physiology. On the technical level, research in biomechanics is centered on:(i) Acquisition of internal geometry.(ii) Modeling of the soft body by elements (several, tens of thousands of elements).(iii) Identification of mechanical properties on soft tissues.

1.2 Importance of biomechanical modeling in the design of surgical simulators

The modeling of the human body depends on the biomechanical analysis. When the organ affected to a deformation it change it shape. Therefore, it is essential to adopt a model which allows the analysis of deformation of the organ. This step is important in the biomechanical analysis [71, 70]. Biomechanical modeling consists of numerically representing the mechanical behavior of the human body. it is based on the dynamometric and kinematic recording of the mechanical chain to determine the external forces applied to the organ. This determination is made using the fundamental laws of mechanics. Pellicer et al. [56] developed a machine learning model that provides real-time inference. they tested their model on dozens of simulations with the biomechanical behavior of the liver which is carried out by the finite element method on several different liver geometries. Miller et al. [46] proposed a physics-based brain modeling approach. The deformations of brain are described in mechanical terms. This approach is carried out for the application on surgical simulation and recording of neuro-images.

1.3 Continuum modeling of hyperelastic tissue in surgical simulation

We can say that the domain contains a continuous material medium if at each moment and at each point of this domain the local physical quantities relating to this material medium are well defined. The physical quantity can be represented mathematically by: scalar, vector and tensor of order 2 or higher order [47]. The goal of a continuous medium (the volume of matter) is that can use the mathematical notions of continuity and apply them to a reality. In physics, we can represent physical quantities such

as density, temperature, displacement, pressure by continuous functions in space and time. Moreover, the continuity medium remains a valid hypothesis under certain physical conditions and at macroscopic scales. To perform surgical simulation, we must found a model that simulates the largest possible range of behavior with optimization of the computational cost [78]. The continuous modeling of a tissue is based on the equations of the mechanics of continuous media. These equations show the relations between the strains and stresses of a tissue.

1.3.1 Stress and Strain in continuum medium

In large deformation, the behavior of the material under strain is studied in continuum mechanics. The representation of a large deformation of a material is linked to a deformed or undeformed geometries. There are two representations of the deformation either by Eulerian Description: the deformation is identified by its position at the current instant (t). By Lagrangian description: the deformation is identified by its initial position. In this thesis we use the Lagrange deformation.
Let us consider an object subjected to forces and displacements so that its geometry passes from the initial state to the current state. In the initial undeformed geometry we consider $P \in \Omega$ identified by vector $X = \{X_1, X_2, X_3\}$ and is mapped to a point $Q \in \Omega$ identified by vector $x = \{x_1, x_2, x_3\}$ in the current deformed geometry[33].
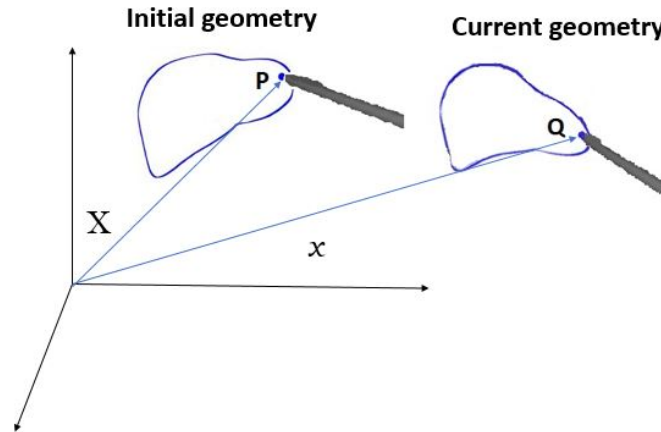
Figure 1.1: The initial and current state of object.

In geometric deformation, we have:

$$\begin{cases} x_1 & = x_1(X_1, X_2, X_3) \\ x_2 & = x_2(X_1, X_2, X_3) \\ x_3 & = x_3(X_1, X_2, X_3) \end{cases} \quad (1.1)$$

The mapping relation is:

$$x = X + u(X, t) \quad (1.2)$$

where $u(X, t)$ is the displacement of point P. This relation says that for a given point P in the undeformed geometry, a unique point Q exists in the deformed geometry.

Deformation Gradient

The neighboring points at infinitesimal distances from P and Q are denoted by vectors dX and dx. The relationship between differential elements dX and dx is as follow [33]

$$dx = \frac{dx}{dX}dX \Rightarrow dx = FdX \tag{1.3}$$

Where F is the deformation of Gradient can be written explicitly as

$$F_{ij} = \frac{dx_i}{dX_j} \tag{1.4}$$

Using the relation in eq.(1.2), F becomes:

$$F = 1 + \frac{\partial u}{\partial X} = 1 + \nabla_0 u \tag{1.5}$$

Where, $\frac{\partial u}{\partial X}$ is the displacement gradient. F must be positive for large deformation.

Lagrangian strain

Using the undeformed geometry as a reference, the vector dX is deformed to dx. So, the change in squares of length of these two vectors is as follows [33]:

$$
\begin{aligned}
\|dx\|^2 - \|dX\|^2 \quad &= dx^T dx - dX^T dX \tag{1.6} \\
&= dX^T F^T F dX - dX^T dX \tag{1.7} \\
&= dX^T (F^T F - 1) dX \tag{1.8}
\end{aligned}
$$

Where, $F^T F = \mathbf{C}$ is a right Cauchy-Green deformation.

The Lagrangian strain can be written as:

$$\mathscr{E} = \frac{1}{2}(\mathbf{C} - 1) \tag{1.9}$$

The factor $\frac{1}{2}$ is used to make the definition identical to the engineering strains in case of infinitesimal strains.

Cauchy and Piola-Kirchhoff Stress

In the equilibrium of a structure, stress is used to determine the failure of a material. It also depends on the frame of reference like strain. Figure 1.2 show in the current geometry the stress vector at point Q can be written using the area of the differential element ΔSx, the force Δf acting on it, and the unit normal n of the area as:

15
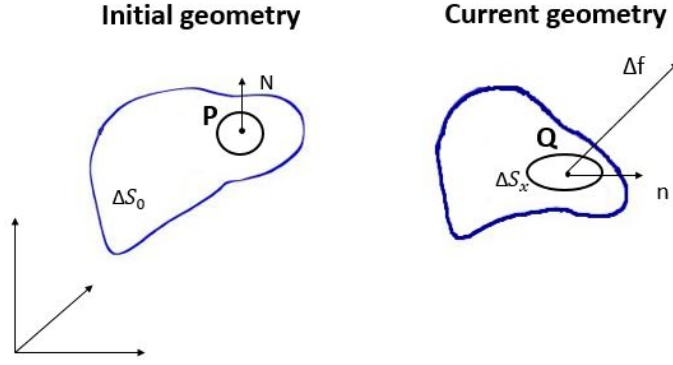
Figure 1.2: Stress vector in initial and current geometries.

The stress vector can be writte as [33]:

$$\lim_{\Delta S_x \to 0} \frac{\Delta f}{\Delta S_x} = \sigma n \qquad (1.10)$$

$$\lim_{\Delta S_0 \to 0} \frac{\Delta f}{\Delta S_0} = P^T N \qquad (1.11)$$

Where σ is known as the Cauchy stress tensor (3×3), and P is known as the first Piola-Kirchhoff stress tensor(3×3)
The relation between P and σ is [33]:

$$P = JF^{-1}\sigma \qquad (1.12)$$

P has an undesirable property that it is not symmetric, for to be symmetrical we multiply it by F, we define the second Piola-Kirchhoff stress tensor as follow:

$$\mathscr{S} = PF^{-T} = JF^{-1}\sigma F^{-T} \qquad (1.13)$$

Where, we can write the Cauchy stress tensor as follows:

$$\sigma = \frac{1}{J}F\mathscr{S}F^T \qquad (1.14)$$

1.3.2   Constitutive Relation

The constitutive theory describes the macroscopic behavior of a material between strain and stress caused by deformation [33]. A soft tissue is called elastic when a strain energy density $\mathscr{W}$ exists such that the stress can be obtained by differentiating $\mathscr{W}$ with respect to Lagrangian strain $\mathscr{E}$ [33].

$$\mathscr{W}(u) = \frac{1}{2}\mathscr{E}(u) : \mathscr{D}(u) : \mathscr{E}(u), \qquad (1.15)$$

Where $\mathscr{D}$ is the fourth-order constitutive tensor for isotropic materials. $\mathscr{D}$ and $\mathscr{E}$ are nonlinear in u. We can determined stress by differentiating the strain energy density with respect to the Lagrangian strain. This stress $\mathscr{S}$ called the 2nd Piola Kirchoff stress [33].

$$\mathscr{S}(u) = \frac{\partial \mathscr{W}}{\partial \mathscr{E}}(u) = \mathscr{D}(u) : \mathscr{E}(u). \qquad (1.16)$$

The potential energy of an hyperelastic system is the difference between the stored strain energy $\mathscr{P}^{int}$ and the work done by external forces $\mathscr{P}^{ext}$ [33], where we can formulated as:

$$\mathscr{P}(u) \quad = \mathscr{P}^{int}(u) - \mathscr{P}^{ext}(u) \tag{1.17}$$

$$= \oint_{\Omega_0} \mathscr{W}(\mathscr{E})d\Omega - \oint_{\Omega_0} u^T f^b d\Omega \tag{1.18}$$

Where f^b is the external body force. Let us consider that the displacement u is perturbed in the direction of $\hat{u}$ ($\hat{u}$ is called the virtual displacement). Where, this perturbation is often used to find the displacement at the minimum potential energy. The perturbation is controlled by parameter ν. So, the perturbed displacement is written as follows:

$$u_\nu = u + \nu \hat{u} \tag{1.19}$$

For keeping the displacement u_ν in the space of admissible solution, we use the set space $\mathcal{V}_0(\Omega_0)$ (where $\mathcal{V}_0(\Omega_0)$ is Sobolev spaces defined in section 2.2). Consequently, the variation $\hat{u}$ must satisfy the essential homogeneous boundary condition, i.e, $\hat{u} \in \mathcal{V}_0(\Omega_0)$. Then, the first-order variation of $\mathscr{P}$ in any direction u must be zero, as [33]

$$\bar{\mathscr{P}}(u,\hat{u}) = \frac{d\mathscr{P}}{d\nu}(u + \nu \hat{u})_{|\nu=0} \tag{1.20}$$

Using eq 1.18, we can write:

$$\bar{\mathscr{P}}(u,\hat{u}) = \frac{\oint_{\Omega_0} \mathscr{W}(\mathscr{E})d\Omega}{d\nu} - \frac{\oint_{\Omega_0} u^T f^b d\Omega}{d\nu}_{|\nu=0} \tag{1.21}$$

$$= a(u,\hat{u}) - l(\hat{u}) \tag{1.22}$$

$$= 0 \tag{1.23}$$

Where, $a(u,\hat{u})$ is the energy form [33]

$$a(u,\hat{u}) = \oint_{\Omega_0} \mathscr{S}(u) : \hat{\mathscr{E}}(u,\hat{u})d\Omega \tag{1.24}$$

$$= \oint_{\Omega_0} \mathscr{S}(u) : \text{sym}\left(\nabla_0 \hat{u}^\top F(u)\right) d\Omega \tag{1.25}$$

sym(.) is the symmetry operator for matrices. ∇_0 is the gradient operator computed with respect to the coordinate frame at rest.
Then $l(\hat{u})$ is the load form [33]

$$l(\hat{u}) = \oint_{\Omega_0} \hat{u}^T f^b d\Omega \tag{1.26}$$

The variational equation for the nonlinear elastic system can be written as:

$$a(u,\hat{u}) = l(\hat{u}) \tag{1.27}$$

The eq. (1.27) is the weak form of nonlinear hyperelastic systems, it is called the material description or the total Lagrangian formulation. Nonlinearity comes from the fact that the stress and strain implicitly depend on u. The two forms internal ($a(u,\hat{u})$) and external ($l(\hat{u})$) are nonlinear in u and linear in $\hat{u}$. The residual between the variation of internal energy and the variation of external energy is defined as [33]

$$\mathbf{r}(u,\hat{u}) = a(u,\hat{u}) - l(\hat{u}), \text{ for all } \hat{u} \in \mathcal{V}_0(\Omega_0). \tag{1.28}$$

In hyperelastic problem, we aims to find u, for all $\hat{u} \in \mathcal{V}_0(\Omega_0)$, which guarantees the nonlinear residues $\mathbf{r}$ to be zero (u balances internal and external energies).

$$\text{Find } u \in \mathcal{V}_0(\Omega_0), \text{ s.t. } \mathbf{r}(u, \hat{u}) = 0, \text{ for all } \hat{u} \in \mathcal{V}_0(\Omega_0). \tag{1.29}$$

Thus, we can rewrite the difference between $a(u, \hat{u})$ and $l(\hat{u})$ as a nonlinear functional $R : \mathcal{V}_0(\Omega_0) \rightarrow \mathcal{V}_0(\Omega_0)$ applied to $\hat{u}$ with a bilinear operator $\{\cdot, \cdot\}$ as follows [33]

$$\{R(u), \hat{u}\} := a(u, \hat{u}) - l(\hat{u}) \tag{1.30}$$

So, we can rewrite the problem defined in eq 1.29 with only the unknown u using eq 1.30 as follows

$$\text{Find } u \in \mathcal{V}_0(\Omega_0), \text{ s.t. } R(u) = 0. \tag{1.31}$$

1.4   Nonlinear modeling of organ's deformation

The linear analysis of structures is defined by three assumptions which are:(i) The behavior of the material which is elastic.(ii) The deformations which are infinitesimal. (iii) The resistance of the material which is infinite. This analysis is justified only if the stress, strain and displacement are low. In reality, for a fairly large deformation and displacement, the structural mechanics are nonlinear. Nonlinearities are associated with material, geometry, applied forces, and boundary conditions [49].

1.4.1   Nonlinear geometry

Geometric nonlinearity is expressed by a significant change in the initial structure. The deformed structure has a structural representation different from that in the initial state (see figure 1.3 [55]). In this case, the physical and mechanical properties of the initial and deformed structure are significantly different. Therefore, it is necessary to rewrite the equilibrium system taking into account the deformed structure [15]. Geometric nonlinearities are modeled using appropriate constitutive equations with a high deformation stress. So that the second Piola-Kirchhoff stress and the Green-Lagrange nonlinear strain tensor are used [24]. Nonlinear relations can be used with a hyperelastic model, to directly account for all nonlinearities (mechanical and geometric) in the mathematical formulation [12]. A finite element model handling geometric and material properties nonlinearities is proposed for human liver and implemented in [58].

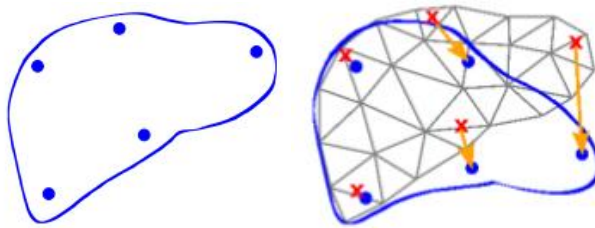Figure 1.3: Initial and deformed geometries [55].

1.4.2   Nonlinear constitutive model

The hyperelsatic biological soft tissues are modeled by non-linear contitutive laws. The constitutive hyperelastic theory takes into account two types of non-linearities: physical non-linearity and geometric non-linearity [20]. Therefore, the aim of these constitutive theories is to develop mathematical models

18

that reproduce the true behavior of biological tissues based on the theory of nonlinear continuum mechanics [13]. A homogeneous isotropic hyperelastic material has as principles:(i) Material objectivity, the constitutive equation is invariant under changes of reference. (ii) The isotropy of the material, the strain-energy function is not affected by a superimposed rigid body transformation before deformation [62]. For anisotropic soft tissues, the constitutive laws can be derived from the stress energy density function $\mathscr{W}$, which is specified for each reference volume unit. $\mathscr{W}$ is expressed as a function of the strain gradient (F) or the green-lagrange strain tensor ($\mathscr{E}$) (i.e $\mathscr{W} = \mathscr{W}(\mathscr{E}) = \mathscr{W}(F)$). For isotropic soft tissues, the constitutive laws are defined using the strain energy density $\mathscr{W}$. This quantity corresponds to the energy stored in the soft tissue after loading ($\mathscr{W} = \int_0^{\mathscr{E}_{ij}} \mathscr{S}_{ij} d\mathscr{E}_{ij}$). The constitutive theories offer the possibility of minutely describing the behavioral characteristics of materials by an improvement of the mathematical models [6, 23].

1.5   Modeling with Nonlinear Finite Element

1.5.1   Nonlinear deformation

Highly deformed structural elements are increasingly used in engineering and biomedical applications. In order for these components to behave correctly under strong strain and displacement, it is important to improve and apply special methodologies and techniques. In the biomedical application, the major factor which complicates the study of deformation is the non-linearity of soft objects which presents a high degree of difficulty. Generally, the resolution of this type of problem is done by numerical methods [53]. The different stages of analysis of a physical problem are organized according to the process shown schematically in figure 1.4. The first step is the physical problem. The precise framework of the study is defined by the simplifying assumptions which make it possible to determine the appropriate mathematical model. The difficulty for the engineer is to know how to choose among the laws of physics, those whose equations will translate with the desired precision the reality of the physical problem. A good choice should give an acceptable answer for non-prohibitive implementation efforts.

1.5.2   Nonlinear Finite Element Method

This method divides a continuous domain into smaller parts called finite elements, connected together by nodes (see figure 2.6). The continuous variable is approximated on the finite element domain by interpolation or shape functions. There are several types of elements that can represent an organ, for example (triangles, squares) in 2D space and (tetrahedron, hexahedron) in 3D space. Tetrahedral elements are the best for modeling a complex geometry domain with little mesh distortion. Moreover, the element tetrahedron uses exact formulas without Gaussian integration to generate the characteristics of the element[65] . Most researchers used tetrahedron elements because they are well adapted to geometries of arbitrary shape thanks to their simple calculations. Chamoret et al. [14] presented a hand modeled by nonlinear finite elements, which is in contact with a deformable object. This modeling makes it possible to study the contact pressures between the hand of an operator and a hand tool. Meister et al. [44] explored the use of neural networks to directly learn the underlying biomechanics. They used the explicit FEM as the reference and they highlighted the possibility of going beyond their stability limit. Liu et al.[40] discretized the geometry of the head-and-neck tumor into tetrahedral elements and mesh as fiducial biomarkers in order to follow their movements.They applied different force fields to the outer surface of the geometry and used FEM software Abaqus as a nonlinear finite element solver to simulate tumor deformation under different load cases.
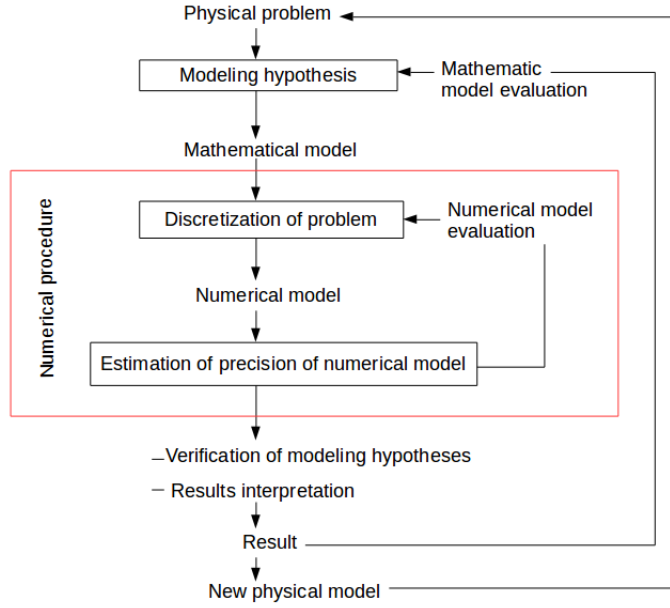
Figure 1.4: Numerical analysis process.

The shape function of tetrahedron

For the isoparametric element, the geometric transformation (figure 1.5) which changes from the reference element to the real element has the following properties:

$$x = \sum_{i=1}^{4} N_i x_i \qquad (1.32)$$

Where x_i is the nodal coordinate, and N_i is the shape function.
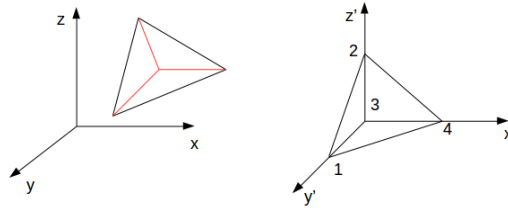
Figure 1.5: Geometric transformation of tetrahedron.

The shape functions is given by:

$$N_1 = \frac{1}{6V}(\alpha_1 + \beta_1 x + \gamma_1 y + \delta_1 z) \qquad (1.33)$$
$$N_2 = \frac{1}{6V}(\alpha_2 + \beta_2 x + \gamma_2 y + \delta_2 z) \qquad (1.34)$$
$$N_3 = \frac{1}{6V}(\alpha_3 + \beta_3 x + \gamma_3 y + \delta_3 z) \qquad (1.35)$$
$$N_4 = \frac{1}{6V}(\alpha_4 + \beta_4 x + \gamma_4 y + \delta_4 z) \qquad (1.36)$$

Where V is the volume of element and α_i, β_i, γ_i and δ_i with $(i = 1, 2, 3, 4)$ are constants defined in the appendix A.

We can expressed the relation between coordinate and displacement of the element by:

$$u = \sum_{i=1}^{4} N_i u_i \tag{1.37}$$

Where u_i is the nodal displacement.

1.6 Solving methods

Non-linearities are classified according to their source in the model mathematics of the mechanics of continuous and correlated media with the physical system. For structural analysis there are two sources of non-linear behavior: Geometric non-linearity (the change in geometry caused by large deformation). Constitutive non-linearity (the material behavior which depends on the strain). In the biomechanical domain, the hyper-elastic tissues have a non-linear behavior [40]. It is necessary to develop reliable and efficient solving algorithms to perform deformations imitated to reality. For FEM, classical solving algorithms are incremental and iterative algorithms. However, the algorithms of resolution depend in a general way on the type of nonlinear problem which one wishes to treat. The iterative incremental method is used for this type of problem. A balance correction is introduced on each increment using an iterative process. This correction can be done in several ways according to the type of stiffness matrix used. There are several iterative incremental methods which the best known is that of Newton-Raphson [11, 67]. The Newton-Raphson method recompute the tangent stiffness matrix with each iteration for solving the problem. This method has fast convergence, but its main drawback lies in the computation time of the update of the tangent stiffness matrix at each iteration. So, Liu et al. [41] proposed a quasi-Newton method which allows an efficient simulation of a large class of hyperelastic materials. Bai et al. [4] used the Newton-Raphson as a solver for quasi-analytic inverse kinematics approach of the 6 degree of freedom manipulator in the Da Vinci surgical robot and other similar systems. Wang et al. [73] presented a numerical solver to solve the problem of nonlinear equations in the dynamics of deformation of blood vessels. They used the hyperelastic continuum model, and a nonlinear solver based on finite element discretization.

1.7 Problems related to the design of surgical simulators

1.7.1 Introduction

A surgical simulator uses geometric and physical modeling of human tissue to model biomedical information. Then, it returns this information to the user through a multimodal interface, with visual and haptic feedback [21]. The problems observed during the realization of these simulators are the geometric modeling. Also, the modeling of the contacts between the virtual instruments and the soft tissues as well as the biomechanical deformation of the soft tissues for the physic modeling. In the literature we find several mathematical models have been proposed in this context which includes two antagonistic elements: the realism of the simulation and the calculation time [57, 5]. In addition, the user interface of the surgical simulator is essential for effective training, as surgeons act as if they were operating on a real patient (figure1.6). Sight and touch are the two main senses for producing compelling visual and haptic rendering [64, 34]. In this case, it is important to give a realistic view of the deformations and forces, otherwise the surgeon may learn inappropriate procedures. As well as, the constraints of real-time realization which are essential for surgical simulation systems. Where, the first constraint depends on the speed of communication between the different elements of the system, while the second constraint depends on the complexity of the geometry and the physical models and calculation algorithms[17, 63].

Figure 1.6: Block diagram of surgical simulator.

1.7.2   Problem related to the haptic feedback

Haptic feedback is the vibratory sense of touch that is used as a communication between the controllers and the user. In surgery, haptic feedback refers to the sense of touch that a surgeon feels during surgery (figure 1.7). Integrating haptic feedback into simulators leads to better performance and operational skills [68]. The problem with using haptic feedback in simulators is that it requires expensive research and analysis to determine its necessity [59]. Therefore, we find the haptic simulator expensive. Among the critical found in the haptic feedback are sensitivity to noise, high cost and difficulty of implementation, and ability to be used in surgical simulators [27].
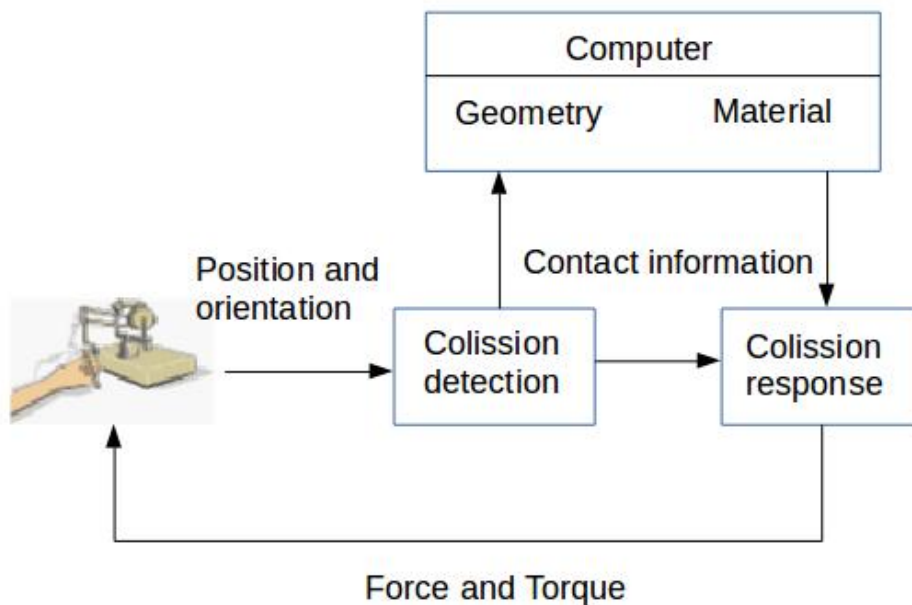
Figure 1.7: Block diagram of haptic feedback.

1.7.3   Problem related to the visual feedback

In a surgical simulation, the user must feel the haptic and visual interactions in a simulation test (figure 1.8). There is a fair amount of research focused on visual feedback in the literature. But the problem is that the methods proposed in this context are not based on physics [29]. In real time, the simulator must provide tens of millions of images in a fraction of a second for better visualization and this is the known problem in realistic simulators. however, these conflicting requirements are difficult to meet [79].

22

Kara et al. [32] proposed a mechanism based on computer vision to detect and recognize objects and to apply an optimal hand gesture through visual feedback. In this work we use a Headset HMD.
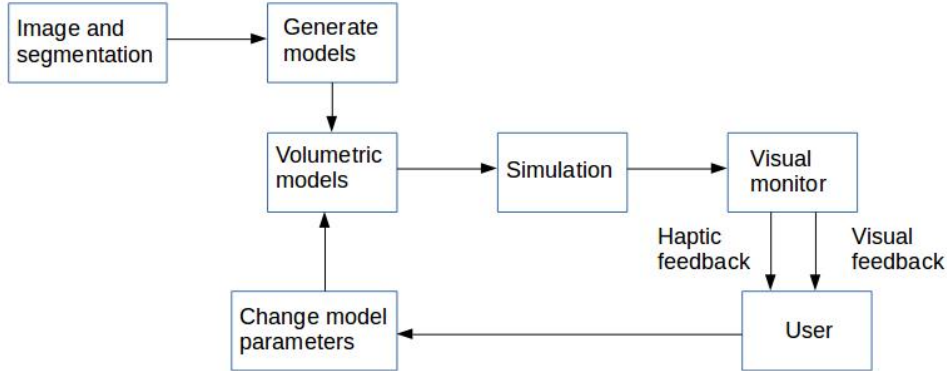
Figure 1.8: Block diagram of visual feedback.

1.7.4 Problem of soft tissue characterization

In hyperelasticity, three problems are rising. The classical problem of geometry, The identification of the constitutive laws of the material as well as the reconstruction of the force. In the problem of geometry, the objective is to calculate the displacement field u, the strain field $\mathscr{E}$ as well as the stress field $\mathscr{S}$ undergone by the material. In this case, the problem of identification is to know the geometry, the boundary conditions and the nature of the constitutive equations. In the problem of identifying the constitutive laws of material, the objective is to find the constitutive parameters and the stress field $\mathscr{S}$ after knowing the geometry, the limiting conditions, the nature of the constitutive equations and the fields $\mathscr{E}$ and u. In the problem of reconstruction of the force, the objective is to find the distribution of the force on the geometry as well as the stresses $\mathscr{S}$ in the material by knowing the fields u and $\mathscr{E}$, the limiting conditions in terms of support, the nature of the constitutive equations as well as the parameters of these equations [42, 2]. The simulation of soft tissues poses certain difficulties related to the modeling and highly realistic training of these tissues. In modeling, the identification of soft tissue characteristics is the first critical factor to be found. Where, the modelization take account to compression, tension and shear. For example, the mechanical characterization of hepatic tissue is of great interest in the management of the liver because the different forms of deformation subjected to the liver tissue exhibit different mechanical characteristics [76, 26].

Many models have been developed to represent the mechanical behavior of hyperelastic materials. The modeling of soft tissue behavior requires nonlinear constitutive laws (see figure 1.9). The most common nonlinear constitutive laws are limited by studies of identification of model parameters from experimental tests. These laws are defined by a specific strain energy function $\mathscr{W}$. The most popular non linear constitutive laws are summarized in table 1.1.
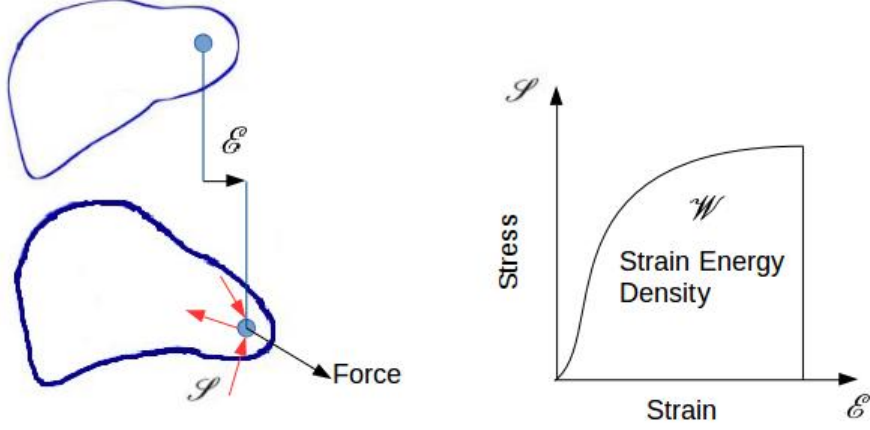
Figure 1.9: Stress, Strain and Strain Energy Density.

Table 1.1: Hyperelastic material models

Phenomenological models	
Fung	$\mathscr{W} = \frac{1}{2}[a(\sum_{i=1}^{3}\lambda_i^2 - 3) + b(e^{(C_1(\sum_{i=1}^{3}\lambda_i^2 - 3))} - 1]$
Mooney-Rivlin	$\mathscr{W} = C_{10}(I_1 - 3) + C_{01}(I_2 - 3) + \frac{1}{D}(J - 1)$
Ogden	$\mathscr{W} = \sum_{i=1}^{N} \frac{2\mu_i}{\alpha_i^2}(\lambda_1^{\alpha_i} + \lambda_2^{\alpha_i} + \lambda_3^{\alpha_i} - 3) + \sum_{i=1}^{N} \frac{1}{D_i}(J - 1)^{2i}$
Polynomial	$\mathscr{W} = \sum_{ij=0}^{N} C_{ij}(I_1 - 3)^i (I_2 - 3)^j + \sum_{i=1}^{m} D_i(J - 1)^{2i}$
Saint Venant-Kirchhoff	$\mathscr{W} = \frac{\lambda}{2}[tr(\mathscr{E})]^2 + \mu tr(\mathscr{E}^2)$
Yeoh	$\mathscr{W} = \sum_{i=1}^{3} C_i(I_1 - 3)^i + \sum_{i=1}^{3} \frac{1}{D_i}(J - 1)^{2i}$
Mechanistic models	
Neo-Hooken	$\mathscr{W} = C_{10}(I_1 - 3) + \frac{1}{D}(J - 1)^2$
Arruda-Boyce	$\mathscr{W} = \mu \sum_{i=1}^{5} \frac{C_i}{\lambda_m^{2i-1}}(I_1^i - 3^i) + \frac{1}{D}(\frac{J^2-1}{2} - ln(J))$

Where C_{ij} and D_i represents the material constants. J is elastic volume ratio. N is number of terms in strain energy function. μ_i, α_i are characteristic constants of the material and λ_i represent the principal stretch ratio.

For Lagrangian strain, the strain energy density is defined using the strain invariants or that of the strain tensor. The three invariants of the right Cauchy-Green strain tensor $\mathbf{C}$ are given as:

$$\mathbf{C} = F^T F \tag{1.38}$$

$$I_1 = tr\mathbf{C} = \lambda_1^2 + \lambda_2^2 + \lambda_3^2 \tag{1.39}$$

$$I_2 = \frac{1}{2}\left[(tr\mathbf{C})^2 - tr(\mathbf{C}^2)\right] \tag{1.40}$$

$$I_3 = det(\mathbf{C}) \tag{1.41}$$

Where F is the deformation of Gradient and λ_1^2, λ_2^2, λ_3^2 are three eigenvalues of $\mathbf{C}$.

For a large isostatic modulus of elasticity (Bulk's modulus), we can separate $\mathscr{E}$ into two parts: A

24

distortion part (contains the invariants I_1, I_2). A dilation part (contains the third invariant I_3). In order to separate the distortion part from dilatation, it is necessary to introduce the so-called reduced invariants, J_1 , J_2 , and J_3, defined by:

$$J_1 \quad = I_1 I_3^{-\frac{1}{3}} \tag{1.42}$$

$$J_2 \quad = I_2 I_3^{-\frac{2}{3}} \tag{1.43}$$

$$J_3 \quad = I_3^{\frac{1}{2}} \tag{1.44}$$

The derivatives of the reduced invariants with respect to Lagrangian strain can be written as:

$$J_{1,\mathscr{E}} \quad = I_{1,\mathscr{E}}(I_3)^{-1/3} - \frac{1}{3} I_1 (I_3)^{-4/3} I_{3,\mathscr{E}} \tag{1.45}$$

$$J_{2,\mathscr{E}} \quad = I_{2,\mathscr{E}}(I_3)^{-2/3} - \frac{2}{3} I_2 (I_3)^{-5/3} I_{3,\mathscr{E}} \tag{1.46}$$

$$J_{3,\mathscr{E}} \quad = \frac{1}{2}(I_3)^{-1/2} I_{3,\mathscr{E}} \tag{1.47}$$

Where

$$I_{1,\mathscr{E}} \quad = 2\mathbf{I} \tag{1.48}$$

$$I_{2,\mathscr{E}} \quad = 2(I_1 \mathbf{I} - \mathbf{C}) \tag{1.49}$$

$$I_{3,\mathscr{E}} \quad = 2I_3 \mathbf{C}^{-1} \tag{1.50}$$

Where $\mathbf{I}$ is a 3×3 identity tensor.

Several works have studied the mechanical behavior of hyperelastic materials. The major problem that is recognized in these studies is the identification of the mechanical parameters of soft tissue for different forms.

Hostettler et al. [28], proposed a method to compute a deformation field from skin position and a modelling of the diaphragm motion. They identified the Poisson's ratio and the Bulk modulus of the liver and kidneys in vivo and compared it to those in vitro available in the literature.

Boubaker [7], studied the nonlinear elastic behavior of pelvic tissue using the Mooney-Rivlin and Ogden model, and the identification of the parameters of these organs. He used a traction machine as measuring instrument (see figure1.10). Zwicki-line allows to perform tensile/compression tests up to 2.5 kN and torsion up to 5 Nm with very wide speed ranges and satisfactory specifications in terms of displacement and force.

Figure 1.10: ZWICKI-LINE 2.5kN-5 Nm [7].

Cecile [18], studied the mechanical behavior of the liver. She modeled the structures implemented in the liver by different types of behavior. She performed tests on a compression device (see figure 1.11). This allows the observation of behavior of the entire liver in compression in a non-anatomical position.

Figure 1.11: Experiment test of compression liver [18].

1.7.5 Addressed problem: Convergence speed and accuracy of nonlinear deformations

Among the main requirements in the construction of the surgical simulator, speed and precision in the mechanical response to organ deformations. The response of the deformation must be physically realistic and calculated in the real time to allow the interactions of the user with the virtual body such as the insertion of a needle or the cutting [19]. The difficulty arises on the modeling of organs which comes from the complexity in terms of composition of soft tissue materials. This leads to non-linear characteristics of the deformation of these tissues. Geometric and material non-linearities complicate problem solving and make it costly in terms of calculation. In this topic, several researchers have proposed techniques to improve the speed of convergence with great precision [31, 16]. Ren et al. [61] have built an intelligent simulation platform for venous surgery which includes a transformation based on the spring-mass. They

viewed the vessel as a soft tissue surface model with a uniform mass distribution, which can also be divided into grids. They subdivided the grids to improve accuracy and adopted the structure of the grid topology to improve performance in real time. They state that the finite element method has good stability and high precision. But, it found a difficulty in optimizing the cost of calculation and in the implementation. In our work we show that the FEM method can be faster and keep its stability and precision. Zhang et al. [77] presented a formulation of bio-heat transfer under the effect of soft tissue deformation for the rapid or near real-time prediction of tissue temperature, based on a fast explicit dynamic finite element algorithm for the transfer transient heat. Xie et al. [74] proposed an approach that combines the traditional nonlinear finite element method and nonlinear Kalman filtering to address both physical fidelity and real-time performance for soft tissue modeling. This approach defines mechanical tissue deformation as a nonlinear filtering process for the dynamic estimation of nonlinear deformation behaviors of biological tissues. Wang et al. [72] proposed a technique for real-time realization. They introduced a screening coefficient to filter the deformed part of the mesh. Only this part which will be treated using the nonlinear FEM model. The remaining of the mesh is fixed. This method optimized the computation cost and improved the execution time. The downside of this method is that the strain and stress of a soft tissue which are not physically realistic. In our work, we use the initialized value of the tangential stiffness matrix for the remaining part instead of fixing them.

1.8   Conclusion

This chapter, defined The biomechanical modeling of hyperelastic tissues in the continuous medium. The geometrical and physical nonlinearity of these tissues. The resolution of nonlinear deformation problem is treated by an iterative process the best known is that of Newton-Raphson. The model of the organ must be represented by a discretized mesh to solve its problems iteratively. The nonlinear finite element method is the most precise and preferable method for the majority of researchers. At the end, the main problems found in the conception of a surgical simulator are presented. The first problem that can be noted is the geometric and physical modeling of the human body. The expensive research and analysis for realizing the haptic and visual feedback. Also, The determination of the mechanical characteristics of biological tissues.

Chapter 2

Numerical convergence of Newton-Raphson algorithms

2.1 Introduction

In this chapter, we present numerical convergence method for hyperelastic soft tissue deformation. Hyperelasticity leads to nonlinearity of deformations. We use a nonlinear FEM for modeling the hyperelastic soft tissue. The complex geometry model requires the implementation of robust and efficient resolution methods in terms of computation time. This problems are solved by an iterative process. The famous method used for solving the nonlinear problems is that of Newton-Raphson. Then, we propose our contribution for checking the convergence of solution by Kantorovitch's theorem.

2.2 Preliminaries

Let us denote $\Omega_0 \subset \mathbf{R}^n$ the domain occupied by the target organ.

Definition of Banach space: For any set $\mathbf{f}$ and any Banach space $\mathbf{E}$, the space $\mathbb{B}(\mathbf{f}, \mathbf{E})$ of bounded maps from $\mathbf{f}$ to $\mathbf{E}$, endowed with the norm of uniform convergence.

Definition of Hilbert space: An inner product space which is complete with respect to the norm induced by the inner product is called a Hilbert space. Let $y \in \mathbf{R}^n$ then $\|y\|^2 = <y, y> = \sum_{i=1}^n |y_i|^2$ is the L^2-norm on $\mathbf{R}^n$.

Let us consider $L^2(\Omega_0)$ space of Hilbert with the inner product. For $\mathbf{f} = (\mathbf{f}_1, \mathbf{f}_2, ..., \mathbf{f}_n)^T \in \mathbf{R}^n$, and $\mathbf{g} = (\mathbf{g}_1, \mathbf{g}_2, ..., \mathbf{g}_n)^T \in \mathbf{R}^n$ with $x = (x_1, x_2, x_3)^T \in \Omega_0$. The inner product is as follow:

$$< \mathbf{f}, \mathbf{g} > = \oint_{\Omega_0} \sum_{i=1}^n \mathbf{f}_i(x)\mathbf{g}_i(x)dx \quad , \quad \|\mathbf{f}\|_{L^2}^2 = <\mathbf{f}, \mathbf{f}> \quad , \quad \mathbf{f}, \mathbf{g} \in L^2(\Omega_0) \tag{2.1}$$

Definition of Sobolev spaces: Sobolev spaces are functional spaces particularly suited to solving partial differential equation problems.
Let Ω_0 be any open of $\mathbf{R}^n$. We define the Sobolev space $\mathcal{V}$ by:

$$\mathcal{V}(\Omega_0) = \{\mathbf{f} \in L^2(\Omega_0) | \mathbf{f}(x) = 0, \text{ for all } x \in \partial\Omega_0, \ \partial\mathbf{f} \in L^2(\Omega_0)\}. \tag{2.2}$$

Where $\partial\mathbf{f}$ is a partial derivative of $\mathbf{f}$ in the weak sense.

Definition of Frèchet derivative: Let $\mathbb{B}(\mathbf{f}, \mathbf{E})$ is normed vector spaces. $\mathbf{f}'(x)$ is called the frèchet derivative at $x \in \mathbf{E}$ if there exist the linear operator $h \to \mathbf{f}(x)h$ such that

$$\lim_{\|h\| \to 0} \frac{\|\mathbf{f}(x+h) - \mathbf{f}(x) - \mathbf{f}'(x)h\|}{\|h\|} \tag{2.3}$$

Definition of a tensor function: Consider two tensors X and x which belong to the space $\mathbf{R}^n$. A mapping of the tensor $X \in \mathbf{R}^n$ into $x \in \mathbf{R}^n$ is called a tensor function and denoted by $\mathscr{M}(x)$.

If $\mathscr{M}(x)$, $x \in \Omega_0$, is a tensor functional, then its L^2-norm can be defined as

$$\|\{\mathscr{M}(x)\}\|_{L^2} = \|\|\mathscr{M}(x)\|_F\|_{L^2} \tag{2.4}$$

Where $\{.\}$ represent tensor and $\|.\|_F$ is the Frobenius norm. In this thesis, the tensor can be either of order 2 (e.g. the deformation gradient) or of order 4 (e.g. the constitutive tensor).

Definition of Frobenius norm: Let a matrix A $(m \times n)$. The Frobenius norm is defined as the square root of the sum of the absolute squares of elements A.

$$\|A\|_F = \sqrt{\sum_{i=1}^{m} \sum_{j=1}^{n} |a_{ij}|^2} \tag{2.5}$$

Lipschitz condition: Function $\mathbf{f}$ satisfies a Lipschitz condition in u on the set $\Omega_0 \subset \mathbf{R}^n$ if a constant $\gamma > 0$ exists with

$$\|\mathbf{f}(u) - \mathbf{f}(\bar{u})\| \leq \gamma \|u - \bar{u}\|, \text{ for all } u \text{ and } \bar{u} \in \mathbf{R}^n \tag{2.6}$$

Upper bound for inverse matrix: Let the matrix $A \in \mathbf{R}^{n \times n}$ ant it is invertible. There exists $\eta > 0$ such that:

$$\|A^{-1}\| \leq \eta \tag{2.7}$$

Taking $\mathcal{V}(\Omega_0)$ the L^2 Sobolev spaces with the inner product defined in eq 2.1. $\mathcal{V}(\Omega_0)$ represent the Sobolev spaces occupied by the target organ. In a biomechanical framework, the organs of the human body are attached by physiological links and clips (ligaments, tendons) see figure 2.1.
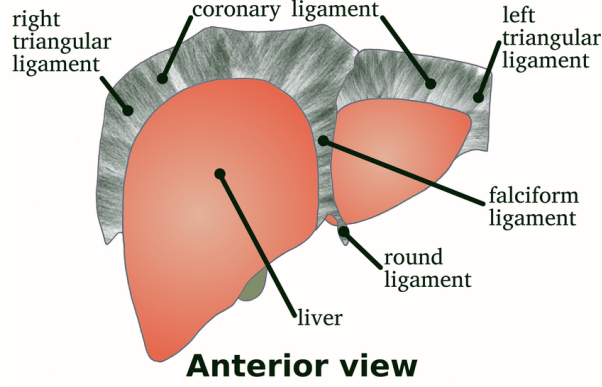
Figure 2.1: Liver anatomy showing the location of ligaments [48].

For that, we consider the space $\mathcal{V}_0(\Omega_0)$ such as:

$$\mathcal{V}_0(\Omega_0) = \{\mathbf{f} \in \mathcal{V}(\Omega_0)|\mathbf{f}(x) = 0, \text{ for all } x \in \Gamma \subset \partial\Omega_0)\}. \tag{2.8}$$

Where $\partial\Omega_0$ is the boundary of the organ and Γ is the fixed part. According to the continuous Sobolev injection [9, 1], the space $\mathcal{V}_0$ is included in $L^2(\Omega)$ ($\mathcal{V}_0(\Omega_0) \subset L^2(\Omega)$). For solving the problem in continuum modeling $\mathbf{f}(\mathbf{x}) = \mathbf{0}$, there is several method found in the literature. In the next section, The finite element method is used for solving this problem.

2.3 Newton-Raphson method

The Newton-Raphson method is an algorithm for finding the roots of nonlinear equations by successive linear approximations. The equilibrium equation eq 1.18 is nonlinear in the displacement field u.

$$\mathscr{P}(u) = \oint_{\Omega_0} \mathscr{W}(\mathscr{E})d\Omega - \oint_{\Omega_0} u^T f^b d\Omega$$

We want to find the field of displacements u such that $\mathscr{P}(u) = f$. Where, the potential energy $\mathscr{P}(u)$ has a nonlinear function of u and f is a vector of known quantities. By using Newton's method in the following way [33, 38]: The field of displacements starting from the i th iteration u^i is known and it is necessary to find the increment Δu^i to find the field of displacements u^{i+1} at the $i + 1$ th iteration of Newton's method by approximating using the first-order Taylor series:

$$\mathscr{P}(u^{i+1}) \approx \mathscr{P}(u^i) + \mathscr{K}_T^i(u^i).\Delta u^i = f \tag{2.9}$$

Where $\mathscr{K}_T^i(u^i)$ is the Jacobian matrix at i th iteration [33]

$$\mathscr{K}_T^i(u^i) \equiv (\frac{\partial\mathscr{P}}{\partial u})^i \tag{2.10}$$

The new approximate solution is obtained as follows:

$$u^{i+1} = u^i + \Delta u^i \tag{2.11}$$

Now, we can refer the difference between the applied force and the internal force as a residue. The residual of linearized equation is as follow:

$$R^{i+1} = f - \mathscr{P}(u^{i+1}) \tag{2.12}$$

Then, the iterative process calculates the solution u^{i+1}. If the residue is less than a given tolerance, this solution may be accepted as a precise solution and the process stops. Otherwise, the process is repeated until this residue becomes very small. The convergence criterion is expressed as follows:

$$conv = \frac{\sum_{j=1}^{n}(R_j^{i+1})^2}{1 + \sum_{j=1}^{n}(f_j)^2} < \epsilon \qquad (2.13)$$

The algorithm of Newton-Raphson method is as follows:

Algorithm 1 Newton-Raphson algorithm

Initialize u^0, k, *max_iteration*, *tolerance*
Calculate Jacobian matrix ($\mathscr{K}_T$) eq. (2.10)
Calculate residual (R) eq. (2.12)
Calculate convergence (*conv*) eq. (2.13)
while (*conv > tolerance* & $k < max\_iteration$) **do**
  if *conv* $\leqslant$ *tolerance* **then**
    stop.
  end if
  if ($k > max\_iteration$) **then**
    stop, with error message
  end if
  Calculate solution increment Δu
  Update solution by $u = u + \Delta u$
  Calculate convergence (*conv*) eq. (2.13)
  Set $k = k + 1$
end while

Example

Let us consider system of 2 nonlinear equations with 2 unknowns variable. Where:

$$g \colon \mathbf{R}^2 \ \to \mathbf{R}^2$$
$$g(u) = [g_1(u) \quad g_2(u)]^T$$

With $u = [u_1 \quad u_2]^T$. The solutions that satisfy both equations are the intersections of the contour curves of both $g_1(u_1, u_2)$ and $g_2(u_1, u_2)$. We consider the Taylor expansions of the 2 functions:

$$g_i(u + \Delta u) \approx g_i(u) + \sum_{j=1}^{2} \frac{\partial g_i(u)}{\partial u_j}\Delta u_j \qquad (i = 1, 2) \qquad (2.14)$$

So,

$$g(u + \Delta u) \ \approx \begin{bmatrix} g_1(u) \\ g_2(u) \end{bmatrix} + \begin{bmatrix} \frac{\partial g_1}{\partial u_1} & \frac{\partial g_1}{\partial u_2} \\ \frac{\partial g_2}{\partial u_1} & \frac{\partial g_2}{\partial u_2} \end{bmatrix} \begin{bmatrix} \Delta u_1 \\ \Delta u_2 \end{bmatrix} \qquad (2.15)$$
$$= g(u) + J_g(u)\Delta u \qquad (2.16)$$

Where, $J(u)$ is the Jacobian matrix. By assuming $g(u + \Delta u) = 0$, we can find the roots as $u + \Delta u$, where Δu can be obtained by solving the following equation:

$$\Delta u = J(u)^{-1}(g(u + \Delta u) - g(u)) = -J(u)^{-1}g(u) \qquad (2.17)$$

And the root can be found from any starting point u as:

$$u + \Delta u = u - J(u)^{-1} g(u) \qquad (2.18)$$

We take for the vector function g:

$$
\begin{aligned}
g_1(u_1, u_2) &= u_1^2 + 2u_1 u_2 - u_1 = 0 \\
g_2(u_1, u_2) &= u_2^2 + 2u_1 u_2 - u_2 = 0
\end{aligned}
$$

Where,

$$
J(u) = \begin{bmatrix} 2u_1 + 2u_2 - 1 & 2u_1 \\ 2u_2 & 2u_2 + 2u_1 - 1 \end{bmatrix}
$$
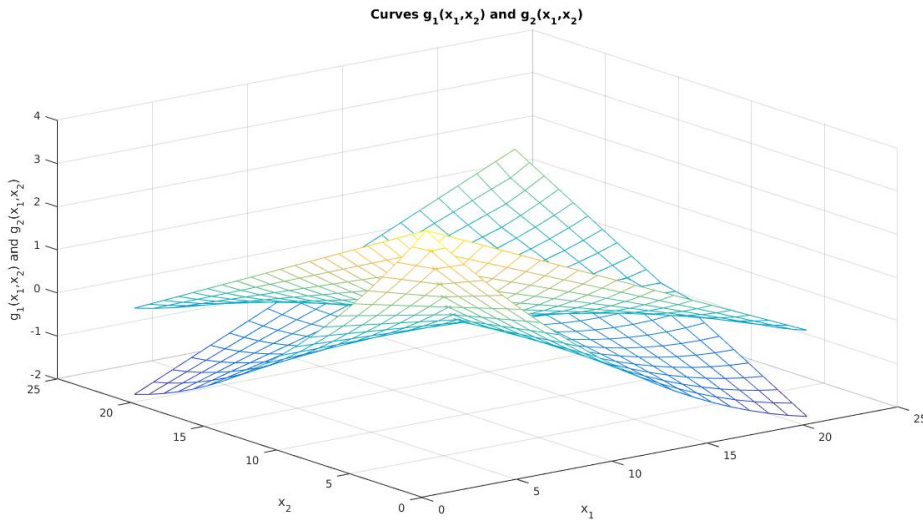
Figure 2.2: Function g in 3D

Figure 2.2 represent the mesh of the function g in 3D. The solutions exist in the intersections of the contour curves of both $g_1(u)$ and $g_2(u)$.

Let us consider in the first test, the initial values are $u_0 = [0.2, 0.1]$. And in the second test, the initial values are $u_0 = [0.85, 0.35]$. With convergence criterion ($conv = 10^{-5}$) and stop criterion ($max\_iteration = 10$).

The first test result with $u_0 = [0.2, 0.1]$:

$$
\begin{aligned}
Iteration \quad 1: \quad & u1 = -0.65000000000000057732, \quad u2 = -0.45000000000000051070 \\
Iteration \quad 2: \quad & u1 = -0.24258544652701230504, \quad u2 = -0.17786659316427810840 \\
Iteration \quad 3: \quad & u1 = -0.06528476968321939022, \quad u2 = -0.05144660209970475240 \\
Iteration \quad 4: \quad & u1 = -0.00816984296660905329, \quad u2 = -0.00691021332387476567 \\
Iteration \quad 5: \quad & u1 = -0.00017196010327221421, \quad u2 = -0.00015365106811884594 \\
Iteration \quad 6: \quad & u1 = -0.00000008233409869309, \quad u2 = -0.00000007637731775707 \\
Iteration \quad 7: \quad & u1 = -0.00000000000001935581, \quad u2 = -0.00000000000001841040
\end{aligned}
$$

The second test result with $u_0 = [0.85, 0.35]$:

$$
\begin{aligned}
Iteration \quad 1: \quad & u1 = 0.81136363636363639795, \quad u2 = 0.10681818181818181213 \\
Iteration \quad 2: \quad & u1 = 1.12168872806060271330, \quad u2 = -0.06562528280994642249 \\
Iteration \quad 3: \quad & u1 = 1.01624470697865687541, \quad u2 = -0.00857178236204569205 \\
Iteration \quad 4: \quad & u1 = 1.00037706830737005426, \quad u2 = -0.00019555153336901603 \\
Iteration \quad 5: \quad & u1 = 1.00000021293148022572, \quad u2 = -0.00000010910928069496 \\
Iteration \quad 6: \quad & u1 = 1.00000000000006794565, \quad u2 = -0.00000000000003456074
\end{aligned}
$$

The solution converges at the 7th iteration in the first test see figure 2.3 and at the 6th iteration in the second test figure 2.4.
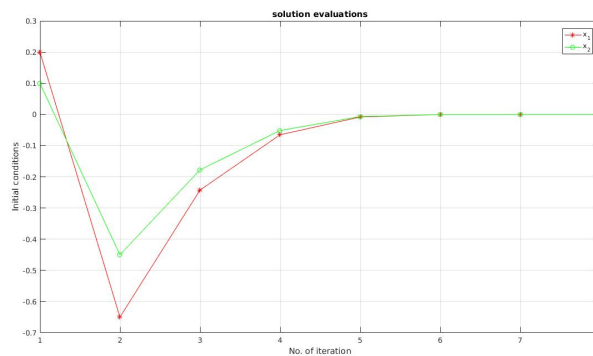
Figure 2.3: Convergence of solutions g(u_1, u_2) with Newton-Raphson method. Initial conditions: $u_1(0) = 0.2$ and $u_2(0) = 0.1$
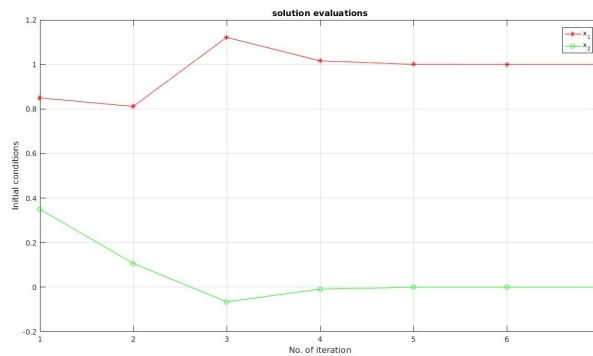
Figure 2.4: Convergence of solutions g(u_1, u_2) with Newton-Raphson method. Initial condition: $u_1(0) = 0.85$ and $u_2(0) = 0.35$

The choice of the initial conditions influences the convergence of the algorithm. The 2 solutions can be obtained after 2 or 3 iterations thanks to the good choice of the initial conditions.

2.3.1 Reviewing of the classical theorem of convergence

The classical method study the solution of a nonlinear problem by solving a sequence of linear problems. In the Newton-Raphson method, the solution of linear problems is based on necessary assumptions

such that the Jacobian matrix must be invertible over the whole domain. For this reason, standard convergence theorems generally require a-priori the existence of the inverse of the Jacobian matrix and that is bounded[22]. For the inverse of the Jacobian matrix $\mathscr{K}_T(u)^{-1}$ there exists $\eta > 0$ where:

$$\|\mathscr{K}_T(u)^{-1}\| \leq \eta \tag{2.19}$$

From a computational point of view, The theoretical quantity η may be difficult to obtain in the domain Ω_0. In this case, a local estimation sample seems preferable such as:

$$\|\mathscr{K}_T(\bar{u})^{-1}\| \leq \eta_0 \tag{2.20}$$

Where $\bar{u} \in \mathcal{V}_0(\Omega_0)$ is the approximate solution exists in the admissible solution space, and η_0 is the upper bound quantity of the local estimation of $\mathscr{K}_T$. In order to study the affinity properties of the above Newton iteration, some information about the second derivative is needed. The classic standard form for including this information is via the Lipschitz condition with constant γ ($\gamma > 0$) as follows:

$$\|\mathscr{K}_T(u) - \mathscr{K}_T(\bar{u})\| \leq \gamma \|u - \bar{u}\| \quad \text{with } u, \bar{u} \in \Omega_0 \tag{2.21}$$

the two assumptions eq.2.20 and eq.2.21 are necessary in the method of Newton-Raphson to show the existence and the uniqueness of a solution. Moreover, the quadratic convergence of the iterations of Newton-Raphson in a neighborhood characterized by a quantity known as of Kantorovich such as:

$$\eta_0 \gamma < \frac{1}{2} \tag{2.22}$$

2.3.2 Kantorovich's theorem

Newton's method has become ubiquitous in numerical and symbolic calculations. On specific functions such as degree two polynomials over real numbers, the behavior of this operator can be simple, but in general it is difficult to determine whether the iterations of a given point converge to zero or not[39]. More precisely, in theory, it is classic for Newton's sequences to quadratically converge if their initial value u_0 is sufficiently close to a simple zero u^*. But for practice, this information is not sufficient, and it is necessary to quantify what is meant by sufficient. The famous hypothesis used as a sufficient condition for the convergence of Newton's method is from Kantorovich [60]. Kantorovich's theorem is a mathematical statement on the semi-local convergence of Newton's method. This theorem is stated in Banach spaces-well aware of the fact that a Banach space formulation is not directly applicable to numerical methods: in the numerical solution of the equations of nonlinear operators, we must take into account both function and derivative approximations. Consequently, Newton's inaccurate methods in Banach spaces are the correct theoretical framework for studying the convergence of algorithms. Kantorovich's theorem for continue nonlinear systems is as follows:

Theorem 1 *Kantorovich's theorem asserts that the iterative method of Newton, applied to a most general system of nonlinear equation $f(u) = 0$, converges to a solution u^* near some given point $\bar{u}$. f is defined in $\mathcal{V}_0 \subset \mathbb{B}$. Where $\mathbb{B}$ is Banach space.*
Assume for some $\bar{u} \in \mathcal{V}_0$ that $[f'(\bar{u})]^{-1}$ exists and that:

$$\exists \alpha > 0: \quad \|f'(\bar{u})^{-1} f(\bar{u})\|_{L^2} \leq \alpha. \tag{2.23}$$

$$\exists \beta > 0, \ \forall u, v \in \mathbb{B}(\bar{u}, 2\alpha): \quad \|f'(\bar{u})^{-1} \left(f'(u) - f'(v) \right)\|_{L^2} \leq \beta \|u - v\|_{L^2}. \tag{2.24}$$

if $\beta\alpha \leq \frac{1}{2}$, then f has a unique solution u^* in the ball $\mathbb{B}(\bar{u}, \xi = \frac{1-\sqrt{1-2\alpha\beta}}{\beta})$

The first condition eq 2.23 is for bounded the error estimate of the nonlinear equation $f(u) = 0$. The second condition eq 2.24 is for verified the Lipschitz condition. Under the two conditions, we can obtain the error estimates, the regions of existence and uniqueness of solutions and know that $\bar{u}$ is an initial convergent point.

Example

Taking the previous example. For the first condition eq 2.23 we have:

$$\|g'(\bar{u})^{-1}g(\bar{u})\|_{L^2} \quad \leq \|g'(\bar{u})^{-1}\|_{L^2}\|g(\bar{u})\|_{L^2}. \tag{2.25}$$

$$\leq \left\| \begin{bmatrix} 2\bar{u}_1 + 2\bar{u}_2 - 1 & 2\bar{u}_1 \\ 2\bar{u}_2 & 2\bar{u}_2 + 2\bar{u}_1 - 1 \end{bmatrix} \right\|_{L^2} \left\| \begin{bmatrix} \bar{u}_1^2 + 2\bar{u}_1\bar{u}_2 - \bar{u}_1 \\ \bar{u}_2^2 + 2\bar{u}_1\bar{u}_2 - \bar{u}_2 \end{bmatrix} \right\|_{L^2} \tag{2.26}$$

For the second condition we must prove that $g(u)$ is β-Lipschitz. Using definition in [3] we have

$$\forall u, v \in \mathbf{R}^2: \quad \|g'(\bar{u})^{-1}\left(g'(u) - g'(v)\right)\|_{L^2} \leq \|g'(\bar{u})^{-1}\|_{L^2}\|u - v\|_{L^2}. \tag{2.27}$$

Where

$$\beta = max(\|g'(\bar{u})^{-1}\|_{L^2}) \tag{2.28}$$

For the initial conditions $\bar{u} = [0.85\ 0.35]$ we have $\alpha = 0.2462$, $\beta = 2.6866$, then $\alpha\beta = 0.6615 > \frac{1}{2}$ so the condition of Kantorovich's is not verified. But, for the initial conditions $\bar{u} = [0.9\ 0.2]$ we obtain $\alpha = 0.19$, $\beta = 2.4892$, then $\alpha\beta = 0.4730 < \frac{1}{2}$ and $\xi = 0.3084$ so the theorem is verified. Figure 2.5 show the better convergence of solution comparing with figure 2.4.
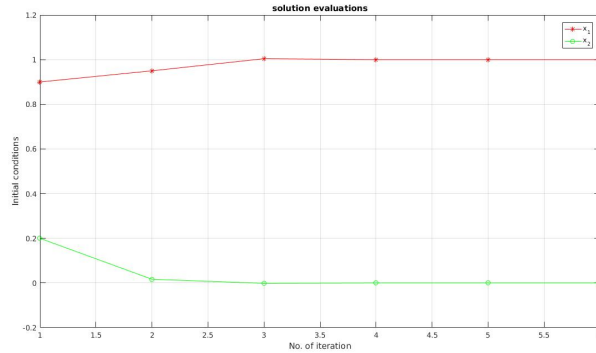
Figure 2.5: Convergence of solutions $g(u_1, u_2)$ with initial condition: $u_1(0) = 0.9$ and $u_2(0) = 0.2$

2.4 Newton-Raphson algorithm with finite element for solving nonlinear minimum energy problem

2.4.1 Solving continuum mechanics with Finite element

The famous method to solve nonlinear problems in continuum mechanics is the finite element. This method discretizes the domain Ω_0 into $\mathscr{M}$ geometrical element with N points$(x_1, .., x_N \in \Omega_0)$. These points are named the nodes of the organ (see figure 2.6).
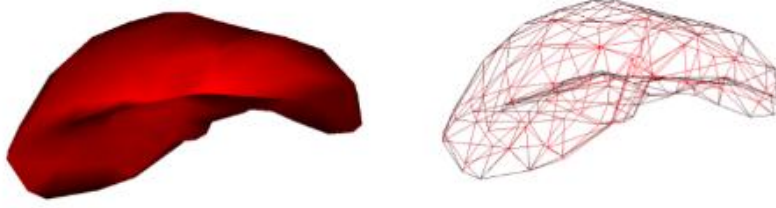
Figure 2.6: Liver representation with FEM.

So, the sub-discretized organ becomes $\Omega_h = \cup_{e=1}^{\mathcal{M}} \omega_h^e \subset \Omega_0$. Where ω_h^e is the e-th element which is composed of n nodes (e.g 4 nodes for tetrahedral element or 8 nodes for hexahedral element).
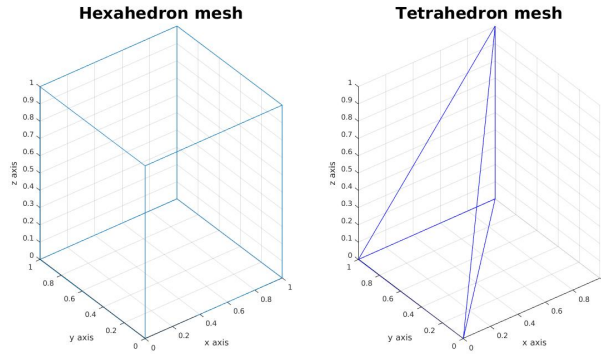
Figure 2.7: Representation of tetrahedral and hexahedral element.

Let the vector $(\varphi_1, \varphi_2, .., \varphi_N)$ a base of $\mathcal{V}_h$, where $\mathcal{V}_h(\Omega_h)$ represent the Sobolev spaces of the sub-discretized organ. We can define it as follow [8]:

$$\mathcal{V}_h(\Omega_h) = \mathrm{span}(\varphi_1, \cdots, \varphi_N) \subset \mathcal{V}_0(\Omega) \tag{2.29}$$

This vector is known by the shape functions and is defined as $\varphi_I : \mathbf{R}^3 \to [0,1]$ with $I = 1, .., N$. These shape functions are associated to the nodes of the mesh and must satisfy certain properties as:

$$\varphi_I(x_I) = \epsilon_{ij} \tag{2.30}$$
$$\sum_{I=1}^{N} \varphi_I = 1 \tag{2.31}$$

Where ϵ_{ij} is the kronecker symbol and x_I is the 3D coordonate of node I. By projection of the space $\mathcal{V}_0(\Omega)$ onto a finite dimensional Hilbert space $\mathcal{V}_h(\Omega_h)$, we define $\mathbf{f}_h$ where is the projection of $\mathbf{f}$. Hence, for each $\mathbf{f}_h \in \mathcal{V}_h(\Omega_h)$ there exist its projection $\mathbf{f} \in \mathcal{V}_0(\Omega)$ such that the projection can be written as

$$\Pi_h : \mathcal{V}_0(\Omega) \to \mathcal{V}_h(\Omega_h) : \mathbf{f} \mapsto \Pi_h(\mathbf{f})(x) = \mathbf{f}_h(x) = \sum_{I=1}^{N} \mathbf{f}(x_I)\varphi_I(x), \ x \in \Omega_0 \tag{2.32}$$

Where, the projection $\mathbf{f}_h(x)$ can be represented by the vector $\mathbf{F}_h$ as

$$\mathbf{F}_h = (\mathbf{f}(x_1), \cdots, \mathbf{f}(x_N))^\top \tag{2.33}$$

So, we can denote the projected version of a continuous functional $\mathbf{f}$ as follow:

$$\mathbf{f}_h = \Pi_h(\mathbf{f}) \tag{2.34}$$

According to the notation used in section 1.3. Let us define the displacement u (see figure 2.8). Where, $u \in \mathcal{V}_0(\Omega)$ caused by the deformation of the organ at rest Ω_0.
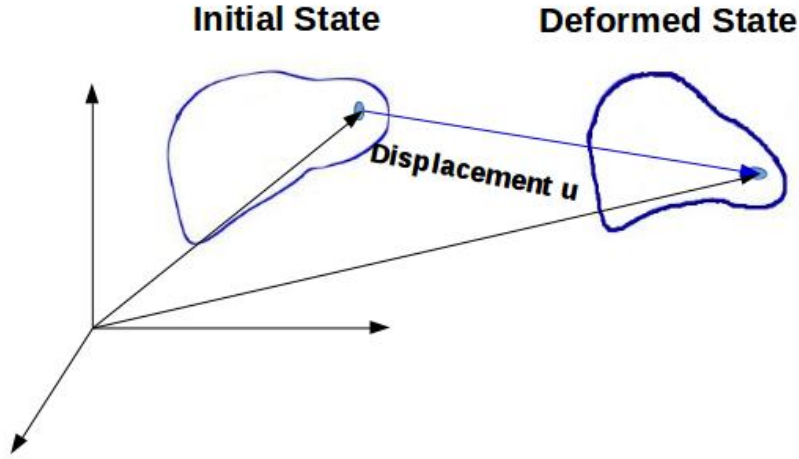
Figure 2.8: Representation of displacement field u.

The discretized displacement is defined as $u_h \in \mathcal{V}_h(\Omega_h)$ where can be represented by the $3N$-vector as

$$U = \left(u(x_1)^\top, \cdots, u(x_N)^\top\right)^\top \tag{2.35}$$

U is called the global displacement vector and the displacement at node I, $1 \le I \le N$ is represented by $u(x_I) \in \mathbf{R}^3$.

To solve the nonlinear problem of eq 1.31 defined in section 1.3.2. In first step, it is necessary to calculate the analytical linearization of the residue with respect to u. Next, using the finite element discretization to approximate the integrals with summations over the reference domain Ω_0. Finally, an iterative process used to find the solution of the discrete problem.

Linearization

To solve the nonlinear problem using an iterative process, it is necessary to linearize the nonlinear functions. Hence, we know that the residual eq 1.28 is nonlinear in the displacement u. For linearize it we consider a displacement $\overline{\overline{u}}$ such as $\overline{\overline{u}} \in \mathcal{V}_0(\Omega)$. The linearized residual is defined as follows [33]:

$$\mathbf{r}(u, \hat{u}) \quad = a(u, \hat{u}) - l(\hat{u}) \tag{2.36}$$

$$\mathbf{r}(u, \hat{u})_{\delta\overline{\overline{u}}} \quad = \frac{\partial a}{\partial u} \delta\overline{\overline{u}} + a(\overline{\overline{u}}, \hat{u}) - l(\overline{\overline{u}}) \tag{2.37}$$

Where $\delta\overline{\overline{u}} = u - \overline{\overline{u}}$. $\frac{\partial a}{\partial u}$ is the Fréchet derivative of internal form a at $\overline{\overline{u}}$ with respect to the displacement u. We note the Fréchet derivative of a by $\mathcal{F}_a$.

So, the linearization of the residual can be written as

$$\mathbf{r}(u, \hat{u})_{\delta\overline{\overline{u}}} = \mathcal{F}_a(\overline{\overline{u}}, \hat{u}) \, \delta\overline{\overline{u}} + a(\overline{\overline{u}}, \hat{u}) - l(\hat{u}), \text{ for all } \hat{u} \in \mathcal{V}_0(\Omega_0), \tag{2.38}$$

Using the relation in eq1.30 the Fréchet derivative of the nonlinear operator $R'(u)$ with a bilinear form $\{\cdot, \cdot\}$ can be defined as follows

$$\left\{ R'(\overline{\overline{u}}), \hat{u} \right\} := \mathcal{F}_a(\overline{\overline{u}}, \hat{u}), \text{ for all } \hat{u} \in \mathcal{V}_0(\Omega_0). \tag{2.39}$$

The formal expression of $\mathcal{F}_a(\overline{\overline{u}}, \hat{u})$ is derived from the expression of $a(u, \hat{u})$ as follows [33]

$$\mathcal{F}_a(\overline{\overline{u}}, \hat{u})\delta\overline{\overline{u}} = \oint_{\Omega_0} \text{sym}(\nabla_0\hat{u}^\top F(\overline{\overline{u}})) : \mathscr{D}(\overline{\overline{u}}) : \text{sym}(\nabla_0\delta\overline{\overline{u}}F(\overline{\overline{u}})) + \mathscr{S}(\overline{\overline{u}}) : \text{sym}\left(\nabla_0\hat{u}^\top\nabla_0\delta\overline{\overline{u}}\right) \, d\Omega \tag{2.40}$$

Where sym(.) is the symmetry operator for matrices. ∇_0 is the gradient operator computed with respect to the coordinate frame at rest.

Discretization

Using the discretized domain for represented an organ by a 3D mesh. Each element of mesh is represented by $3n$ number of DOF (see figure 2.9). All elements of the mesh are represented by $3N$ number of DOF.
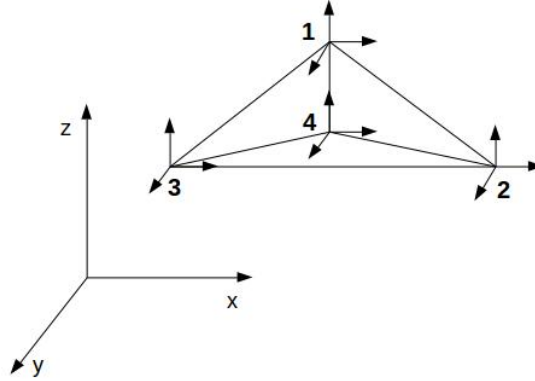
Figure 2.9: Nodal representation of tetrahedral element.

Let be the displacement vector $\overline{\overline{U}}_h^e \in \mathbf{R}^{3n}$ associated for each element which takes the nodes' element from rest to deformed state. Let consider the global nodal displacement vector $\overline{\overline{U}}_h \in \mathbf{R}^{3N}$ constructed by row-wise concatenating the N displacements of each node.

The change from local element index to global index is done by mapping index η. Where, it takes the element index e, $1 \le e \le \mathcal{M}$, as well as the DOF index of the local element i, $1 \le i \le 3n$ and maps it to the global DOF by $\eta(e, i)$, $1 \le \eta(e, i) \le 3N$. We know in the finite element method that each element has an elementary tangential stiffness matrix $\kappa_{\omega^e}(\overline{\overline{U}}_h^e)$ of size $3n \times 3n$. For a given displacement $\overline{\overline{U}}_h^e$, the nonlinear strain properties are encoded in the elementary stiffness matrix. For convenience, we consider an extension of κ_{ω^e} to $\mathscr{K}_{\omega^e}$ which is of size $3N \times 3N$. This extended matrix is obtained by filling with

zeros the extended rows and columns which can be written as :

$$\mathscr{K}_{\omega^e}(\overline{\overline{U}}_h)[j,l] = \begin{cases} \kappa_{\omega^e}(\overline{\overline{U}}_h^{\,e})[j',l'], & \text{if } (j,l) = (\eta(e,j'),\eta(e,l')) \\ 0, & \text{else.} \end{cases} \quad, 1 \le i,j \le 3N, \ 1 \le i',j' \le 3n. \quad (2.41)$$
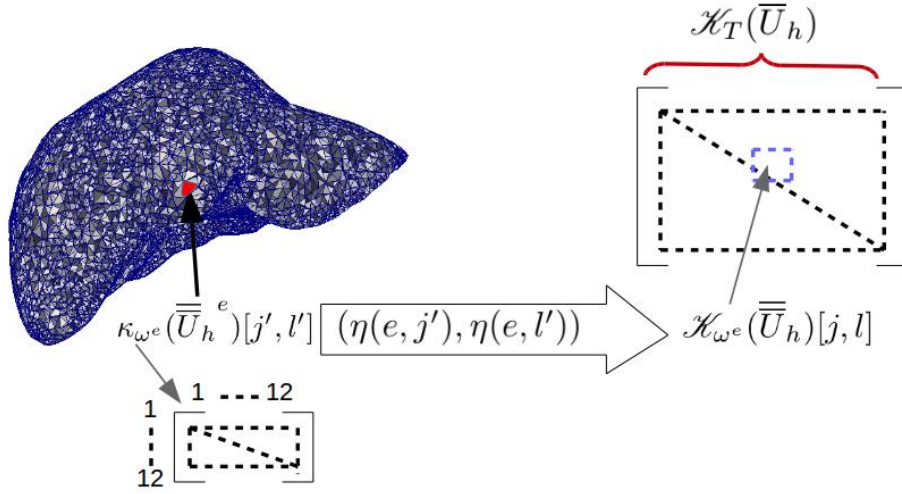

Figure 2.10: Mapped the tangential stiffness matrix of tetrahedron element into the global tangential stiffness matrix.

After calculation of the elementary tangential matrices. An assembly process will gather all these matrices in a global tangential stiffness matrix $\mathscr{K}_T(\overline{\overline{U}}_h)$ of size $3N \times 3N$ (see figure 2.10). If the mesh is deformed according to an external force or an imposed displacement the total behavior of this mesh will be encoded in the total tangential stiffness matrix. We can express the assembly of the elementary tangential matrices by the following formula:

$$\mathscr{K}_T(\overline{\overline{U}}_h) = \sum_{e=1}^{\mathscr{M}} \mathscr{K}_{\omega^e}(\overline{\overline{U}}_h^{\,e}). \quad (2.42)$$

Thus the discretization of eq 2.40 can be written as [33]

$$\Pi_h\left(\mathcal{F}_a(\overline{u},\hat{u})\delta\overline{u}\right) \coloneqq \mathcal{F}_{a,h}(\overline{u}_h,\hat{u}_h)\delta\overline{u}_h = \hat{U}_h^\top \mathscr{K}_T(\overline{\overline{U}}_h)\Delta\overline{\overline{U}}_h. \quad (2.43)$$

Where $\Delta\overline{\overline{U}}_h = U - \overline{\overline{U}}_h$ is the global incremental displacement. This equation gives a direct link between the formal projection and its numerical representation. Replaces eq 2.43 in the eq 2.39, it gives us the numerical definition of the Fréchet derivative $R'_h(\overline{\overline{u}}_h)$

$$R'_h(\overline{\overline{u}}_h) \coloneqq \mathscr{K}_T(\overline{\overline{U}}_h) \quad (2.44)$$

So, the numerical estimation for the L^2-norm of the Fréchet derivative $R'_h(\overline{\overline{u}}_h)$ and its inverse are as follow:

$$\|R'_h(\overline{\overline{u}}_h)\|_{L^2} = \left\| \|\mathscr{K}_T(\overline{\overline{U}}_h)\|_F \right\|_{L^2}, \quad (2.45)$$

$$\|R_h'(\overline{\overline{u}}_h)^{-1}\|_{L^2} = \left\|\|\mathscr{K}_T(\overline{\overline{U}}_h)^{-1}\|_F\right\|_{L^2}. \tag{2.46}$$

Now, using the relation eq 1.30 we can write

$$\left\{R(\overline{\overline{u}}), \hat{u}\right\} := a(\overline{\overline{u}}, \hat{u}) - l(\hat{u}) \tag{2.47}$$

So, the residual eq 2.38 can be write as

$$\mathbf{r}(u, \hat{u})_{\delta\overline{\overline{u}}} = \mathcal{F}_a(\overline{\overline{u}}, \hat{u})\,\delta\overline{\overline{u}} + \left\{R(\overline{\overline{u}}), \hat{u}\right\} \tag{2.48}$$

Using the global tangential stiffness matrix to discretize the linearized residual 2.48, we obtain

$$\{\Pi_h R(u), \Pi_h \hat{u}\} := \hat{U}_h^\top \mathscr{K}_T(\overline{\overline{U}}_h)\Delta\overline{\overline{U}}_h + \hat{U}_h^\top R(\overline{\overline{U}}_h). \tag{2.49}$$

This equation is valid for every $\hat{u} \in \mathcal{V}_0(\Omega_0)$, therefore we obtain the following classic formula

$$R_h(u_h) = \mathscr{K}_T(\overline{\overline{U}}_h)\Delta\overline{\overline{U}}_h + R_h(\overline{\overline{u}}_h). \tag{2.50}$$

The computation of $\mathscr{K}$ and R are based on three task. The mesh of an organ represented by FEM requires the shape functions (linear, polynomial, etc.), the type of the constitutive model (Mooney-Rvilin, Saint Venant-Kirchhoff, etc.) and the type of primitives that make up the element (tetrahedron, hexahedron, etc.). We can write the

(iii) *Iteration.* The generic iterative algorithm can be define with the following steps

1. $k = 0$, $\overline{\overline{U}}_{h,0} = 0$, $R(\overline{\overline{u}}_{h,0})$, $\mathscr{K}_T(\overline{\overline{U}}_{h,0})$, [initialization];

2. $\Delta\overline{\overline{U}}_{h,k} = -\left(\mathscr{K}_T(\overline{\overline{U}}_{h,k})\right)^{-1} R(\overline{\overline{u}}_{h,k})$, $k > 0$, [Computing incremental displacement];

3. $\overline{\overline{U}}_{h,k+1} = \overline{\overline{U}}_{h,k} + \Delta\overline{\overline{U}}_{h,k}$, [Updating global displacement];

4. $R(\overline{\overline{u}}_{h,k+1})$, [Updating residual];

5. $\|R(\overline{\overline{U}}_{h,k+1})\|_{L^2} < \epsilon$, [Stop criterion].

6. $\mathscr{K}_T(\overline{\overline{U}}_{h,k+1})$, [Updating tangential stiffness];

7. $k = k + 1$ [Next increment];

8. go to line 2, [Loop];

So far, we have defined the discrete space using finite elements to solve the problem in the continuous medium. In the next section, we define hypothesis that allow us to numerically evaluate the radius of convergence.

2.4.2 Assumptions in the context of surgical simulation

The finite element method formulated in displacement requires a convergence criterion when it is used in nonlinear mechanics with iterative resolution algorithms. This convergence criterion aims to measure the proximity of the stress field obtained with the equilibrium. Therefore, three hypotheses have been proposed in this section to improve the radius of convergence. Let assume the following:

Assumption 1 *If $\mathbf{f}$ is continuously differentiable over Ω_0 then there exists a positive constant $c_1 > 0$ such that*

$$\|\{\nabla_0 \mathbf{f}\}\|_{L^2} \leq c_1 \|\mathbf{f}\|_{L^2}. \tag{2.51}$$

This hypothesis control the L^2-norm of the functional's gradient by the norm of the functional with a positive non-null constant.

Assumption 2 *If $\mathbf{f}$ is continuous over Ω_0 then there exists a positive constant $c_2 > 0$ such that*

$$\|\mathbf{f}\|_{L^2} \leq c_2 \|\mathbf{f}_h\|_{L^2}. \tag{2.52}$$

This hypothesis control the norm L^2 of the functional by the projection of the functional (it represents an interpolation error of order 0).

Assumption 3 *Let us consider $\rho(\Omega_0)$ is the volume of the continuous domain Ω_0 and $\rho(\Omega_h)$ is the volume of the discretized domain Ω_h. There exists $c_3 > 0$ such that*

$$\rho(\Omega_0) \leq c_3 \rho(\Omega_h). \tag{2.53}$$

This assumption limits the exact volume of the organ by greater value of the approximate discretized volume. The control variables c_1, c_2 and c_3 are used numerically during the experimental evaluation of the convergence radius. For the chosen constants, we evaluate how close the approximate solution is to the exact solution. The following lemma establishes an upper bound of the L^2-norm of a tensor functional given the above assumptions.

Lemma 1 *Let us consider an element $u \in \mathcal{V}_0(\Omega)$ and its projection $u_h \in \mathcal{V}_h(\Omega_h)$. If we consider a continuous tensor functional $\mathcal{M}$ evaluated at u then there exists a constant $c_2 > 0$ as defined in assumption 3 such that*

$$\|\|\mathcal{M}(u)\|_F\|_{L^2} \leq c_2 \sqrt{c_3 \rho(\Omega_h)} \|\mathcal{M}_h(u_h)\|_F. \tag{2.54}$$

Where $\mathcal{M}_h$ is the projection of $\mathcal{M}$ onto $\mathcal{V}_h(\Omega_h)$.

Proof 1 *On the one hand, we consider from assumption 3 that*

$$\|\|\mathcal{M}(u)\|_F\|_{L^2} \leq c_2 \|\|\mathcal{M}_h(u_h)\|_F\|_{L^2} \tag{2.55}$$

On the other hand, we have from equations 2.1 and 2.4

$$\|\|\mathcal{M}_h(u_h)\|_F\|_{L^2}^2 := \oint_\Omega \sum_{i=1}^n \{\mathcal{M}_h(u_h)\}_i^2 \, d\Omega \tag{2.56}$$

$$\leq \sum_{i=1}^n \{\mathcal{M}_h(u_h)\}_i^2 \rho(\Omega_0) \tag{2.57}$$

$$\leq c_3 \rho(\Omega_h) \|\mathcal{M}_h(u_h)\|_F^2, \ by \ assumption \ 2. \tag{2.58}$$

Combining 2.55 and 2.58 concludes the proof.

2.4.3 Contribution 1: Convergence checking with Kantorovich theorem

In this section, we compute the radius of convergence by using Kantorovich's theorem [37] as is discussed in section 2.3.2. We recall this theorem with our notations as follows

Theorem 2 *Let us consider the nonlinear functional* $R : \mathcal{V}_0(\Omega_0) \to \mathcal{V}_0(\Omega_0)$. *We assume that for* $\bar{u} \in \mathcal{V}_0(\Omega_0)$, *the Fréchet derivative* $R'(\bar{u})$ *exists, is non-singular and satisfies:*

$$\exists \alpha > 0 : \quad \|R'(\bar{u})^{-1} R(\bar{u})\|_{L^2} \leq \alpha. \tag{2.59}$$

Furthermore, we assume the following

$$\exists \beta > 0, \ \forall \mathbf{u}, \mathbf{v} \in \mathbb{B}(\bar{u}, 2\alpha) : \quad \|R'(\bar{u})^{-1} \left(R'(\mathbf{u}) - R'(\mathbf{v}) \right)\|_{L^2} \leq \beta \|\mathbf{u} - \mathbf{v}\|_{L^2}. \tag{2.60}$$

If $\alpha\beta \leq \frac{1}{2}$ *then problem 1.31 has a unique solution* u^* *in the ball* $\mathbb{B}(\bar{u}, \xi = \frac{1-\sqrt{1-2\alpha\beta}}{\beta})$.

The most difficult task in using this theorem is to estimate $\|R'(\bar{u})^{-1}\|_{L^2}$. Where, we have no formal expression which represents the inverse of the Fréchet derivative of the residue $R'(\bar{u})$. Fortunately, there exists a lemma [50, 66] which allows to bound this inverse given that the discretized derivative of Fréchet is bounded and given that the difference of these two linear operators is also bounded. We integrate this lemma with our notations as follows

Lemma 2 *Let* $\bar{u}_h$ *be the approximate solution of equation 1.31. Let us consider that the discretized linear operator of the Fréchet derivative* $R'_h(\bar{u}_h)$ *is bounded and has a bounded inverse*

$$\| \left(R'_h(\bar{u}_h) \right)^{-1} \|_{L^2} \leq \gamma. \tag{2.61}$$

Let's further assume that the difference between the linear operators $R'(\bar{u})$ *and* $R'_h(\bar{u}_h)$ *is bounded*

$$\|R'(\bar{u}) - R'_h(\bar{u}_h)\|_{L^2} \leq \eta. \tag{2.62}$$

If $\gamma\eta < 1$, *then* $R'(\bar{u})$ *is a bijection and*

$$\|R'(\bar{u})^{-1}\|_{L^2} \leq \frac{\gamma}{1 - \gamma\eta}. \tag{2.63}$$

The upper bound of the Fréchet derivative of the residual $R'(\bar{u})$ is computed when the upper bounds γ and η referenced in the inequalities 2.61 and 2.62 are estimated. Therefore, we have proposed the following two propositions

Proposition 1 *Given the conditions of lemma 2, the upper boundaries of inequalities 2.61 and 2.62 are given by*

1.

$$\gamma = c_2 \sqrt{c_3 \rho(\Omega_h)} \, \|\mathscr{K}_T(\overline{U}_h)^{-1}\|_F. \tag{2.64}$$

2.

$$\eta = 3c_1^2 c_2 \left(3c_2^2 \|\{F_h(\bar{u}_h)\}\|_{L^2}^2 \|\{\mathscr{D}_h(\bar{u}_h)\}\|_{L^2} + \|\{\mathscr{S}_h(\bar{u}_h)\}\|_{L^2} \right) + c_2 \sqrt{c_3 \rho(\Omega_h)} \, \|\mathscr{K}_T(\overline{U}_h)\|_F. \tag{2.65}$$

Proof 2   *1. To find* γ *it's simple, we take equation 2.46 and lemma 1 and we combine them. We come out with this following formula*

$$\| \left(R'_h(\bar{u}_h) \right)^{-1} \|_{L^2} \leq \left\| \|\mathscr{K}_T(\overline{U}_h)^{-1}\|_F \right\|_{L^2} \tag{2.66}$$

$$\leq c_2 \sqrt{c_3 \rho(\Omega_h)} \, \|\mathscr{K}_T(\overline{U}_h)^{-1}\|_F. \tag{2.67}$$

2. To find η, the first step is to find the upper bound of $\|R'_h(\bar{u}_h)\|_{L^2}$ which is similar to the previous reasoning. We take equation 2.45 and lemma 1 and we combine them.

$$\|R'_h(\bar{u}_h)\|_{L^2} \leq \boldsymbol{c_2}\sqrt{\boldsymbol{c_3}\rho(\Omega_h)} \; \|\|\mathcal{K}_T(\overline{U}_h)\|_F\|_{L^2} \tag{2.68}$$

The second step, we find an upper bound for $\|R(\bar{u})'\|_{L^2}$ with applying the absolute value operator $|\cdot|$ on both sides of equation 2.40 where leads to the following inequalities

$$|\mathcal{F}_a(\overline{\overline{u}},\hat{u})\delta\overline{\overline{u}}| = |\oint_{\Omega_0} sym(\nabla_0\hat{u}^\top F(\overline{\overline{u}})) : \mathscr{D}(\overline{\overline{u}}) : sym(\nabla_0\delta\overline{\overline{u}}F(\overline{\overline{u}})) \; + \; \mathscr{S}(\overline{\overline{u}}) : sym\left(\nabla_0\hat{u}^\top\nabla_0\delta\overline{\overline{u}}\right) d\Omega|, \tag{2.69}$$

$$= |\oint_{\Omega_0} \{sym(\nabla_0\hat{u}^\top F(\overline{\overline{u}}))\}^\top \lfloor\mathscr{D}(\overline{\overline{u}})\rfloor\{sym(\nabla_0\delta\overline{\overline{u}}F(\overline{\overline{u}}))\} \; + \; \{\mathscr{S}(\overline{\overline{u}})\}^\top\{sym\left(\nabla_0\hat{u}^\top\nabla_0\delta\overline{\overline{u}}\right)\} d\Omega|, \tag{2.70}$$

$$\leq |\oint_{\Omega_0} \{sym(\nabla_0\hat{u}^\top F(\overline{\overline{u}}))\}^\top \lfloor\mathscr{D}(\overline{\overline{u}})\rfloor\{sym(\nabla_0\delta\overline{\overline{u}}F(\overline{\overline{u}}))\}| \; + \; |\{\mathscr{S}(\overline{\overline{u}})\}^\top\{sym\left(\nabla_0\hat{u}^\top\nabla_0\delta\overline{\overline{u}}\right)\} d\Omega| \; . \tag{2.71}$$

Where the operator $\lfloor\cdot\rfloor$ transforms the 4-tensor of $\mathscr{D}$ to a 2-tensor while preserving the initial contraction product. In this case, the contraction products involving 2-tensors and 4-tensors in equation 2.69 are transformed to matrix vector products in equation 2.70. Using the triangular inequality, we obtained the derived 2.71. Applying Cauchy-Schwarz inequality [9] gives the following

$$|\mathcal{F}_a(\overline{\overline{u}},\hat{u})\delta\overline{\overline{u}}| \leq \left\|\{sym(\nabla_0\hat{u}^\top F(\overline{\overline{u}}))\}\right\|_{L^2} \left\|\lfloor\mathscr{D}(\overline{\overline{u}})\rfloor\{sym(\nabla_0\delta\overline{\overline{u}}^\top F(\overline{\overline{u}}))\}\right\|_{L^2} \; + \; \left\|\{\mathscr{S}(\overline{\overline{u}})\}^\top\{sym\left(\nabla_0\hat{u}^\top\nabla_0\delta\overline{\overline{u}}\right)\}\right\|_{L^2} \tag{2.72}$$

The L^2-norm being submultiplicative [9], then the norm of the product is less than or equal the product of norms

$$|\mathcal{F}_a(\overline{\overline{u}},\hat{u})\delta\overline{\overline{u}}| \leq \left\|\{sym(\nabla_0\hat{u}^\top F(\overline{\overline{u}}))\}\right\|_{L^2} \left\|\lfloor\mathscr{D}(\overline{\overline{u}})\rfloor\right\|_{L^2} \left\|\{sym(\nabla_0\delta\overline{\overline{u}}^\top F(\overline{\overline{u}}))\}\right\|_{L^2} \; + \; \left\|\{\mathscr{S}(\overline{\overline{u}})\}\right\|_{L^2} \left\|\{sym\left(\nabla_0\hat{u}^\top\nabla_0\delta\overline{\overline{u}}\right)\}\right\|_{L^2} \tag{2.73}$$

Now we address the terms of the form $sym(A^\top B)$ where A and B are matrices of dimension 3. Consider the following derivation:

$$\left\|\{sym(A^\top B)\}\right\|_{L^2} = \frac{1}{2}\left\|\{(A^\top B + B^\top A)\}\right\|_{L^2} \tag{2.74}$$

$$= \frac{1}{2}\left\|(\mathbf{I}\otimes A^\top)\{B\} + (A^\top\otimes\mathbf{I})\{B^\top\}\right\|_{L^2} \tag{2.75}$$

$$\leq \frac{1}{2}\left(\left\|(\mathbf{I}\otimes A^\top)\right\|_{L^2}\|\{B\}\|_{L^2} + \left\|(A^\top\otimes\mathbf{I})\right\|_{L^2}\left\|\{B^\top\}\right\|_{L^2}\right) \tag{2.76}$$

$$\leq \frac{1}{2}\left(3\left\|\{A^\top\}\right\|_{L^2}\|\{B\}\|_{L^2} + 3\left\|\{A^\top\}\right\|_{L^2}\left\|\{B^\top\}\right\|_{L^2}\right) \tag{2.77}$$

$$\leq 3\|\|A\|_F\|_{L^2}\|\|B\|_F\|_{L^2} \tag{2.78}$$

Where, $\otimes$ denote the dyadic product and $\mathbf{I}$ is the identity matrix of dimension 3. Using this result in the inequality terms eq 2.73, we find the following inequality

$$|\mathcal{F}_a(\overline{\overline{u}},\hat{u})\delta\overline{\overline{u}}| \leq 3\left(3\left\|\{F(\overline{\overline{u}})\}\right\|_{L^2}^2\left\|\{\mathscr{D}(\overline{\overline{u}})\}\right\|_{L^2} \; + \; \left\|\{\mathscr{S}(\overline{\overline{u}})\}\right\|_{L^2}\right)\|\{\nabla_0\hat{u}\}\|_{L^2}\|\{\nabla_0\delta\overline{\overline{u}}\}\|_{L^2} \tag{2.79}$$

$$\leq 3\boldsymbol{c_1^2}\left(3\left\|\{F(\overline{\overline{u}})\}\right\|_{L^2}^2\left\|\{\mathscr{D}(\overline{\overline{u}})\}\right\|_{L^2} \; + \; \left\|\{\mathscr{S}(\overline{\overline{u}})\}\right\|_{L^2}\right)\|\{\hat{u}\}\|_{L^2}\|\{\delta\overline{\overline{u}}\}\|_{L^2} \; , \; by \; assumption \; 1. \tag{2.80}$$

44

Thus, one can set

$$|\mathcal{F}_a(\overline{\overline{u}}, \hat{u})| \leq 3\boldsymbol{c}_1^2 \left(3 \left\| \{F(\overline{\overline{u}})\} \right\|_{L^2}^2 \left\| \{\mathscr{D}(\overline{\overline{u}})\} \right\|_{L^2} + \left\| \{\mathscr{S}(\overline{\overline{u}})\} \right\|_{L^2} \right) \left\| \hat{u} \right\|_{L^2} \left\|_{L^2}. \tag{2.81}$$

Given the definition 2.39 and replacing $\overline{\overline{u}}$ by the approximate solution $\bar{u}$, we can put

$$\|R(\bar{u})'\|_{L^2} \leq 3\boldsymbol{c}_1^2 \left(3 \left\| \{F(\bar{u})\} \right\|_{L^2}^2 \left\| \{\mathscr{D}(\bar{u})\} \right\|_{L^2} + \left\| \{\mathscr{S}(\bar{u})\} \right\|_{L^2} \right). \tag{2.82}$$

Applying the link of passage from continuous to discrete entities by lemma 1, we obtain

$$\|R(\bar{u})'\|_{L^2} \leq 3\boldsymbol{c}_1^2 \boldsymbol{c}_2 \left(3\boldsymbol{c}_2^2 \left\| \{F_h(\bar{u}_h)\} \right\|_{L^2}^2 \left\| \{\mathscr{D}_h(\bar{u}_h)\} \right\|_{L^2} + \left\| \{\mathscr{S}_h(\bar{u}_h)\} \right\|_{L^2} \right). \tag{2.83}$$

In this step, we use the triangular inequality on $\|R'(\bar{u}) - R'_h(\bar{u})\|_L^2$ and the bounds found in eq 2.68 and eq 2.68. Finally, we find an upper bound of the norm of the difference between the continuous derivative of the residual and its discrete version

$$\|R'(\bar{u}) - R'_h(\bar{u})\|_{L^2} \leq \|R'(\bar{u})\|_{L^2} + \|R'_h(\bar{u})\|_{L^2} \tag{2.84}$$

$$\leq 3\boldsymbol{c}_1^2 \boldsymbol{c}_2 \left(3\boldsymbol{c}_2^2 \left\| \{F_h(\bar{u}_h)\} \right\|_{L^2}^2 \left\| \{\mathscr{D}_h(\bar{u}_h)\} \right\|_{L^2} + \left\| \{\mathscr{S}_h(\bar{u}_h)\} \right\|_{L^2} \right) + \boldsymbol{c}_2 \sqrt{\boldsymbol{c}_3 \rho(\Omega_h)} \left\| \|\mathscr{K}_T(\overline{U}_h)\|_F \right\|_{L^2} \tag{2.85}$$

Proposition 2   *1. if $\gamma\eta < 1$ then we can define the bounds of Kantorovich's theorem 2 as follows*

$$\alpha = \frac{\gamma}{1 - \gamma\eta} \left(3\boldsymbol{c}_1 \boldsymbol{c}_2^2 \left\| \{F_h(u_h)\} \right\|_{L^2} \left\| \{\mathscr{S}_h(u_h)\} \right\|_{L^2} + \boldsymbol{c}_2 \left\| \{\mathbf{f}_h^b\} \right\|_{L^2} \right). \tag{2.86}$$

$$\beta = 27\boldsymbol{c}_1^3 \boldsymbol{c}_2^2 \boldsymbol{c}_3 \rho(\Omega_h) \frac{\gamma}{1 - \gamma\eta} \max_{u_h \in \mathbb{B}(\bar{u}_h, 2\alpha)} \left(\|\mathscr{D}_h(u_h)\|_F \|F_h(u_h)\|_F \right). \tag{2.87}$$

Thus if $\alpha\beta \leq \frac{1}{2}$, the exact solution of problem 1.31 is within the ball centered at the estimated displacement $\bar{u}$ and a radius estimated with $\xi = \frac{1 - \sqrt{1 - 2\alpha\beta}}{\beta}$.

Proof 3 *To find α, it is necessary to establish an upper bound of the residual at the estimated displacement. Using the triangular inequality and the equation 1.30, gets us*

$$|[R(u), \hat{u}]| \leq |a(u, \hat{u})| + |l(\hat{u})|, \tag{2.88}$$

$$\leq |\oint_{\Omega_0} \mathscr{S}(u) : sym\left(\nabla_0 \hat{u}^\top F(u)\right) d\Omega| + |\oint_{\Omega_0} \hat{u}^\top \mathbf{f}^b d\Omega|, \text{ from eqs 1.25, and 1.26,} \tag{2.89}$$

$$\leq \left(3\boldsymbol{c}_1 \left\| \{F(u)\} \right\|_{L^2} \left\| \{\mathscr{S}(u)\} \right\|_{L^2} + \left\| \{\mathbf{f}^b\} \right\|_{L^2} \right) \left\| \{\hat{u}\} \right\|_{L^2}, \text{ from eq 2.78 and assumption 1.} \tag{2.90}$$

Thus, we can put

$$\|R(u)\|_{L^2} \leq 3\boldsymbol{c}_1 \left\| \{F(u)\} \right\|_{L^2} \left\| \{\mathscr{S}(u)\} \right\|_{L^2} + \left\| \{\mathbf{f}^b\} \right\|_{L^2}, \tag{2.91}$$

$$\leq 3\boldsymbol{c}_1 \boldsymbol{c}_2^2 \left\| \{F(u)_h\} \right\|_{L^2} \left\| \{\mathscr{S}(u)_h\} \right\|_{L^2} + \boldsymbol{c}_2 \left\| \{\mathbf{f}_h^b\} \right\|_{L^2}. \tag{2.92}$$

Using this result together with lemma 2 and proposition 2.1 we can infer α as follows

$$\|R'(\bar{u})^{-1} R(\bar{u})\|_{L^2} \leq \|R'(\bar{u})^{-1}\|_{L^2} \|R(\bar{u})\|_{L^2}, \text{ submultiplicity of } L^2 \text{ norm [9],} \tag{2.93}$$

$$\leq \frac{\gamma}{1 - \gamma\eta} \left(3\boldsymbol{c}_1 \boldsymbol{c}_2^2 \left\| \{F_h(\bar{u}_h)\} \right\|_{L^2} \left\| \{\mathscr{S}_h(\bar{u}_h)\} \right\|_{L^2} + \boldsymbol{c}_2 \left\| \{\mathbf{f}_h^b\} \right\|_{L^2} \right), \tag{2.94}$$

$$= \alpha. \tag{2.95}$$

2. for finding the estimate β, we must estimate the Lipschitz constant of the Frechet derivative of $R'(u)$ for all $u \in \mathbb{B}(\bar{u}, 2\alpha)$ we take the second derivative Fréchet [33] of the residue derived from the equation 2.40

$$\mathcal{G}_a(\bar{\bar{u}}, \hat{u}, \delta u)\underline{u} = \oint_{\Omega_0} sym(\nabla_0 \hat{u}^\top \nabla_0 \underline{u}) : \mathscr{D}(u) : sym(\nabla_0 \delta u^\top F(u)) + sym(\nabla_0 \hat{u}^\top F(u)) : \mathscr{D}(u) : sym(\nabla_0 \delta u^\top \nabla_0 \underline{u}) \, d\Omega$$

$$+ \oint_{\Omega_0} sym(\nabla_0 \underline{u}^\top F(u)) : \mathscr{D}(u) : sym\left(\nabla_0 \hat{u}^\top \nabla_0 \delta u\right) \, d\Omega \tag{2.96}$$

Using similar reasoning as was developed for the first Fréchét derivative (see from eq 2.71 to eq 2.85), we can bound the second Fréchet derivative of the residual operator as follows

$$\|R''(u)\|_{L^2} \leq 27 \boldsymbol{c}_1^3 \|\{\mathscr{D}(u)\}\|_{L^2} \|\{F(u)\}\|_{L^2} . \tag{2.97}$$

Since the second Fréchet derivative is continuous on the compact set $\mathbb{B}(\bar{u}, 2\alpha)$, then it has a maximum over this set [9]

$$\|R''(u)\|_{L^2} \leq 27 \boldsymbol{c}_1^3 \max_{u \in \mathbb{B}(\bar{u}, 2\alpha)} \left(\|\{\mathscr{D}(u)\}\|_{L^2} \|\{F(u)\}\|_{L^2}\right), \tag{2.98}$$

$$\leq 27 \boldsymbol{c}_1^3 \boldsymbol{c}_3 \boldsymbol{c}_2^2 \rho(\Omega_h) \max_{u_h \in \mathbb{B}(\bar{u}_h, 2\alpha)} \left(\|\mathscr{D}_h(u_h)\|_F \|F_h(u_h)\|_F\right), \text{ by lemma 1,} \tag{2.99}$$

$$= \beta'. \tag{2.100}$$

The right hand side of 2.99 provides a Lipschitz constant of R' on $\mathbb{B}(\bar{u}, 2\alpha)$. Thus we can estimate β with the following quantity

$$\|R'(\bar{u})^{-1}\left(R'(\mathbf{u}) - R'(\mathbf{v})\right)\|_{L^2} \leq \|R'(\bar{u})^{-1}\| \, \|R'(\mathbf{u}) - R'(\mathbf{v})\|_{L^2} \tag{2.101}$$

$$\leq \frac{\gamma}{1 - \gamma\eta}\beta'\|\mathbf{u} - \mathbf{v}\|_{L^2}, \text{ by lemma 2} \tag{2.102}$$

$$= \beta\|\mathbf{u} - \mathbf{v}\|_{L^2}. \tag{2.103}$$

2.5   Addressing large deformations with bisection method

The objective of the analysis by NFEM is to satisfy the equilibrium equation such as the equation.1.18. In other words, it is to make the vector of the residues disappear. In Newton-Raphson method's, the iteration stops when the value of the residual vector is less than a specific tolerance. In this case, the iteration converges and the solution becomes the current displacement. However, the iterations may not converge in some cases. The Newton-Raphson failed to converge when the starting point is far from the solution. So, the program stops when the iteration counter reaches the maximum number of iterations allowed. In this case, the algorithm stops with an error message. To avoid this case, the bisection method will be used. This method can be repeated until the iteration converges or reaches the maximum allowed number of bisections.

Bisection method

In mathematics, the bisection method is a method of finding roots that divides an interval several times and then selects a sub-interval in which the root must be located for further processing. This method is based on the intermediate value theorem for continuous functions.

As indicated previously, the Newton-Raphson method may find difficulty in converging to the solution [33]. In this case, reducing the amount of the increment by dividing in half each time the convergence iteration fails to converge, then the loop is repeated from the previously converged point. The bisection

process stops once the maximum number of bisections is reached.

By integrating the bisection method into the Newton-Raphson method the new algorithm becomes as follows:

Algorithm 2 Newton-Raphson algorithm with bisection method's

Initialize u^0, k, k_b, *max_iteration*, *tolerance*, *b_tolerance*,*b_iteration*
Calculate Jacobian matrix $\mathscr{K}_{\mathscr{T}}$ eq. (2.10)
Calculate residual (R) eq. (2.12)
Calculate convergence (*conv*) eq. (2.13)
while *conv > tolerance* & $k < max\_iteration$ **do**
    Set $k = k + 1$
    if ($conv \leqslant tolerance$) **then**
        stop.
    end if
    if ($k > max\_iteration$) **then**
        stop, with error message
    end if
    Calculate solution increment Δu
    Update solution by $u = u + \Delta u$
    Calculate convergence (*conv*) eq. (2.13)
    if (convergence $> b\_tolerance$ $||$ $k \geq max\_iteration$) **then**
        if ($k_b < b\_iteration$) **then**
            $k_b = k_b + 1$
            $\Delta u = \Delta u * 0.5$
            Update solution by $u = u + \Delta u$
        else
            stop, with error message
        end if
    end if
    Calculate convergence (*conv*) eq. (2.13)
end while

Example

Taking the same example discussed in the previous section(Sec.2.3). We choose the values of the convergence and stop criterion for the bisection method 0.5 and 4 respectively.

The first test result with $u_0 = [0.2, 0.1]$:

$$Iteration \quad 1: \quad u1 = -0.32500000000000028866, \quad u2 = -0.22500000000000025535$$

$$Iteration \quad 2: \quad u1 = -0.09738160291438990868, \quad u2 = -0.07288251366120226948$$

$$Iteration \quad 3: \quad u1 = -0.01579861914262817302, \quad u2 = -0.01283360262817323516$$

$$Iteration \quad 4: \quad u1 = -0.00060394058117522673, \quad u2 = -0.00052466182254340236$$

$$Iteration \quad 5: \quad u1 = -0.00000099513290709554, \quad u2 = -0.00000090591011892417$$

$$Iteration \quad 6: \quad u1 = -0.00000000000279327560, \quad u2 = -0.00000000000262366005$$

The second test result with $u_0 = [0.85, 0.35]$:

$$
\begin{aligned}
Iteration \quad 1: \quad & u1 = 0.81136363636363639795, \quad u2 = 0.10681818181818181213 \\
Iteration \quad 2: \quad & u1 = 1.12168872806060271330, \quad u2 = -0.06562528280994642249 \\
Iteration \quad 3: \quad & u1 = 1.01624470697865687541, \quad u2 = -0.00857178236204569205 \\
Iteration \quad 4: \quad & u1 = 1.00037706830737005426, \quad u2 = -0.00019555153336901603 \\
Iteration \quad 5: \quad & u1 = 1.00000021293148022572, \quad u2 = -0.00000010910928069496 \\
Iteration \quad 6: \quad & u1 = 1.00000000000006794565, \quad u2 = -0.00000000000003456074
\end{aligned}
$$

Figure 2.11 show that the solution converge at a 5th iteration for the first test. Figure 2.12, show the second test where the solution converge at a 6th with precise convergence.
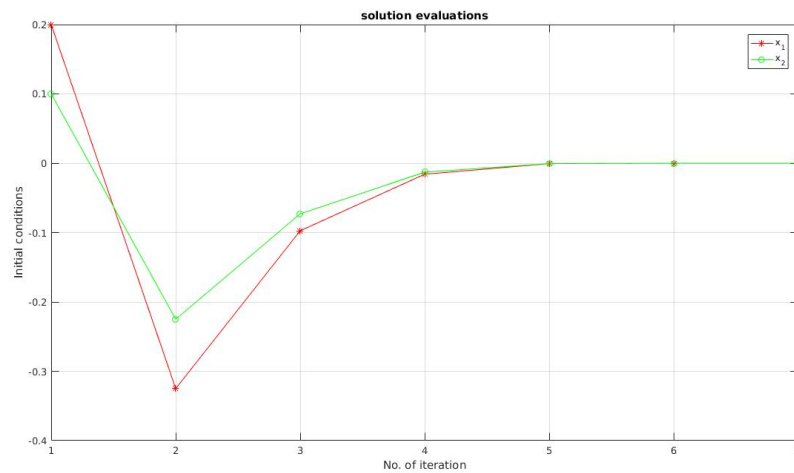
Figure 2.11: Convergence of solutions g(x_1, x_2) with integrating the bisection method. Initial conditions: $x_1(0) = 0.2$ and $x_2(0) = 0.1$
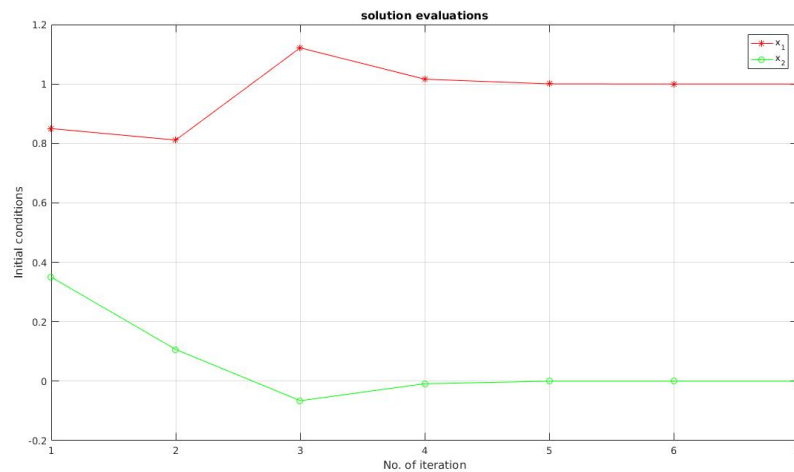
Figure 2.12: Convergence of solutions g(x_1, x_2) with integrating the bisection method. Initial conditions $x_1(0) = 0.85$ and $x_2(0) = 0.35$

2.6 Conclusion

In this chapter, we define the iterative process of Newton-Raphson for solving the nonlinear problem. Sometime this process lose the convergence solution if the initial condition is far from the solution. Therefore, the Kantorovich' theorem is used as sufficient condition for the convergence of Newton-Raphson method. We proposed a new technique for calculate the radius of convergence using Kantorovich's theorem in the discretized domain by the nonlinear finite element method. This technique allows us to calculate the upper bound of the inverse of the Fréchet derivative of residue. With the control parameters we can define the convergence region. These parameters are defined experimentally.

Chapter 3

Modified Newton-Raphson approach with partially updated stiffness matrix

3.1 Introduction

The Newton-Raphson method requires to update the total tangential stiffness matrix of a mesh at each iteration (see section 2.3). This method becomes slow if the mesh has a large number of nodes. Therefore, this problem affects the quality of the convergence speed. As mentioned before, surgical simulators need the computational process to perform the deformation in real time. For that, we proposed two new techniques for the update of the tangential stiffness matrix. We subdivide the global domain of mesh into two sub-domains. The sub-domain in which the strain and the large displacement are located will be treated at each iteration. The other sub-domain is initialized for the first proposed method by null displacement and for the second proposed method by linear elastic material and that only for the first iteration.

3.2 Definition of partially updated stiffness matrix

The resolution of the problem of nonlinear deformation of soft tissue by an iterative process of Newton-Raphson as mentioned has drawbacks on the cost of calculations and the speed if the organ is represented by a large mesh (large number of node and element). In the surgical simulation, the organs of the human body are represented by large mesh so that they are more realistic but that poses problem for simulator based on real time. This problem resides on the computation of the stiffness matrix and its update at each iteration. In surgery, the operation is done on a particular local region such as resection, tumor removal, biopsy, etc. In this case, the displacement will be very small outside the deformation zone [72]. The two contributions in this chapter are based on this observation. The mesh is sub-divided into two sub-domains. A sub-domain whose substiffness matrix will be updated at each iteration. The other sub-domain whose substiffness matrix will be constant during all the iterations. The selection of such a sub-domain is a problem in full share which is discussed in the next section.

3.3 Problem of selection of the updated substiffness matrix

In the medical field, ablations, biopsies and incision are made on a defined part of an organ. The precise selection of this part is a problem in surgical simulation. Let us consider the decomposition of soft tissue as mentioned in figure 3.1. To delineate the frontier of $\Omega^\star$ and determine its size we compare two different approaches.
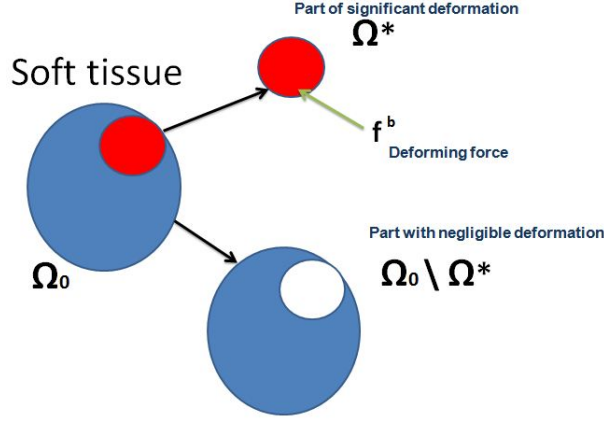
Figure 3.1: Decomposition of soft tissue which the red color represent Ω^* with external force f^b and the blue color represent the remaining part

3.3.1   First approach

This approach is used in the work by Wang et al. [72]. The general idea of Wang et al. method is to reduce the computational matrix by taking a set of elements involved in the computation around the center of the force-carrying element that has been selected to perform an accelerated finite element simulation (see figure 3.2). Given a deforming force applied on an element, the method delimits the boundary of $\Omega^\star$ around this element by the following heuristic screening criterion:

$$|\overrightarrow{o_j o_k}| \leq s\, l, \text{ for } 1 \leq j, k \leq M. \tag{3.1}$$
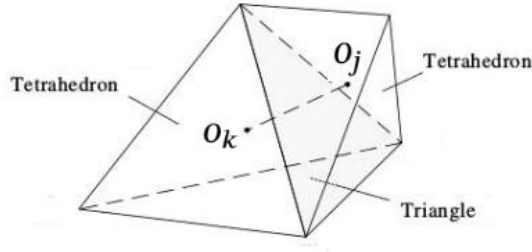
Figure 3.2: Screening the elements involved in the calculation

Where o_j, o_k are the centers of gravity of the two adjacent elements. l is the maximum edge length of the shared face. s is a screening coefficient that tunes the size of $\Omega^\star$ We tested this method on a regular mesh cube which contains 1000 vertices and 4374 tetrahedral elements. The following table 3.1 shows the effect of different screening coefficients. With this method, $\Omega^\star$ does not exceed 11.11% of total mesh and the computing scale of the model did not change when $s > 40$.

Table 3.1: $\Omega^\star$ with different screen coefficient.

s	Number of nodes	Number of elements	% of $\Omega^\star$
1	8	5	0.11
2	10	8	0.18
3	12	11	0.25
5	19	23	0.52
10	38	63	1.44
15	64	122	2.79
20	79	201	4.59
35	187	445	10.7
40	198	480	10.9
41	200	486	11.11
45	200	486	11.11
60	200	486	11.11

3.3.2   Second approach

$\Omega^\star$ is obtained by partitioning the main domain Ω_0 by different scales sizes around the deformation region. In the experimental section, we used percentages among at 10%, 20%, 30%, 40% and 50%. Figure 3.3 show some percentages of $\Omega^\star$ of mesh A which is contain 1000 vertex and 4374 tetrahedron. This approach allows for a wider choice of size range for $\Omega^\star$. The optimal choice of $\Omega^\star$ requires precise formal and optimal criteria to determine the zone of deformation.
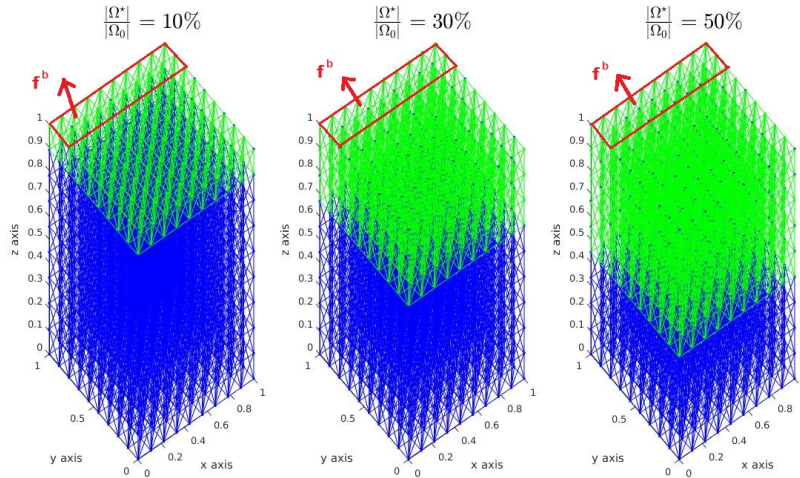
Figure 3.3: Mesh A with different $\frac{|\Omega^\star|}{|\Omega_0|}$

3.3.3   An open problem: Selection of the boundary of the substiffness matrix

Based on the two approaches discussed previously. The selection part of an organ is a very important task for a realistic simulation. The first approach has a disadvantage on the resection of a mesh. For certain mesh the screening coefficient does not take more than 10% of the latter to process it. As indicated in the example of section 3.3.1 for a regular mesh cube the $\Omega^\star$ does not exceed 11.11% of the total mesh. The second approach resection the mesh by different percentage around the deformed part. In the surgical simulation this ratio is not enough as will be demonstrated later in the experimental results section. Taking the case of the liver, it is difficult to practice a resection at localized part (eg a tumor) without

taking into account the relationship with the adjacent portal, venous and biliary intrahepatic structures. Therefore, an optimal boundary selection is an important problem to solve in our context. That will be our perspective in our future work. In this thesis, we consider a set of sub-optimal selected regions on which we show the effectiveness of our approaches.

3.4 Contribution 2: Substiffness matrix initialized with initial value

Our main formal contribution in this thesis is to update at each iteration only the tangential stiffness matrix of the region concerned by the deformation. The remaining of the tangential stiffness matrix will be initialized only once at the starting of the iterative process. Thus, we can divide the domain of the deformed organ into two subdomains $\Omega^\star$ with $N^\star$ vertices and $\Omega_0\backslash\Omega^\star$ with $(N - N^\star)$ vertices (see figure 3.4). Where $\Omega^\star$ is the subdomain where the strain is located and the displacement is important. We note this method as $Init\_0$. This subdivision allows us to decrease the computational complexity of each tangential stiffness update from $\mathcal{O}(N)$ to $\mathcal{O}(N^\star)$. So, in the step 6 of the generic iterative algorithm (section 2.4.3) the equation eq 2.42 is simplified as follows

$$\mathscr{K}_T(\overline{\overline{U}}_h) = \sum_{\omega^e \in \Omega^\star} \mathscr{K}_{\omega^e}(\overline{\overline{U}}_h^e). \tag{3.2}$$
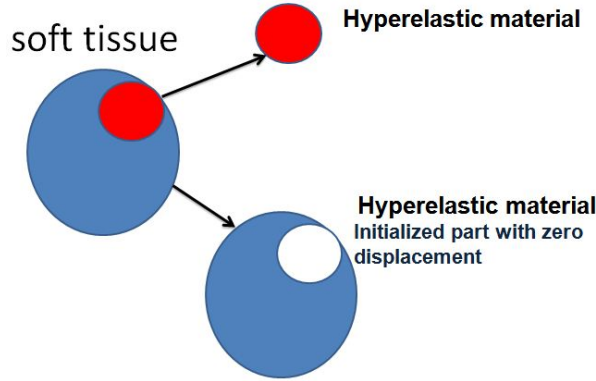
Figure 3.4: Decomposition domain into two sub-domain. Red color: Assembled part at each iteration. Blue color: Remaining part with initial value.

3.5 Contribution 3: Substiffness matrix initialized with linear deformation

For the same idea discussed previously in section 3.4 on the division of the global domain into two subdomains. We will now consider $\Omega_0\backslash\Omega^*$ as a linear elastic part initialized only once on the first iteration and Ω^* as a nonlinear hyperelastic part which will be treated at each iteration (see figure 3.5).We use for Ω^* Mooney-Rivlin model and for $\Omega_0\backslash\Omega^*$ a linear mechanical characteristics. We denote this method as $Init\_L$.
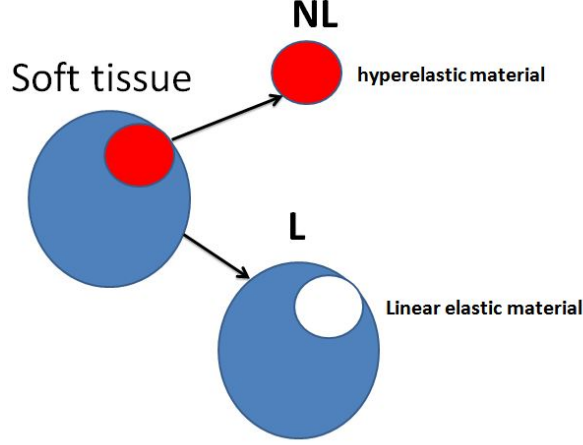
Figure 3.5: Decomposition domain into two sub-domain. Red color: $\Omega^\star$ with nonlinear hyperelastic material. Blue color: Remaining part with linear elastic material

3.6 The proposed algorithm with partially updated stiffness matrix

Our objective is to minimize the cost of calculating the stiffness matrix in the iterative process. For that, we propose the division of domain Ω_0 by two sub-domains ($\Omega^\star$ and $\Omega_0 \backslash \Omega^\star$) where the deformed part is the one that will be treated. Our algorithm is as follows (see figure 3.6). In the first step, we load the mesh of organ, and the necessary data such as the fixed part, the deformed part and the vertex to be moved (bloc A). We select one of the two proposed methods ($Init\_0$ and $Init\_L$). For the first proposed method ($Init\_0$) we initialize the global stiffness matrix $\mathscr{K}_T$ with a zero displacement $U = 0$ (bloc B). Then, for the second proposed method ($Init\_L$) we initialize the global stiffness matrix $\mathscr{K}_T$ with linear elastic material (bloc C). The next step (bloc D), is to assemble the partial stiffness matrix with the current displacement U and update the residual vector for all mesh. We update the boundary condition with fixed vertex (bloc E). The partial assembly will be repeated until the solution converges. The last step (bloc F and bloc G), is to compute the constants of the two propositions (2.1, 2.2) and check if the constraint ($\alpha\beta \leq \frac{1}{2}$) is justified than compute radius of convergence (bloc H) with proposition 2.1.
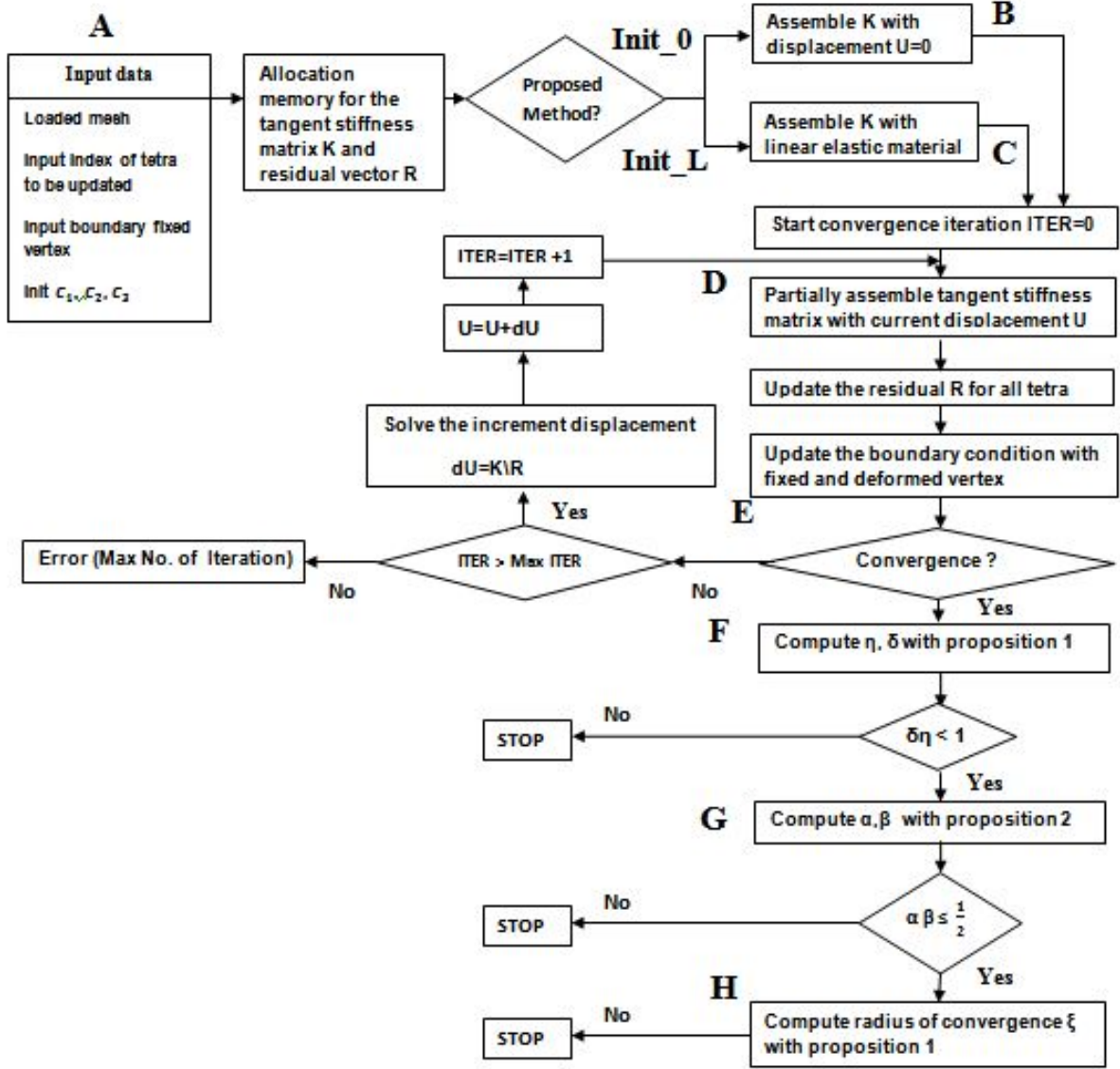
Figure 3.6: Diagram of Our method

3.7 Simulation Results with Mooney-Rivlin constitutive model

3.7.1 Results of substiffness matrix initialized with initial value

We compared the proposed method to two state-of-the-art approaches: *(i)* the classic Newton-Raphson algorithm [33] and *(ii)* the method proposed by Wang et al. [72]. To evaluate the results of our method and show its efficiency, we take into consideration three parameters: *(1)*The precision of reconstructing the deformation. *(2)* The convergence time. *(3)* The radius of convergence. The classical Newton-Raphson method updates the total tangential stiffness matrix at every iteration. Therefore, we used it as a standard method for measuring precision. We calculated the precision for the complete domain Ω_0

and the two sub-domains ($\Omega^\star$ And $\Omega_0\backslash\Omega^\star$) according to the following formulas

$$\epsilon_{\mathbf{\Omega}}^{method_i} = \frac{1}{N} \left\| \left[\sum_{e\in\mathbf{\Omega}} \overline{U}_h^{\,e} \right]_{\text{classic method}} - \left[\sum_{e\in\mathbf{\Omega}} \overline{U}_h^{\,e} \right]_{method_i} \right\|_2 . \tag{3.3}$$

Where $\mathbf{\Omega}$ is alternatively Ω_0, $\Omega^\star$ and $\Omega_0\backslash\Omega^\star$ and $method_i$ is either the proposed or Wang et al. [72]. The convergence time is the time required to find a final approximate solution by each method. It can be considered as the speed of convergence of a simulation. All the methods are initialized with zero displacement vector. From the formulas of propositions 2.1 and 2.2, we can calculate the radius of convergence for each method. In this section, we performed tests for the three methods (classic Newton-Raphson, proposed method and Wang et al method) by choosing the constitutive nonlinear Mooney-Rivlin model [33]. Since, this thesis concerns surgical simulation for that we used the mechanical properties of the liver that we have found in the literature [28, 18]. The constants of the material are taken as $C_{10} = 0.16 KPa$ and $C_{01} = 0.14 KPa$ while the mass modulus (or the Bulk modulus) is fixed at $K = 11.11 KPa$ [28]. For the rest of this experimental part, we performed two series of experiments: The first series carried tests on a regular cubic mesh and the second on a non-regular mesh of a soft tissue of the liver. In the first set, we used a different number of node and element. We used the tetrahedron as a representative type of mesh in this experiment.

Simulations on a regular meshed cube

We ran a first set of experiments. The cube has length, width and height of 10 mm. We ran experiments on three different meshing resolutions as shown in table 3.2.

Table 3.2: Different resolutions of the meshed cube.

Mesh	Type	Elements	Vertices
A	tetrahedron	4347	1000
B	tetrahedron	3375	16464
C	tetrahedron	8000	41154

As mentioned in our contribution, we splitting the domain Ω_0 into two sub-domains ($\Omega^\star$ and $\Omega_0\backslash\Omega^\star$). $\Omega^\star$ contains the nonlinearly deformed vertices. For a precise comparison between our method and Wang et al. method we use the same mesh subparts for both algorithms. For each regular mesh, we imposed a non-zero border displacement on 5% of the vertices at 3 mm on the x,y and z axes (ie deformation of vertices by 30%). We varied the nonlinearly $\Omega^\star$ in a range of 5 sized subparts with $\frac{N^\star}{N} \times 100 = 10\%$, 20%, 30%, 40% and 50% of the overall mesh domain Ω_0. By the following, we label these percentages as $\frac{|\Omega^\star|}{|\Omega_0|}$. We fixed about 10% of the overall mesh. We ran our experiments with the same code for the three compared methods on core i3 lap-top with 4Go RAM and Matlab2016a.

Precision of reconstructing deformations

Figures 3.7 and 3.8 illustrate some qualitative results of deformations. The two figures show the deformation of mesh A by the three methods. They represent the deformation of 10% and 50% of $\Omega^\star$ respectively. We see that our method has the same form of physical deformation and precision as Newton-Raphson. For the two deformation tested by Wang et al. method [72](shown in the figures cited above) we see that the deformation lacks physical reality and the deformation of $\frac{|\Omega^\star|}{|\Omega_0|} = 50\%$ is better than $\frac{|\Omega^\star|}{|\Omega_0|} = 10\%$. Figures 3.9 and 3.10 show the precision of deformation of our and Wang et al. methods. These quantitative results confirm our observation on the precision of our method. Where, the subdivision of domain Ω_0

does not affect negatively on the deformation amount. Consequently, the partial update of the tangential stiffness matrix is the good choice compared to the update of the total tangential stiffness matrix.

Time of convergence

The execution times of the three algorithms are summarized in figure 3.11. This figure shows the convergence times of each mesh (A, B, C) with the five different $\frac{|\Omega^{\star}|}{|\Omega_0|}$. We use the logarithm with the base 10 to display the axis of execution times. We note that our method converges more quickly to the solution and that is thanks to the fast computation of the partially tangential stiffness matrix. Our remark on the convergence time of the Wang et al. method that this is not enough precise in the computation of the tangential stiffness matrix by comparing with the proposed method. In this case, the process produces more iteration in order that the solution converges. In addition, to fix too many vertex physically is not realistic because when we moves a set of vertex in a nonlinear way, inevitably its neighbors react and follow this movement.

Radius of convergence

To apply Kantorovich's theorem for the three compared methods. We must first calculate the norms of the different terms which are used in propositions2.1 and2.2 to calculate the radius of convergence see Table 3.3. Where, the control constants $\mathbf{c}_1$, $\mathbf{c}_2$ and $\mathbf{c}_3$ are chosen experimentally to satisfy the two conditions (i.e. $\gamma\eta < 1$ and $\alpha\beta \leq \frac{1}{2}$), To calculate β from equation 2.87, we get the maximum over $\mathbb{B}(\bar{u}_h, 2\alpha)$ by simply solving a linear problem by linearizing $\mathscr{D}_h$ and F_h around the approximate solution $\overline{U}_h$. In our experience for the three meshes A, B, C with part of $\frac{|\Omega^{\star}|}{|\Omega_0|} = 10\%$, we chose a range of values for the two constants of assumptions 1 and 2 . Where, We varied $\mathbf{c}_1$ from 10^{-1} to 50 with 200 steps and $\mathbf{c}_2$ is varied from 10^{-5} to 10^{-4}. For assumption 3 we fixed the control constant at $\mathbf{c}_3 = 1.5$. The figures 3.12, 3.14 and 3.16, show the values of the products $\gamma\eta$ and $\alpha\beta$. We use the logarithm with the base 10 to display these values. We can see that the three constants chosen satisfy the conditions of proposition 2.2.
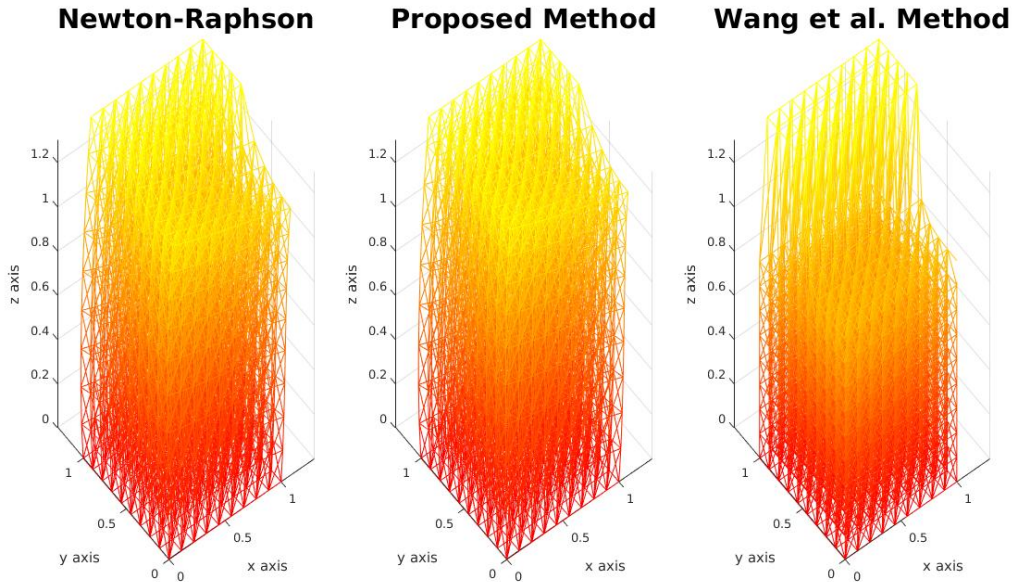

Figure 3.7: Result of deforming mesh A with $\frac{|\Omega^{\star}|}{|\Omega_0|} = 10\%$.
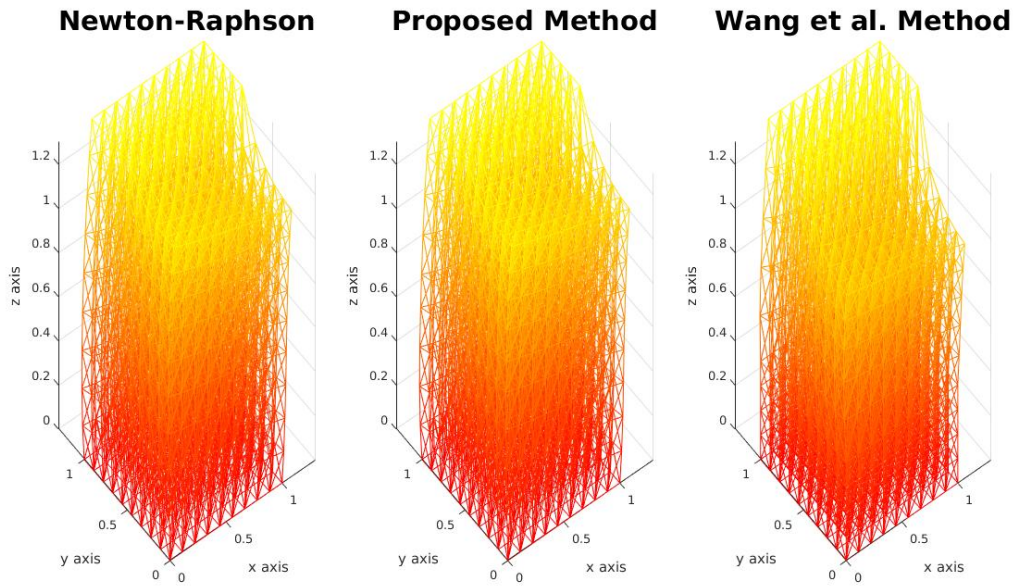
Figure 3.8: Result of deforming mesh A with $\frac{|\Omega^\star|}{|\Omega_0|} = 50\%$.
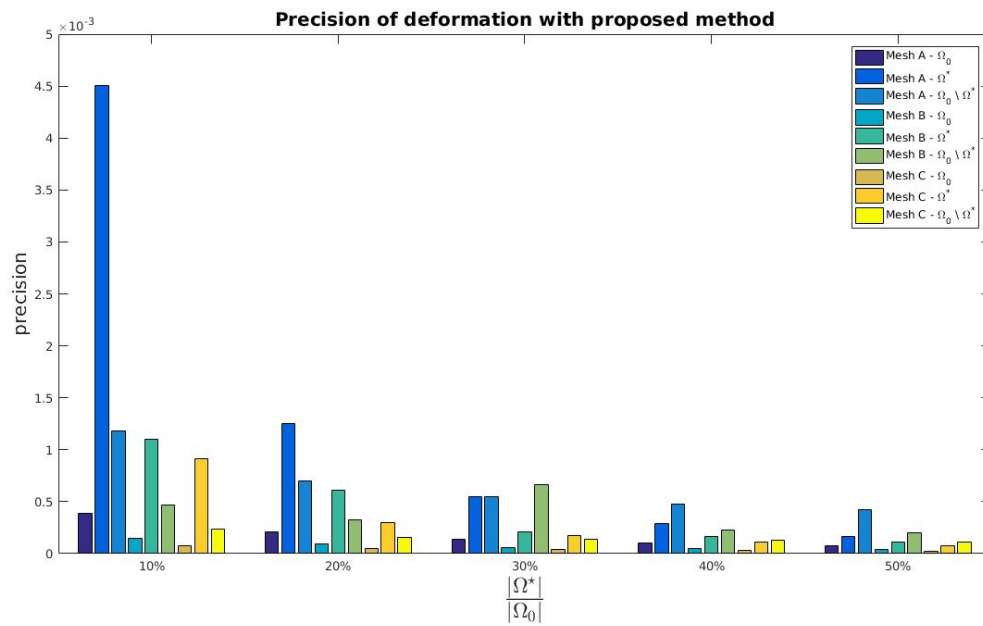

Figure 3.9: Precision of reconstructing deformations with proposed method.
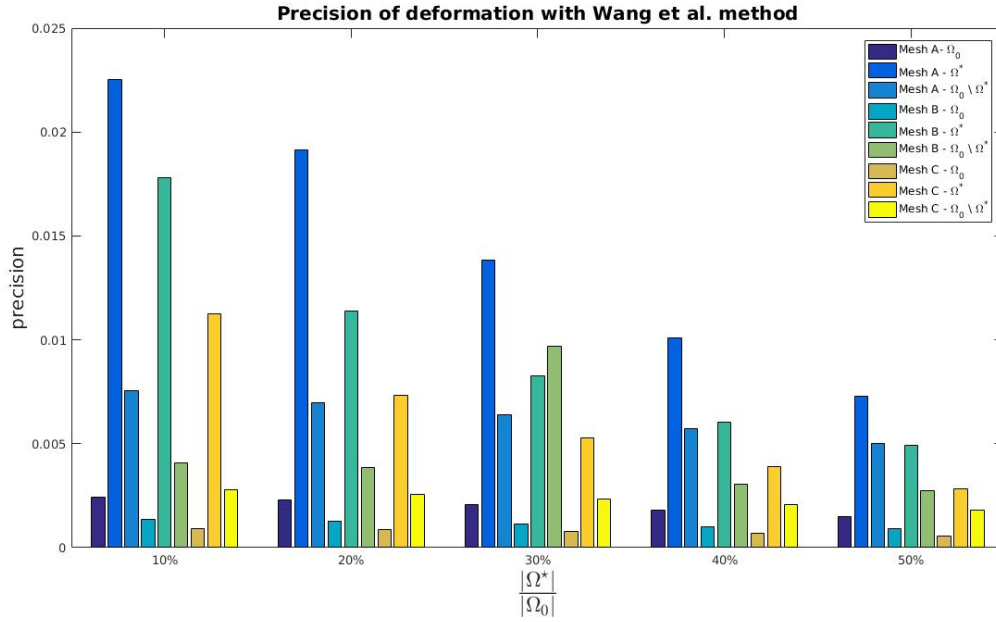
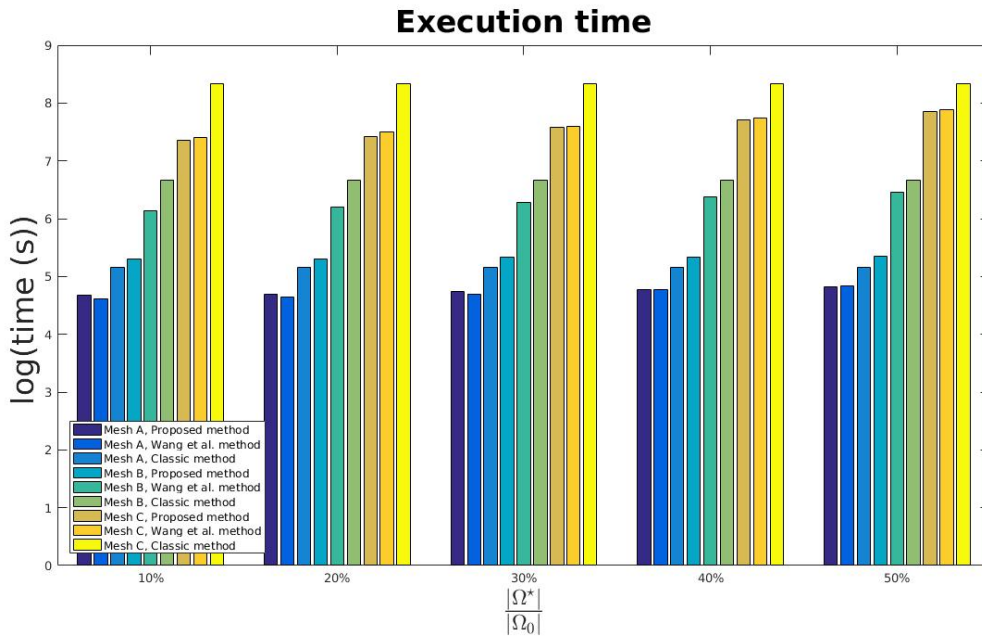Figure 3.10: Precision of reconstructing deformations with Wang et al. method.

Figure 3.11: Execution time of all methods for the three meshes A, B and C.

Figure 3.13, 3.15 and 3.17 show the radius of convergence for all methods. We can say that for certain values of c_1 and c_2, the proposed method has a radius of convergence similar to the classic method. As well, these two methods are better than Wang et al. method. The table 3.4 presents some examples of values of the radius of convergence.

Table 3.3: Estimation of upper bounds for regular meshes with $\frac{|\Omega^\star|}{|\Omega_0|} = 10\%$.

Mesh	Estimation	Proposed method	Wang et al. method	Newton-Raphson method
A	$\|\nabla_0 \bar{u}_h\|_{L^2}$	185.4339	372.3015	178.4332
	$\|\{F_h(\bar{u}_h)\}\|_{L^2}$	599.0464	699.8396	597.7208
	$\|\{\mathscr{S}_h(\bar{u}_h)\}\|_{L^2}$	0.0623	0.3508	0.0682
	$\|\{\mathscr{D}_h(\bar{u}_h)\}\|_{L^2}$	4.1126	37.7582	3.0644
	$\|\mathscr{K}_T(\overline{U}_h)\|_F$	0.5758	0.4724	0.6504
	$\|\mathscr{K}_T(\overline{U}_h)^{-1}\|_F$	2.4819e+05	2.8430e+04	2.8641e+05
B	$\|\nabla_0 \bar{u}_h\|_{L^2}$	349.2160	700.1930	341.9864
	$\|\{F_h(\bar{u}_h)\}\|_{L^2}$	1.1578e+03	1.3425e+03	1.1569e+03
	$\|\{\mathscr{S}_h(\bar{u}_h)\}\|_{L^2}$	0.1111	0.6016	0.1138
	$\|\{\mathscr{D}_h(\bar{u}_h)\}\|_{L^2}$	12.0565	71.9946	5.9133
	$\|\mathscr{K}_T(\overline{U}_h)\|_F$	0.8033	1.8754	0.8339
	$\|\mathscr{K}_T(\overline{U}_h)^{-1}\|_F$	6.4532e+05	2.8430e+04	8.4301e+05
C	$\|\nabla_0 \bar{u}_h\|_{L^2}$	559.9283	1.4811e+03	550.0074
	$\|\{F_h(\bar{u}_h)\}\|_{L^2}$	1.8328e+03	2.3299e+03	1.8317e+03
	$\|\{\mathscr{S}_h(\bar{u}_h)\}\|_{L^2}$	0.1601	14.1466	0.1652
	$\|\{\mathscr{D}_h(\bar{u}_h)\}\|_{L^2}$	21.2159	2.6341e+03	9.4253
	$\|\mathscr{K}_T(\overline{U}_h)\|_F$	0.9077	2.2754	0.9884
	$\|\mathscr{K}_T(\overline{U}_h)^{-1}\|_F$	1.4451e+06	9.5613e+05	1.8673e+06
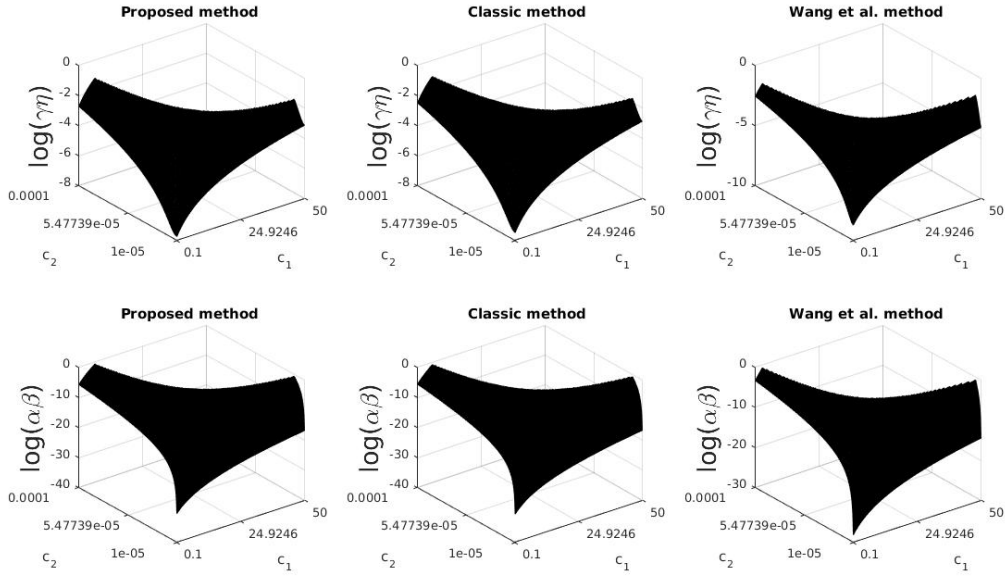
Figure 3.12: Conditions of the two propositions for mesh A with $\frac{|\Omega^\star|}{|\Omega_0|} = 10\%$.
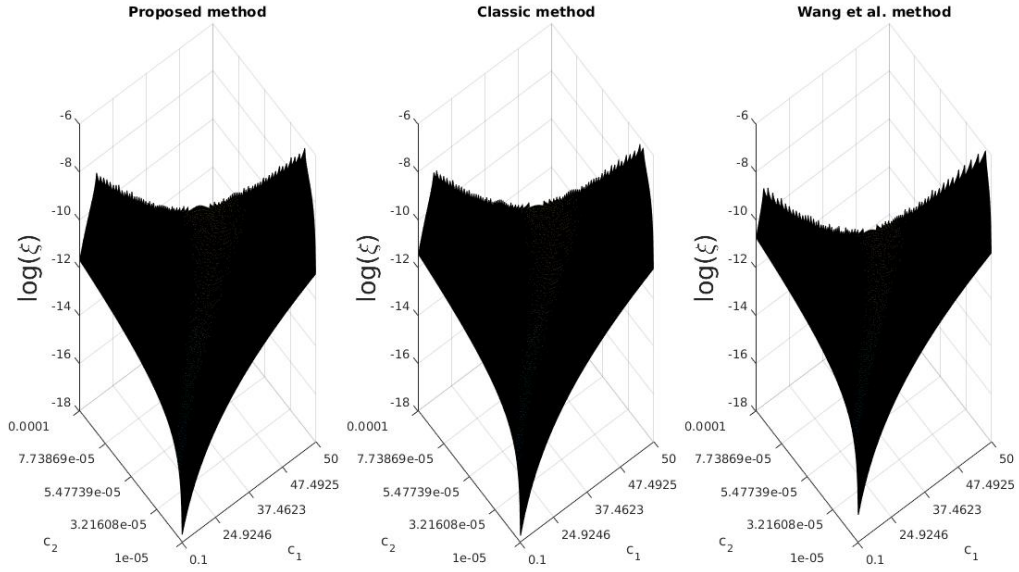
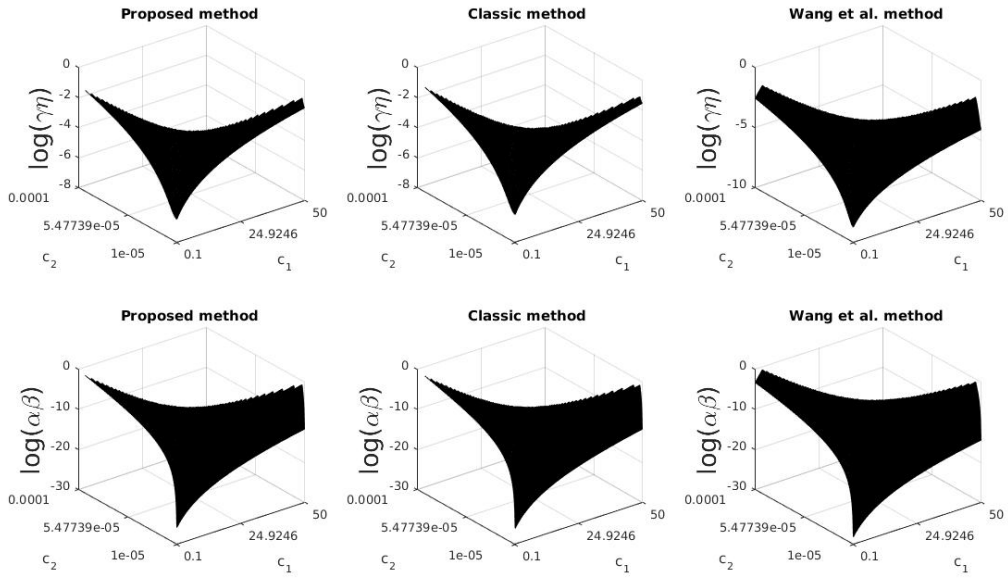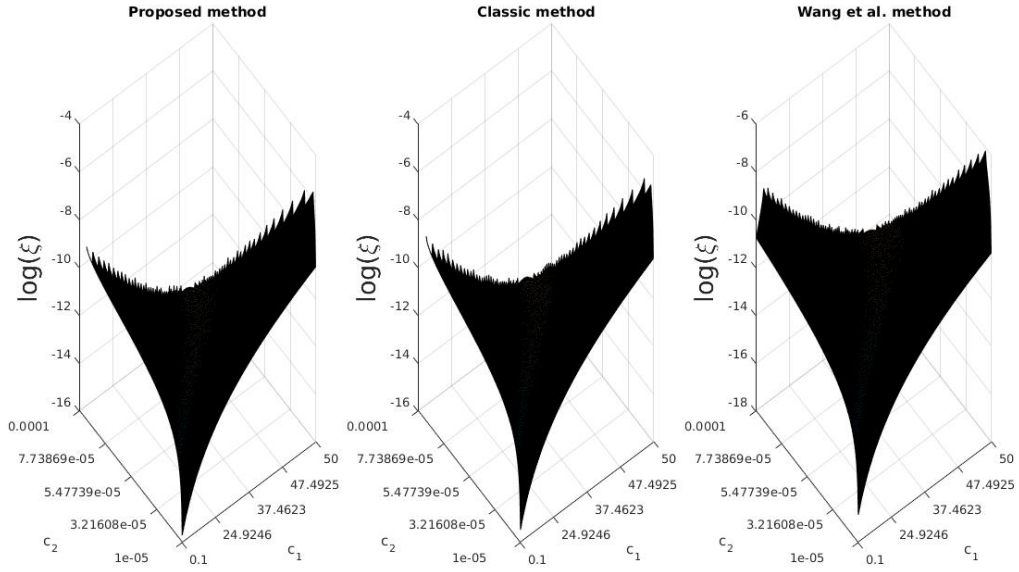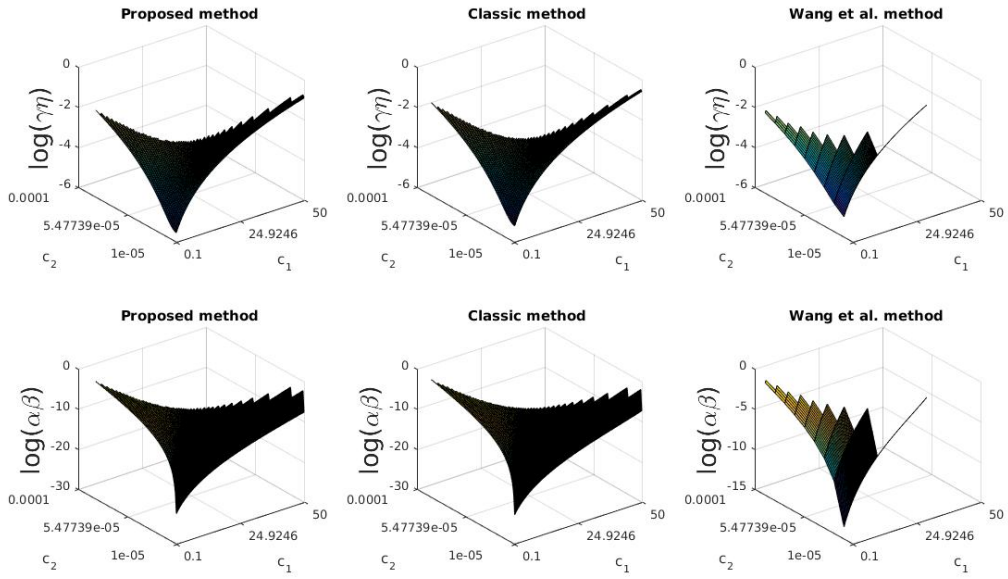Figure 3.13: Radius of convergence of regular mesh A with $\frac{|\Omega^\star|}{|\Omega_0|} = 10\%$.

Figure 3.14: Conditions of the two propositions of regular mesh B with $\frac{|\Omega^\star|}{|\Omega_0|} = 10\%$.

Figure 3.15: Radius of convergence of regular mesh B with $\frac{|\Omega^\star|}{|\Omega_0|} = 10\%$.

Figure 3.16: Conditions of the two propositions of mesh C with $\frac{|\Omega^\star|}{|\Omega_0|} = 10\%$.
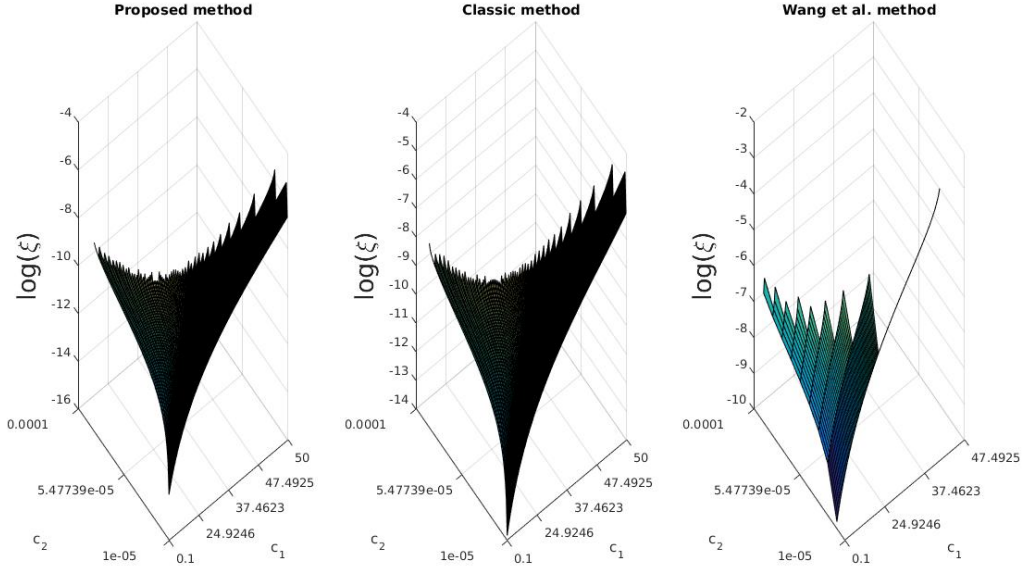
Figure 3.17: Radius of convergence of regular mesh C with $\frac{|\Omega^\star|}{|\Omega_0|} = 10\%$.

Table 3.4: Sample points of radius of convergence.

mesh	c_1	c_2	Proposed method	Wang et al. method	Newton-Raphson method
A	0.1	1e-4	1.6425e-05	3.9223e-05	2.0345e-05
	2.1162	4e-05	2.0868e-05	5.1586e-05	2.6294e-05
	50	1e-5	8.1460e-06	2.0756e-05	1.0461e-05
B	0.1	1e-4	1.6276e-04	3.9223e-05	2.3136e-04
	2.1162	4e-05	1.9297e-04	5.1586e-05	2.6030e-04
	40.2206	1e-5	7.8745e-05	1.6065e-05	1.1421e-04
C	0.1	4e-5	4.7857e-05	0.0038	6.5228e-05
	2.1162	1e-05	1.4850e-05	0.0017	1.9809e-05
	20.1603	1e-5	2.4723e-04	$\gamma\eta > 1$	3.1679e-04

Simulation results on a non-regular liver mesh

For a non-regular mesh, we chose mesh of liver which contains 16291 vertex and 60233 tetrahedra. As mentioned above in the figure 3.1. We fixed the part that exists in the right lobe of the liver, more precisely the lower posterior segment. This part contains approximately 2070 vertex with zero displacement. The superior medial segment considered as deformed part with the non-zero displacement. The selected deformed part contains 825 vertex. We imposed a displacement of 22 mm on the z axis with four different deformed parts $\frac{|\Omega^\star|}{|\Omega_0|} = 20\%$, 30%, 40%, 50%. We ran our experiments with the same code for the three compared methods on core i7 lap-top with 32Go RAM and Matlab2016a.

Figures 3.18 and 3.19 show the precision of the deformations of our method and Wang et al. method compared to the classic method. Our method has a better capture of the nonlinear deformation than the second method of each deformed part $\frac{|\Omega^\star|}{|\Omega_0|}$. Table 3.5 summarizes the execution time of each method with different deformed part. We can say that the proposed method is almost 15 times faster than the classic method. On average, it is also three times faster than Wang et al. method. Figure 3.22 shows

qualitative deformations of the liver that confirms the observation made on the quantitative evaluation of the precision.
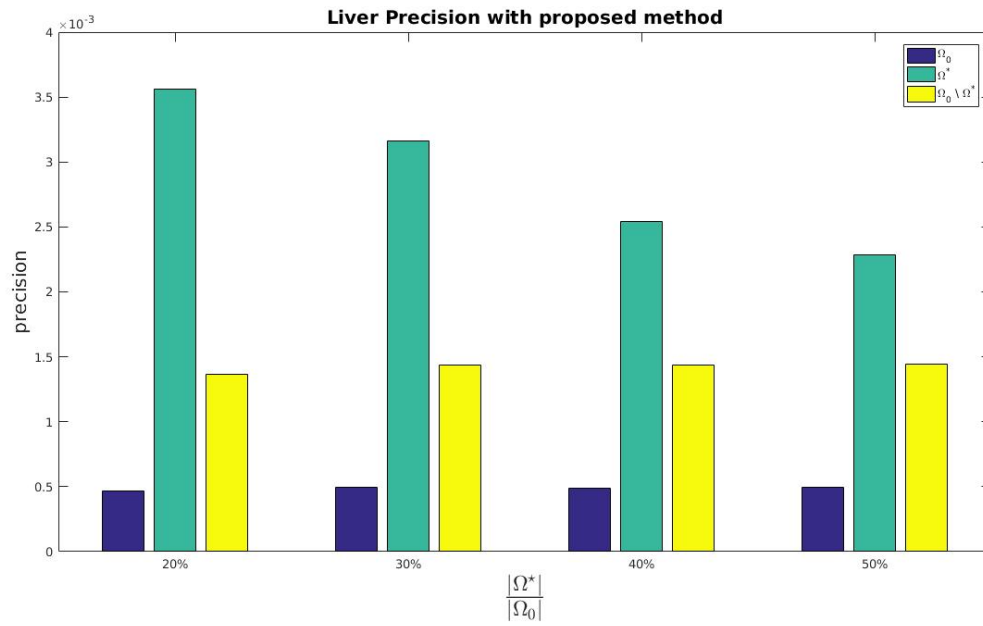

Figure 3.18: Precision of reconstructing liver's deformation with the proposed method.
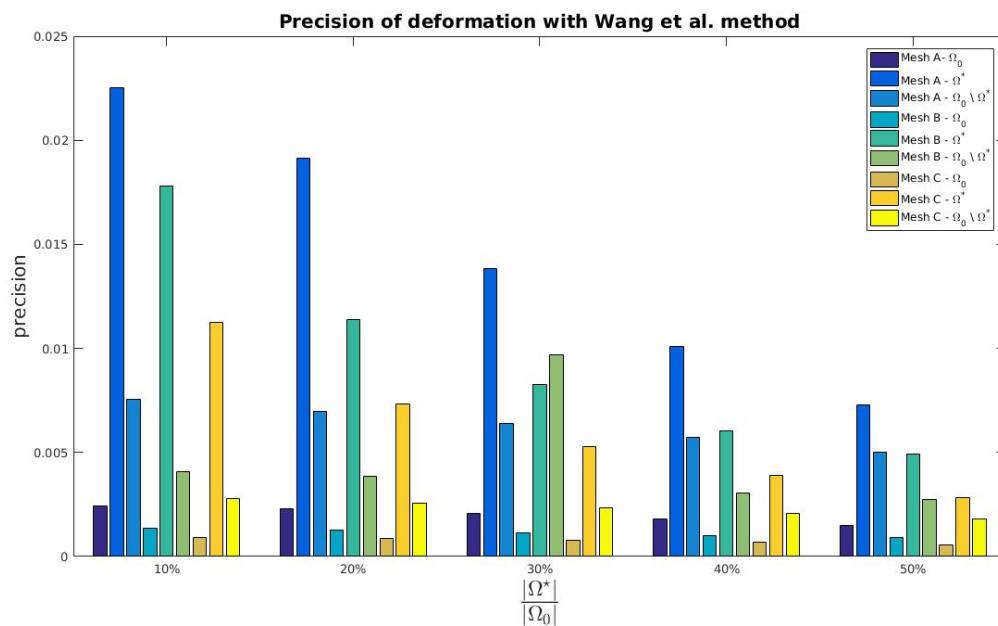

Figure 3.19: Precision of reconstructing liver's deformation with Wang et al. method

Table 3.5: Execution time of liver deformation in seconds.

$\frac{|\Omega^{\star}|}{|\Omega_o|}$	Proposed method	Wang et al. method	Newton-Raphson method
20%	6.0720e+03	1.2777e+04	8.7975e+04
30%	7.6998e+03	1.2249e+04	8.7975e+04
40%	1.2625e+04	1.8682e+04	8.7975e+04
50%	6.7999e+03	1.3906e+04	8.7975e+04

For this experiment, the convergence of solution is justified by Kantorovich's theorem. We experimentally defined the control parameters to calculate the convergence radius. We chose a range of values for the constants $\mathbf{c}_1$ and $\mathbf{c}_2$. Where,$\mathbf{c}_1$ is varied from 10^{-2} to 50 and $\mathbf{c}_2$ from 10^{-7} to 10^{-6} with step of 100 for both. The third constants of assumption 3 is fixed at $\mathbf{c}_3 = 2$. In table 3.6 we show the norms of the terms used in propositions 2.1 and 2.2 of the deformation of liver with $\frac{|\Omega^{\star}|}{|\Omega_o|} = 20\%$ with each method compared.

β is calculated as explained in the previous subsection 3.7.1. The product of the conditions $\gamma\eta$ and $\alpha\beta$ of the two propositions 2.1 and 2.2 are configured in figure 3.20. With certain values obtained we can justify the convergence of the solution by application of Kantorovich's theorem.

Figure 3.21 shows the radius of convergence obtained for each method. From this figure we can classify the three methods compared according to the minimum and maximum values of convergence radius in this order: the classical method, the proposed method and Wang et al. method. Table 3.7 shows some points of the convergence radius for the compared methods.

Table 3.6: Estimation of upper bounds for the liver mesh with $\frac{|\Omega^{\star}|}{|\Omega_o|} = 20\%$.

Estimation	Proposed method	Wang et al. method	Newton-Raphson method
$\|\nabla_0 \bar{u}_h\|_{L^2}$	6.2710e+04	1.1726e+05	8.2882e+04
$\|\{F_h(\bar{u}_h)\}\|_{L^2}$	2.9893e+06	3.0013e+06	2.9906e+06
$\|\{\mathscr{S}_h(\bar{u}_h)\}\|_{L^2}$	0.0205	0.1197	0.0247
$\|\{\mathscr{D}_h(\bar{u}_h)\}\|_{L^2}$	8.1916	8.2988	8.2122
$\|\mathscr{K}_T(\overline{U}_h)\|_F$	141.7217	2.0391e+07	107.3756
$\|\mathscr{K}_T(\overline{U}_h)^{-1}\|_F$	8.4770e+05	1.3224e+06	8.4671e+05

Figure 3.20: The conditions $\gamma\eta < 1$ and $\alpha\beta \leq \frac{1}{2}$ for liver mesh
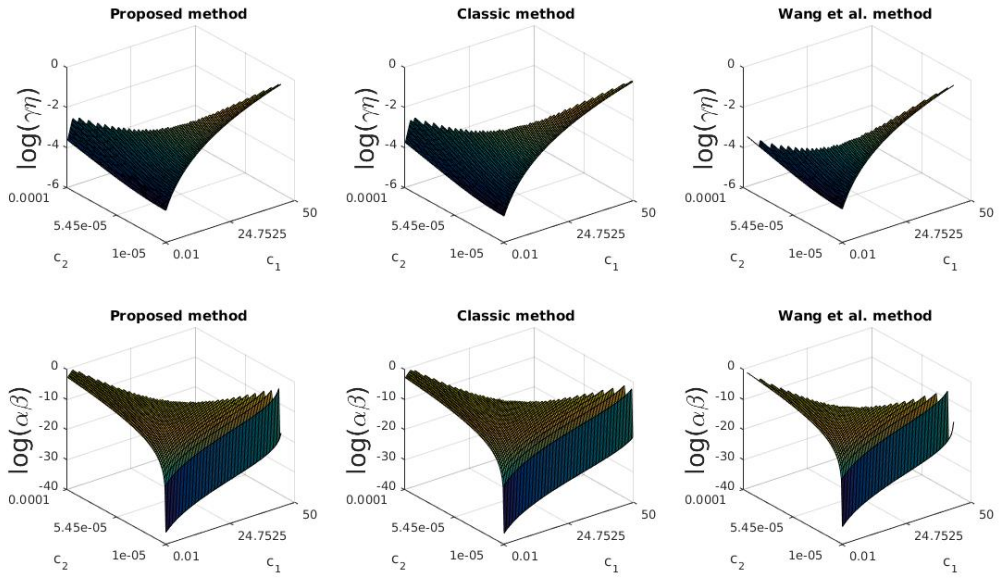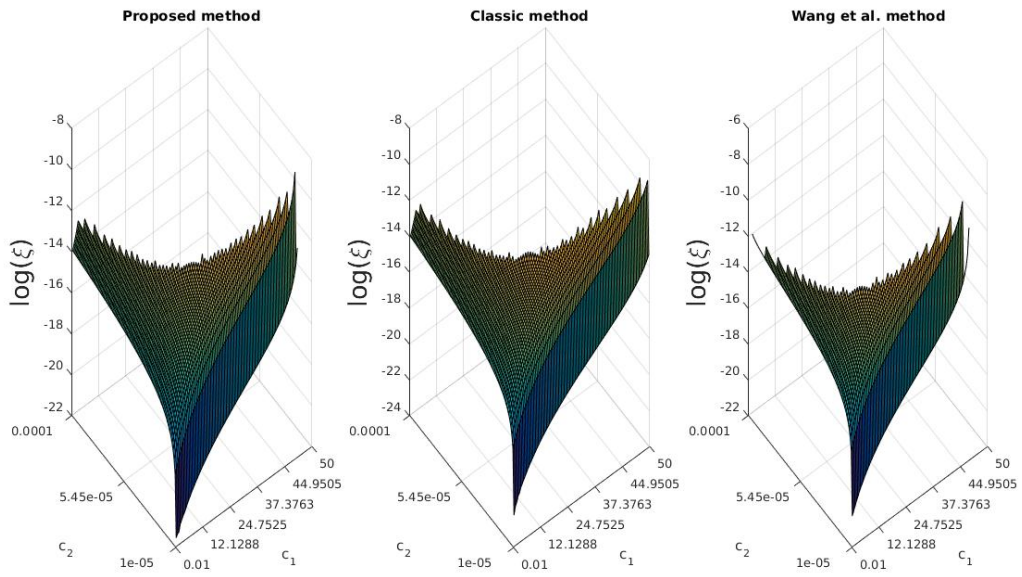

Figure 3.21: The radius of convergence of liver mesh

Table 3.7: Sample points of radius of convergence (liver deformation).

c_1	c_2	Proposed method (s)	Wang et al. method (s)	Newton-Raphson method (s)
0.01	7e-07	1.4663e-07	9.2870e-07	9.8126e-08
1.5248	5e-07	4.2579e-06	2.7512e-05	3.6490e-06
5.0595	1e-07	7.9535e-08	4.9060e-07	7.5043e-08
8.5941	1e-07	1.3502e-07	8.3359e-07	1.2744e-07
50	1e-07	8.1935e-07	$\gamma\eta > 1$	7.7224e-07
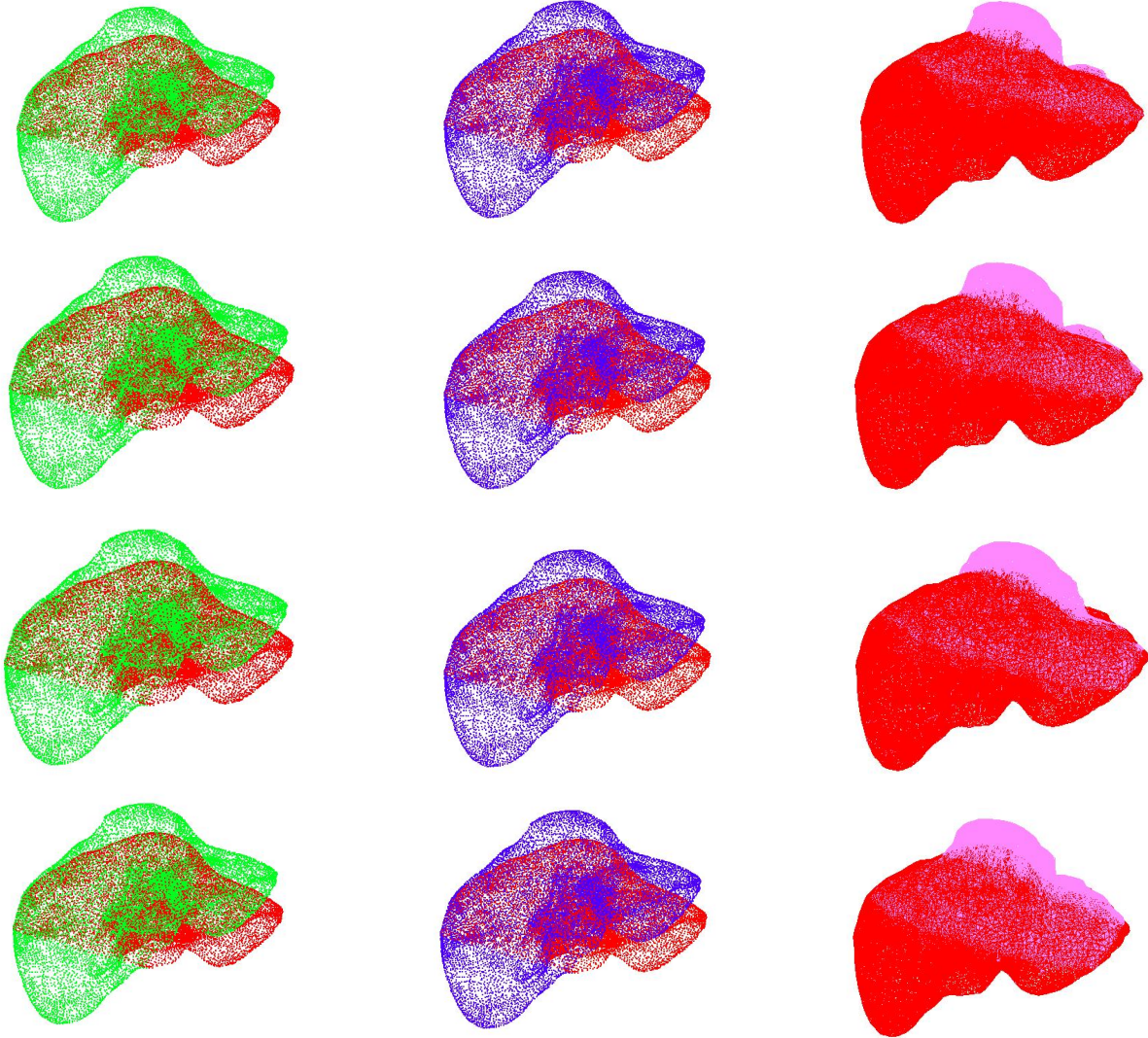
Figure 3.22: Liver deformation for different $\Omega^\star$. From top to down, the rows represent respectively 20%, 30%, 40% and 50% of Ω_0. Red liver represents the initial state at rest. Blue liver is the deformation obtained with the classic Newton-Raphson method. Pink liver represents the Wang's method deformation. Green represents the deformation obtained with the proposed method.

Discussions and comments

In this section, we tested the proposed method by comparing their results with those of Newton-Raphson and Wang et al. methods. The last method optimized the matrix computation by introducing of a

filtering coefficient. In a large mesh, this coefficient will indicate the part which will be deformed and this part which will be treated subsequently. The remaining of the mesh considered as fixed. We tested their method as explained in the section 3.2 and we concluded that this method lacks realism. A comparison was made between the three methods on regular and non-regular meshes represented by FEM. In order, for the comparison to be correct, we take the same $\Omega^\star$ parts and the same fixed part of the meshes for all the methods. From the execution times shown in figure 3.11. We can classify according to the speed of convergence our method in the first place after that Wang et al. method and in the last place Newton-Raphson method. The average difference in execution time between the three compared methods depends on the mesh size. Where, the difference between our method and the classic method for meshes A, B, C are 59.3903 s, 582.587 s and 2148 s respectively. And between our method and Wang et al. method for the same meshes A, B and C are 20.9011 s, 336.1185 s and 268.466 s respectively. In terms of precision, the classic Newton-Raphson method based on FEM is known for its supreme precision for non-linear deformation. Which is our advantage in the contribution proven in this thesis. Where, the proposed method converges to the solution similar to the classic method with runtime optimization. On the other hand, Wang et al. method is less precise and lacks realism. The proposed method has succeeded in improving the speed of convergence of nonlinear deformation without losing precision. Likewise, in the application of Kantorovich's theorem our method has better performances than that of Wang et al. method in the calculation of the convergence radius with favorable sufficient conditions (appropriate choice of $\mathbf{c}_1, \mathbf{c}_2$ and $\mathbf{c}_3$). In this study, we noticed that the norm of the inverse $\|\mathscr{K}_T(\overline{U}_h)^{-1}\|_F$ has high values as show in tables 3.3 and 3.6 . Those are due to a bad conditioning of the matrix of rigidity inherent in the methods of the finite elements. Good conditioning of the stiffness matrix can improve the range of sufficient conditions for the control parameters $\mathbf{c}_1, \mathbf{c}_2$ and $\mathbf{c}_3$ and also the convergence of the solution with less iteration based on the Newton-Raphson method. This problem must be taken into account to further improve the acceleration and speed of convergence.

3.7.2 Results of substiffness matrix initialized with linear deformation

Hence, we performed tests with the proposed method and Newton-Raphson method. Let us consider different parts $\frac{|\Omega^\star|}{|\Omega_0|}$ of 10%-30% and 50%. For regular meshed cube, we impose a displacement on 5% of the vertex of the global mesh which are located in Ω^* of 3 mm on x y and z axis. For the boundary conditions, we fixed about 10% of the global vertex. These are located in the linear part $(\Omega_0\backslash\Omega^*)$. We ran this experiments on core i3 lap-top with 4Go RAM and Matlab2016a. For non regular Liver mesh, we take the same fixed part and $\Omega^\star$ part with 825 vertex as the previous experiment in section 3.7.1. We impose a displacement of 6 mm on the z axis. We ran this experiments on core i7 lap-top with 32Go RAM and Matlab2016a. In the following, for the mechanical properties we used the values that we found in the literature as is mentioned in the table 3.8:

Table 3.8: Properties of liver tissue

Mooney-Rivlin	$C_1 = 0.16$kPa $C_2 = 0.14$kPa $K = 11.11$kPa	[28]
Linear properties	$\lambda = 8.939$ MPa $\mu = 90.3$ kPa	[10]

Experimental results on a regular meshed cube

We ran the experiment for the three meshes A, B and C. The precision is calculated as mentioned in section. Figure 3.23 represent the quantitative results of all mesh with different deformed parts. Figure 3.24 show the speed convergence of our method and the classic method. We use the logarithm with the

base 10 to display the axis of execution times. Our remark for this experiment is that the proposed method is also faster then the classic method.
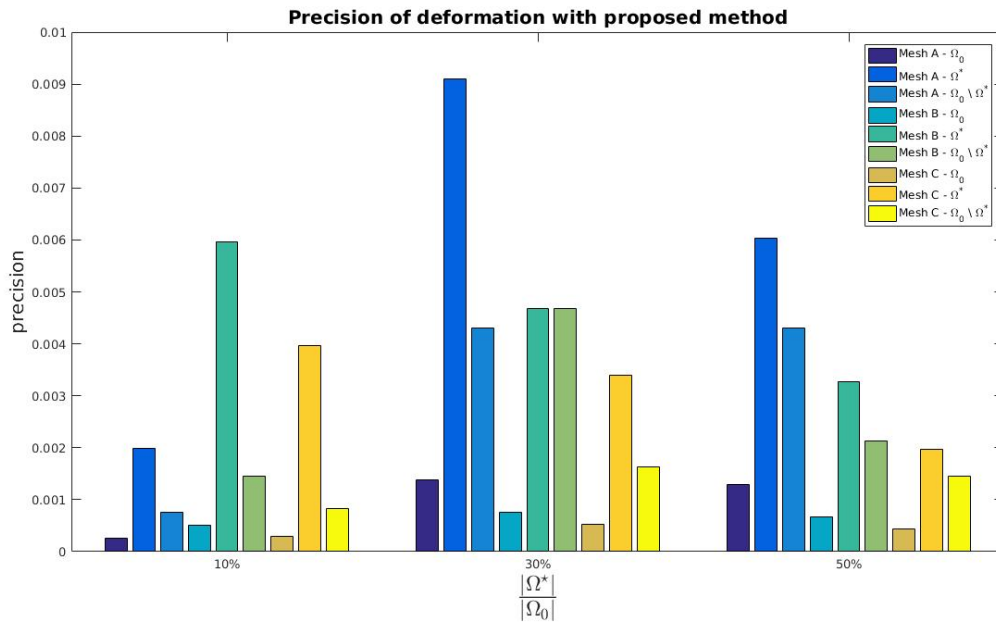

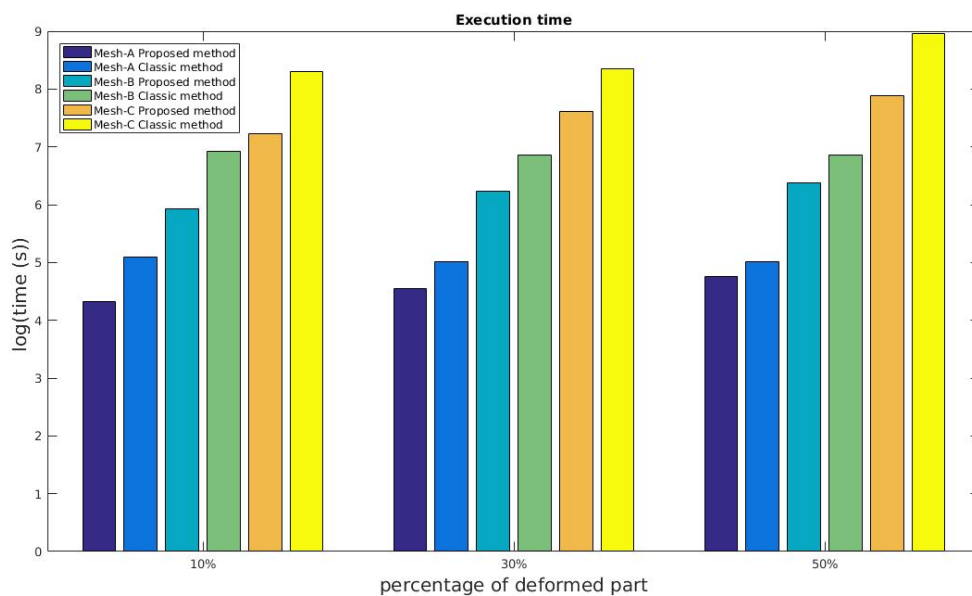Figure 3.23: Precision of reconstructing deformations with proposed method.

Figure 3.24: Execution time of the proposed method and Newton-Raphson method for the three meshes.

Figure 3.25, 3.26 shows the qualitative results of deforming mesh A with deformed part $\frac{|\Omega^\star|}{|\Omega_0|}$ of 10% and 50%. When the deformed part is less than 30% the result of convergence is almost similar to the Newton-Raphson method result. On the other hand, for a deformed part greater than 30% the proposed method loses its precision.
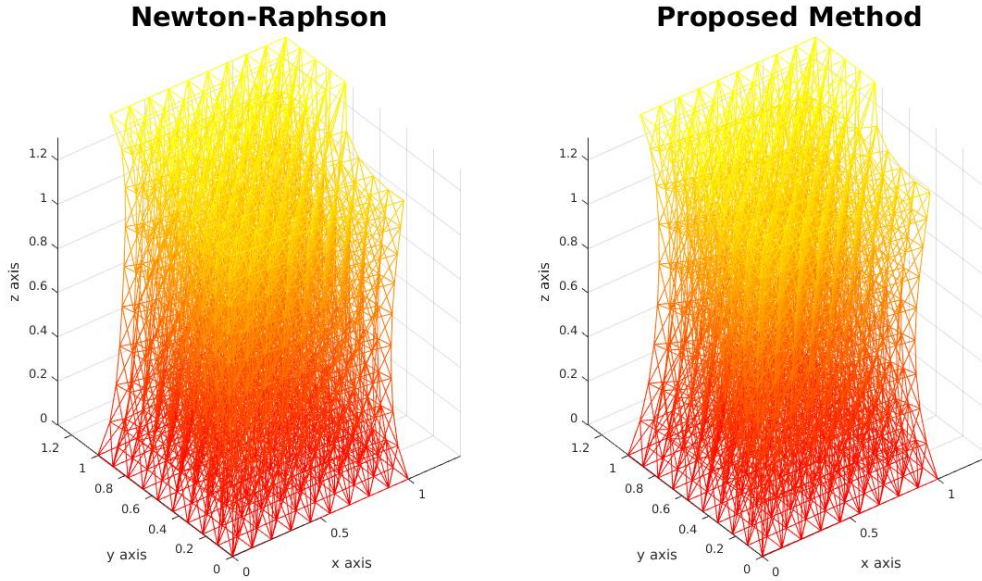
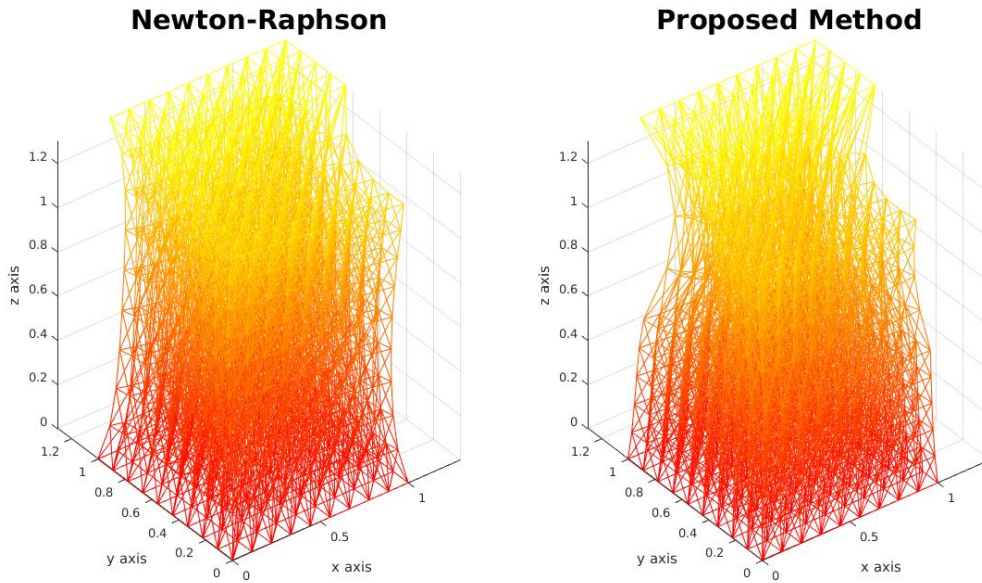Figure 3.25: Deformation of mesh A with $\frac{|\Omega^\star|}{|\Omega_0|} = 10\%$.

Figure 3.26: Deformation of mesh A with $\frac{|\Omega^\star|}{|\Omega_0|} = 50\%$

Experimental results on non regular Liver mesh

We perform test on non regular liver mesh. The imposed displacement of 6 mm is obtained with a displacement loop of 1 mm. In these experiments, we note that the $Init\_L$ method does not converge for the parts $\frac{|\Omega^\star|}{|\Omega_0|}$ greater than 20%. Also, it does not converge with displacement up than 1 mm. The execution time of deformation with $\frac{|\Omega^\star|}{|\Omega_0|} = 20\%$ four our method is $5.4924e + 03$ s and for Newton-

71

Raphson method is $1.6082e + 04$ s. So, the proposed method is faster than the classical method. Figure 3.27 represent the qualitative result of deformation with $\frac{|\Omega^\star|}{|\Omega_0|} = 20\%$.
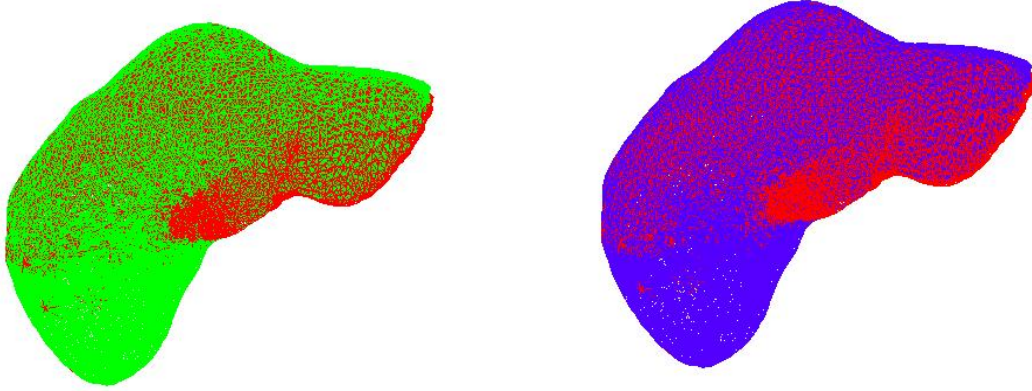

Figure 3.27: Deformation of liver with $\frac{|\Omega^\star|}{|\Omega_0|} = 20\%$

3.7.3 Discussion

In this experimental section, we test the two proposed method by comparing it by the Newton-Raphson method. We perform two tests, one for regular mesh and the other for non-regular mesh we take Liver mesh as example. We take three different parts of $\frac{|\Omega^\star|}{|\Omega_0|}$ for the three meshes A, B and C. The result obtained show that this proposed $Init\_L$ method loss its precision when $\frac{|\Omega^\star|}{|\Omega_0|}$ is upper than 30%. For Liver mesh, the result obtained with $\frac{|\Omega^\star|}{|\Omega_0|} = 20\%$ indicate that our method is faster than the classical method with keeping the precision. In other case, with $\frac{|\Omega^\star|}{|\Omega_0|}$ greater than 20% the solution lose the convergence. In addition, this method does not converge with displacement upper than 1 mm. Comparing with $Init\_0$ method which the result can converge with displacement upper than 4 mm and with different parts of $\frac{|\Omega^\star|}{|\Omega_0|}$. From the point of view of improving the speed of convergence, the proposed method serves to achieve this objective.

3.8 A comparative study with other constitutive models

The nonlinear mechanical behavior of hyperelastic tissues has been extensively studied by several researchers. In this part, we propose to compare three models of hyperelastic behavior: Mooney-Rivlin, Neo-Hookean and Saint Venant-Kirchhoff. As shown above in Table 1.1, the simplest hyperelastic material model is the Saint Venant-Kirchhoff model which has a linear relationship between stress and strain [25]. The Neo-Hookean model is a particular case of the Mooney-Rivlin model, with parameter $C_2 = 0$. And its justification is more molecular than phenomenological[7]. The two models Mooney-Rivlin and Saint Venant-Kirchhoff are classified as phenomenological models and the Neo Hookeen model is classified as mechanistic models. A test is carried out for the three models on a regular and non-regular mesh as indicated in the following subsections. We chose the mechanical properties of the liver that we found in the literature of the three models (see table 3.9). For this comparative experiment, we perform tests with our first method ($Init\_0$) discussed in 3.4.

Table 3.9: Hyperelastic material models of liver tissue

Mooney-Rivlin	$C_1 = 0.16\text{kPa } C_2 = 0.14\text{kPa } K = 11.11\text{kPa}$	[28]
Saint Venant-Kirchhoff	$\lambda = 0.235\text{Pa } \mu = 0.333\text{Pa}$	[43]
Neo-Hooken	$C_1 = 3.7\text{kPa } K = 11.11\text{kPa}$	[80, 28]

3.8.1 Experimental results on regular meshed cube

First test : We ran a first experiment on the regular mesh A. We took a fixed part of 10% of the total mesh and a nonlinear part of $\frac{|\Omega^\star|}{|\Omega_0|} = 10\%$. We imposed a non-zero displacement of 3 mm on 5% of the vertex. We ran this experiments on core i3 lap-top with 4Go RAM and Matlab2016a.

Figure 3.28 show the execution time for the three models with imposed displacement of 3mm. We can say that Saint Venant-Kirchhoff is faster in computation of tangential stiffness matrix then Mooney-Rivlin and Neo-Hookean. Figure 3.29 present the precision of nonlinear deformation with the three hyperelastic material models. We observed that for a displacement of 3 mm the Saint Venant-Kirchhoff model has a better pressure compared to Monney-Rivlin and Neo-Hookean. Also, the Monney-Rivlin model take the second place after the Saint Venant-Kirchhoff model whether for execution time or for precision. The qualitative result of deformation for the three models depends on the identification of the constant materials for each model (see figure 3.30)
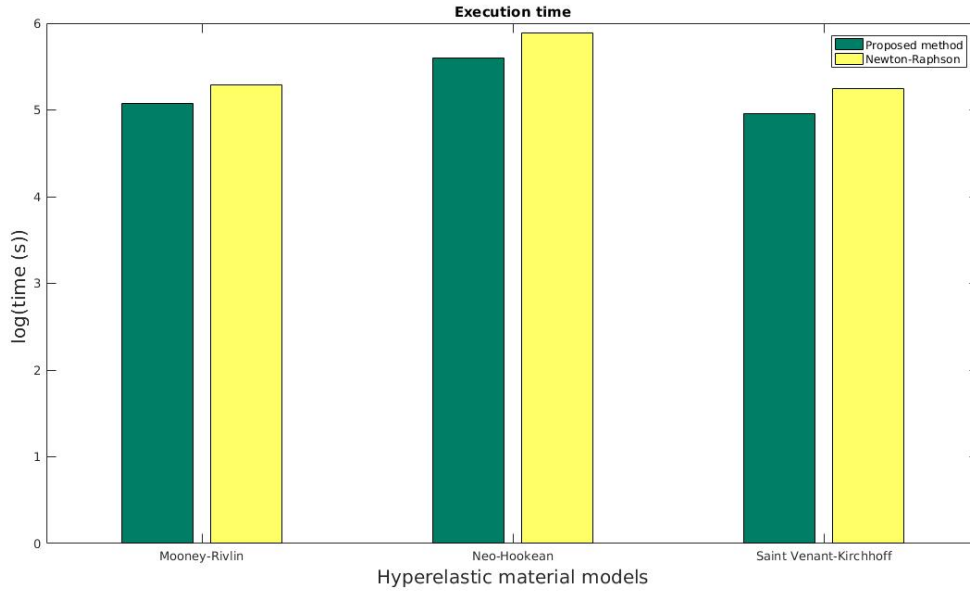

Figure 3.28: Execution time with imposed displacement of 3mm for the three models: Mooney-Rivlin, Neo-Hookean and Saint Venant-Kirchhoff
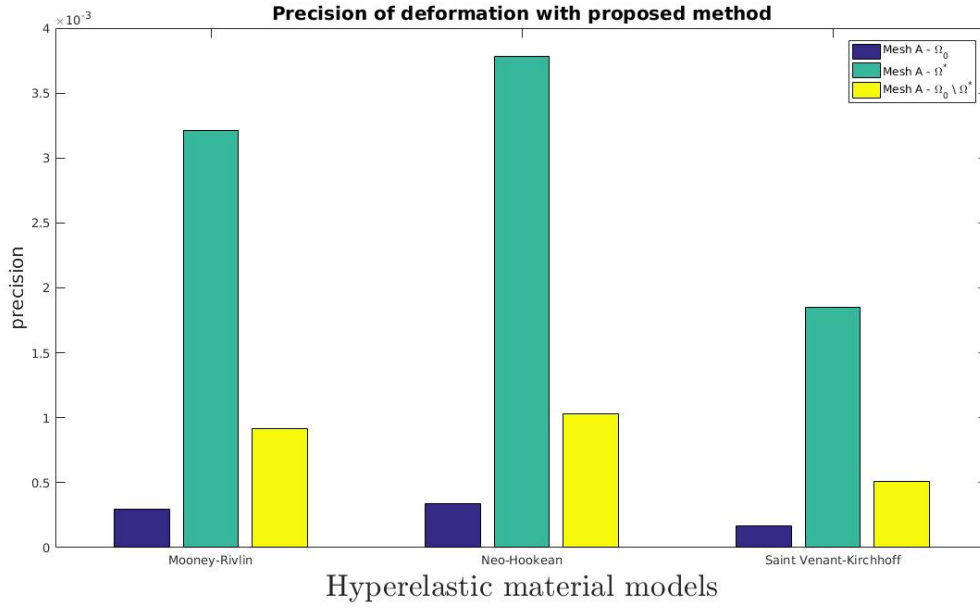
Figure 3.29: Precision deformation with imposed displacement of 3mm for the three different material models
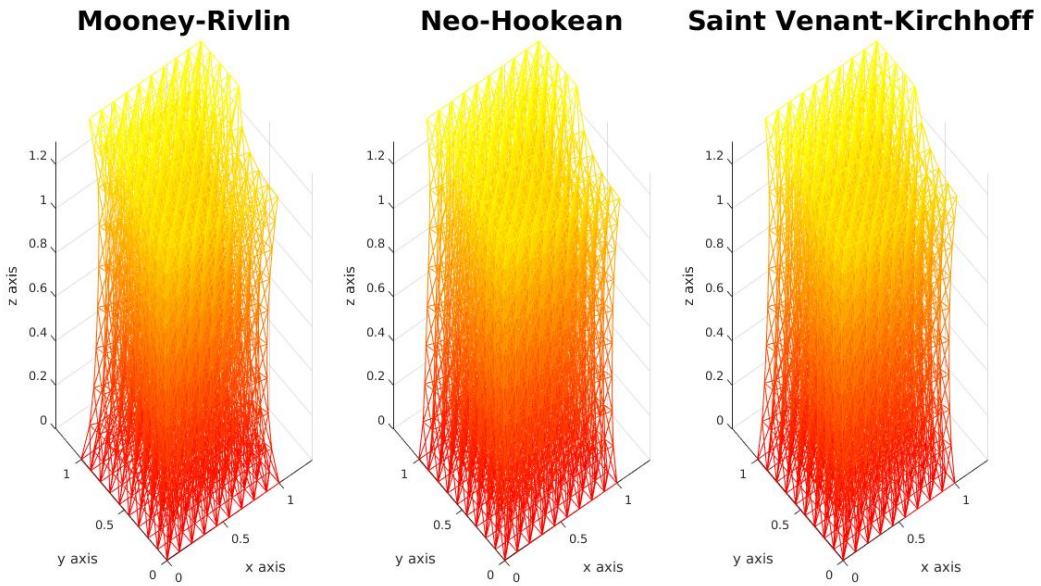

Figure 3.30: Result of deforming mesh A with $\frac{|\Omega^\star|}{|\Omega_0|} = 10\%$ for the three compared models

Second test : For a better comparison between the three models we perform test for a deformation of 50%. Where, we impose a displacement of 5mm instead of 3mm with the same part considered in the first test.
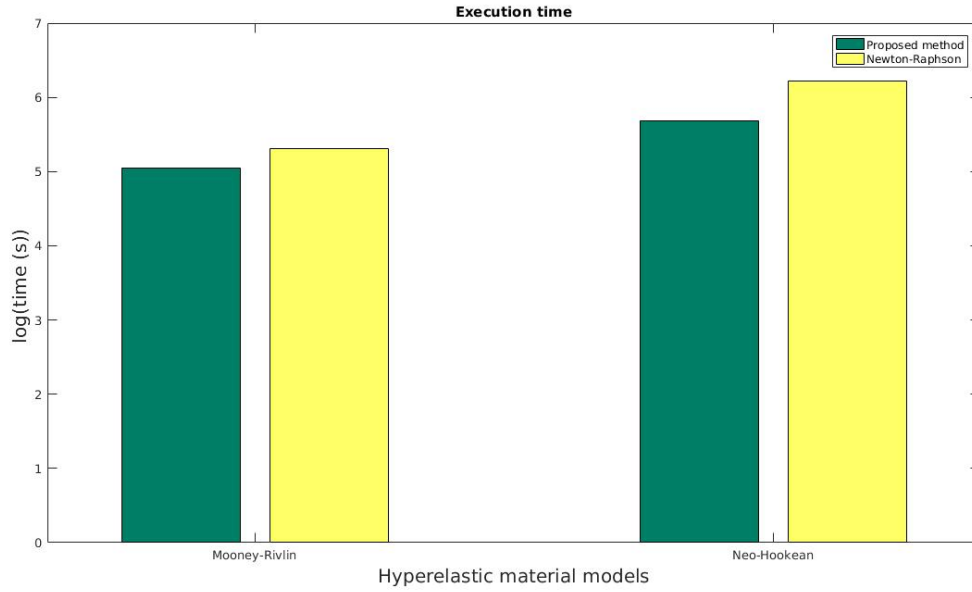
74

Figure 3.31: Execution time with imposed displacement of 5mm for the two models: Mooney-Rivlin and Neo-Hookean
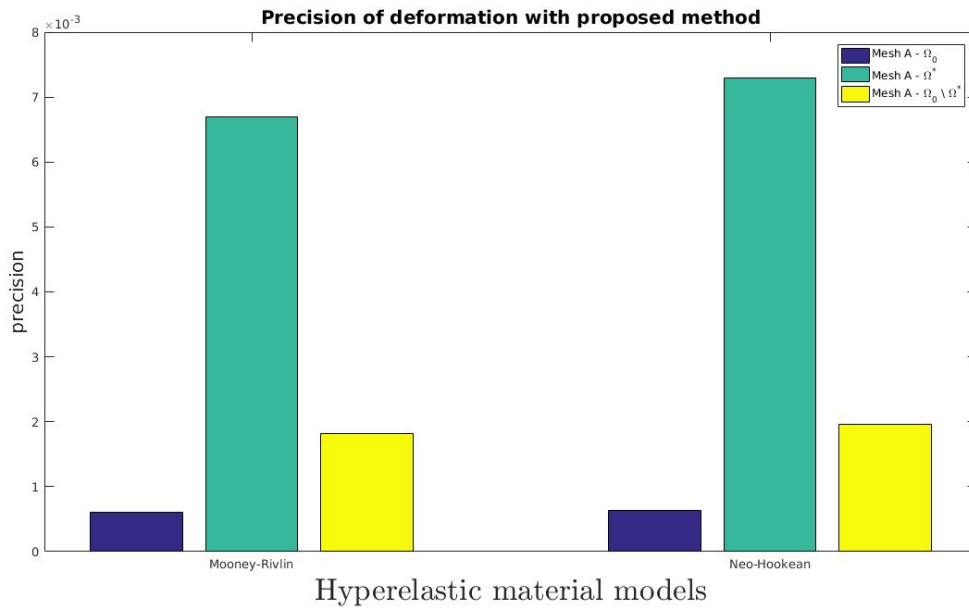

Figure 3.32: Precision deformation with imposed displacement of 5mm for the two material models

In this experiment, Saint Venant-Kirchhoff lost the convergence for a large deformation. On the other hand, the other two methods naturally converge. For quantitative result, the Mooney-Rivlin model is considered the best hyperelastic material model for large deformation. As show in both figure 3.31 and 3.32 of the time of convergence and precision respectively. Figure 3.33 represent the qualitative result of deformation for the both models (Mooney-Rivlin and Neo Hookean). Our remark for Neo-Hookean
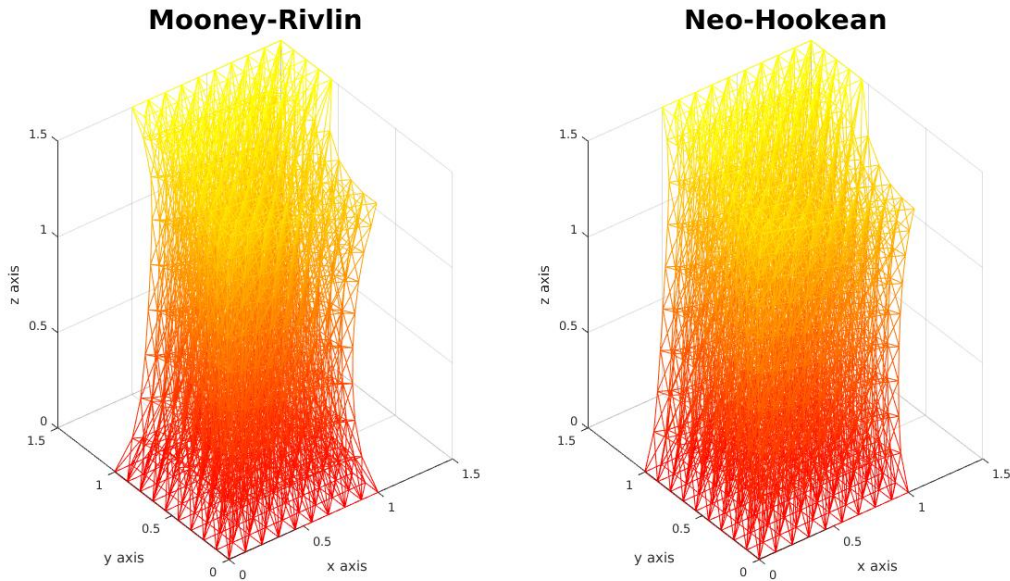
model that is not compressible.

Figure 3.33: Result of deforming mesh A with $\frac{|\Omega^\star|}{|\Omega_0|} = 10\%$

3.8.2 Experimental results on a non-regular liver mesh

In this experiment section, only Mooney-Rivilin model which converged for the two methods compared with an imposed displacement of 40mm as it is shown in figure 3.22 . The Neo-Hookean model converged for a value less than 30mm for the classic method but by the proposed method it did't converge. This model converges for a lower displacement value of 8mm for the proposed method. For the Saint Venant-Kirchhoff model the solution does not converge for both method if the imposed displacement is greater than 3mm. We conclude that for a large deformation the Mooney-Rivlin model is the best model chosen to solve the nonlinearity by our method.

3.8.3 Discussions

The constitutive laws for the mechanical response of hyperelastic models make it possible to predict the nonlinear elastic response in large deformation. They are numerous and widely available in structural computation tools. In this section, we present and compare the results of deforming meshes with the three models well known in the literature which are: Mooney-Rivlin, Neo-Hookean and Saint Venant-Kirchhoff. The results obtained in the experiments treated above show that the Saint Venant-Kirchhoff method solves nonlinear problems for small displacements. The Neo-Hookean model is adapted to the nonlinear problem with large deformation for the classic method but on the other hand for greater values of displacement than 8 mm this model loses convergence in our method. The Mooney-Rivlin model is widely used for hyperelastic tissues. This model proves its reliability in solving nonlinear problem with large deformation as it's noticed in this thesis where it can converge with a displacement value of 40 mm for the two methods compared.

3.9 Comments on the conditioning of the stiffness matrix and its impact on convergence

In numerical analysis, conditioning measures the dependence of the solution of a numerical problem on the data of the problem. This in order to check the validity of a solution computed with respect to these data. The inverse stiffness matrix must be well conditioned to avoid very important model errors. We say that a matrix is well conditioned if its conditioning is not much greater than 1. Thus, a badly conditioned matrix if its conditioning is high. Conditioning is linked to the choice of the polynomial base and to the geometry of the elements. In our work, we find that the norm of the inverse of $\mathscr{K}_T$ is very high as shown in the two Tables 3.3 and 3.6. It's implies that the tangential stiffness matrix is not well conditioned. This problem remains a point to solve in the future work.

Table 3.10: Conditioning Values.

Mesh	Estimation	Proposed method
A	$\|\mathscr{K}_T(\overline{U}_h)^{-1}\|_F$	2.4819e+05
B	$\|\mathscr{K}_T(\overline{U}_h)^{-1}\|_F$	6.4532e+05
C	$\|\mathscr{K}_T(\overline{U}_h)^{-1}\|_F$	1.4451e+06
Liver	$\|\mathscr{K}_T(\overline{U}_h)^{-1}\|_F$	8.4770e+05

3.10 Conclusion

In this chapter, we define our main ideas on the optimization of computation time. We propose two methods: The $Init\_0$ method which decompose the domain Ω_0 into two sub-domain (Ω^* and $\Omega_0\backslash\Omega^*$). This method initializes the global matrix $\mathscr{K}_T$ with a zero displacement and the deformed part of $\mathscr{K}_{\omega^e}$ is treat at each iteration in the iterative process . The $Init\_L$ method has the same idea of the decomposition of the domain as the $Init\_0$ method. This method initializes the matrix $\mathscr{K}_T$ with linear elastic material and Ω^* which will be treated at each iteration with nonlinear hyperelastic material. We perform tests on our proposed methods for different meshes with number of nods equal or more than 1000. We compared our results with the classic method and we note a difference in the computation time of more than 8 times for the different meshes with different deformed part $\frac{|\Omega^\star|}{|\Omega_0|}$. Then, we use three nonlinear constitutive models and we conclude that the Sain Venant-Kirchhoff model does not converge for a large displacement of 50% either with the classic method or with our method. Neo-Hookean converges for a displacement up to 80% by our method. Mooney-Rivlin is the most suitable for our method where it can converge with a displacement upper than 80%.

Chapter 4

Surgical simulation based on virtual reality

4.1 Introduction

Virtual reality is a series of computer technologies that aim to immerse one or more people in a virtual environment created by software. It can be a reproduction of the real world or a totally imaginary environment. The experience is both visual, oral and, in some cases, haptic with the production of senses-toutch feedback. When the person is equipped with the appropriate interfaces, such as gloves or clothing, they can experience certain sensations related to touch or certain actions (blow, impact, etc.)[54]. The use of virtual reality in the medical setting has a positive influence on the learning performance of surgeons. They can learn the anatomy and physiology of the human body, perform endoscopic or laparoscopic simulations, and even perform complex surgical procedures [35]. The major problem in virtual reality-based surgical training is realism in soft tissue deformation or hyperelastic tissue. It is extremely important to define the minimum requirements for realism that training systems must provide to be effective [75, 36, 69]. Peterlik et al. [58] developed a pre-calculus procedure allowing haptic interaction. They used the static nonlinear FEM with geometric and material nonlinearities. This procedure is based on a notion of displacement in a configuration space which is precomputed in advance. Oshiro et al [52] developed Liversim, software which shows the deformation of models according to the user interaction in real time. This software is updated by Oshiro et al. [51] where it can incising the hepatic parenchyma and intrahepatic vessels depending on the user's operations. It converts models of organs such as the liver and gallbladder into quadrilateral mesh models with physical simulations based on the finite element method. Zhang et al. [79] proposed a method for modeling soft tissue deformation based on the neural network. This method presents a nonlinear force-displacement relationship and the associated nonlinear deformation behaviors of soft tissue. This method aims to simulate the deformation of soft tissues in real time, and make it realistic and stable. In this chapter, we present some commercial surgical simulator. We expose the design steps of our simulator. Finally, we perform test on virtual liver and gallbladder tissues.

4.2 Examples of commercial surgical simulator

Simulation training is constantly associated with a significant improvement in knowledge, practices, risk management and behavior. There are many commercial surgical simulators for different domains of application. Next, we present some commercial simulators.

Vtopia Surgical : This simulator trains users to perform operations in a virtual environment. It is

produced by the French team of ETR (figure 4.1).

Figure 4.1: Vtopia Surgical is a virtual reality simulator for the training of surgeons. https://lab.troisprime.com/wp-content/uploads/2017/10/Vtopia_surgical_bariatrie-e1519145789560.png.

ALT 60100-Paracentesis simulator : This simulator allows users to learn diagnostic and therapeutic techniques. Using ultrasound guidance, the user can visualize the insertion site and check vital organs (figure 4.2). It is made by Limbs & Things in the United Kingdom.

Figure 4.2: ALT 60100 - Paracentesis simulator ALT 60100 Limbs & Things https://www.medicalem. com/6158-fiche_product/alt60100-alt60100-simulateur-de-paracentese-limbs-things.jpg.

ANGIO Mentor : Provides a clinical environment of an operating room for the training of intervention teams (figure 4.3). This simulator is used in several medical companies in the endovascular domain such as Cordis, Boston Scientific, Endologix and Corindus.

Figure 4.3: Simbionix ANGIO Mentor. Endovascular training simulator https://img.medicalexpo.com/images_me/photo-pc/81276-7614071.webp.

CAE LapVR™: This simulator allows users to learn and master techniques such as suturing, knotting and tying the loop, as well as some commonly performed laparoscopic surgeries such as gallbladder removal and horn occlusion (see figure 4.4). It is a product of the company CAE Healthcare which located in Florida, United States.

Figure 4.4: CAE LapVR™laparoscopic simulator https://www.caehealthcare.com/images/made/media/images/LapVR-teaching_1024_774_s_c1.jpg.

Our simulator has the same objective of training as the simulators presented above. Our simulator consist of headset HMD and controllers as the simulator Vtopia Surgical. With the headset HMD the

user can react to the virtual environment and he can train and perform surgeries on a virtual human body using the controllers.

4.3 Components of our surgical simulator

A surgical simulator consists of a visual part and a haptic part. The visual part consists of a virtual image resulting from the infographic manipulation of 3D models representing human organs. The haptic part makes it possible to restore to the user the sensation of force feedback due to manipulations on the organs. The haptic device acts as a surgical tool that helps the user interact with the virtual model of the organ. A computer system processes the deformations applied to the virtual organ and performs calculations and updates on the latter (figure 4.5). The functioning of virtual reality in surgical simulation is based on 5 main components: (1) Headset HMD. (2) Controllers. (3) Motion sensors. (4) The audio system. (5) The computer.
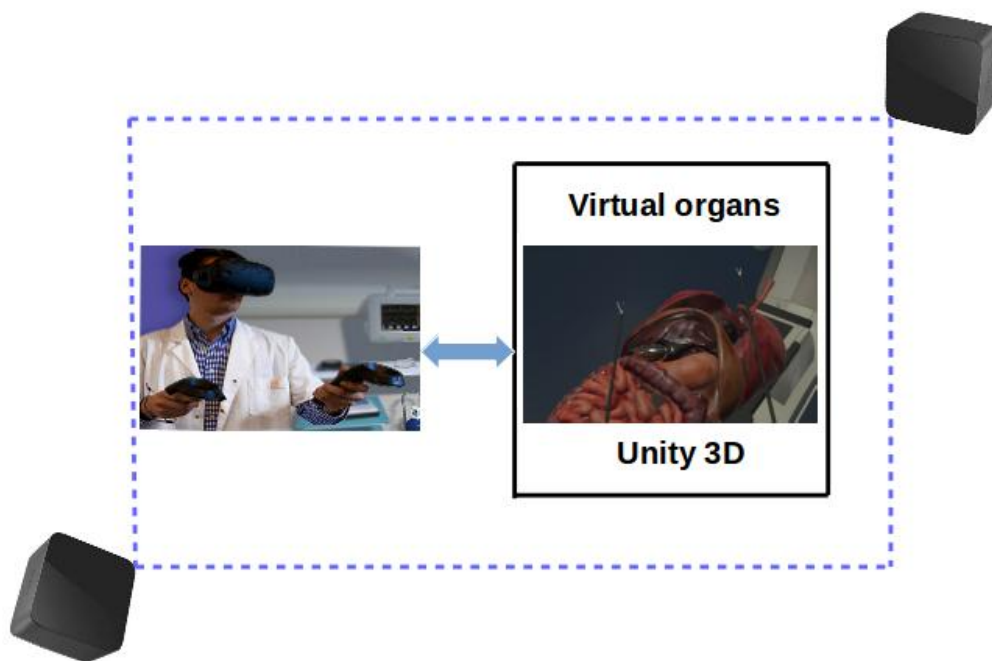

Figure 4.5: Surgical simulator based on virtual reality.

4.3.1 Materials

Headset HMD

The virtual reality headset is a contact between the user and the virtual environment. This headset is called "HMD" or "Head Mounted Display" (see Figure 4.6). The virtual reality headset consists of two miniature televisions, allowing monoscopic or stereoscopic vision. The "tracker" sensor on the top of the helmet responds to the user's head movements, allowing the user to visit three-dimensional (3D) environments.

Figure 4.6: Headset HMD https://blogue.bestbuy.ca/wp-content/uploads/sites/3/2017/01/10460569. jpg, https://static.wixstatic.com/media/d55152_4f0cf98d67e742dbbe45702ff5d1c924~mv2.jpg/v1/fill/ w_360,h_192,al_c,q_90,usm_0.66_1.00_0.01/d55152_4f0cf98d67e742dbbe45702ff5d1c924~mv2. webp.

Controllers

Represents the user's hands in the virtual world. These controllers (see Figure 4.7) allow the user to interact with the environment through the sensation of touch and the force feedback when the user presses on a virtual object. In the surgical simulation these joysticks control the virtual surgical tools like the scissors, the forceps, etc.

Figure 4.7: HTC Controllers

Motion sensors

These sensors make it possible to follow the exact movement of the headset and the controllers (see figure 4.8). They offer a sensation of movement and life-size immersion. They can also locate the manipulation space in real space by warning the user when he exceeds the limits of that space.

Figure 4.8: Motion sensors

The audio system

The audio system allows auditory immersion by transcribing the sounds from the virtual reality experience.

Computer

Its role is paramount because it must be perfectly sized to meet the needs of virtual reality. To perform a surgical simulation based in virtual reality we need to use algorithms for the calculation of deformation and reaction and a development platform in real time.

4.3.2 Software

Unity 3D is a standard interactive application building tool that offers simple solutions for sensor integration. As part of the surgical simulation Unity 3D is used to display the operating scene, surgical tools and organs through the headset (see figure 4.9). The latter ensures communication between the components. For example, if the organ receives a force and a position from the controllers, the latter will translate the position of the controllers into a virtual tool position and transmit it to an algorithm to compute the deformation applied on the organ. Then, it sends the reaction force that will be produced by the controllers.

Figure 4.9: The operative scene of our surgical simulator **VRSurge**.

4.4　Integration of the proposed method in our surgical simulator

We performed our study in chapter 3 under Matlab (R2016a, 64-bit). To integrate it into the simulator, we coded our method in `C++` language under visual studio. Afterwards, we linked the code from `C++` to `C#` by using DLL file. Where, as part of a `C#` project, we need to use libraries (.DLL) to make a link between `C++` and `C#`. To be able to integrate it into Unity 3D as show in figure 4.10.

The instructions for the coding languages are different. This complicates the translation from one language to another. In this case, we followed the same steps taken in the matlab code and we coded them in `C++`. This code transfer was done using two libraries Eigen and VTK.
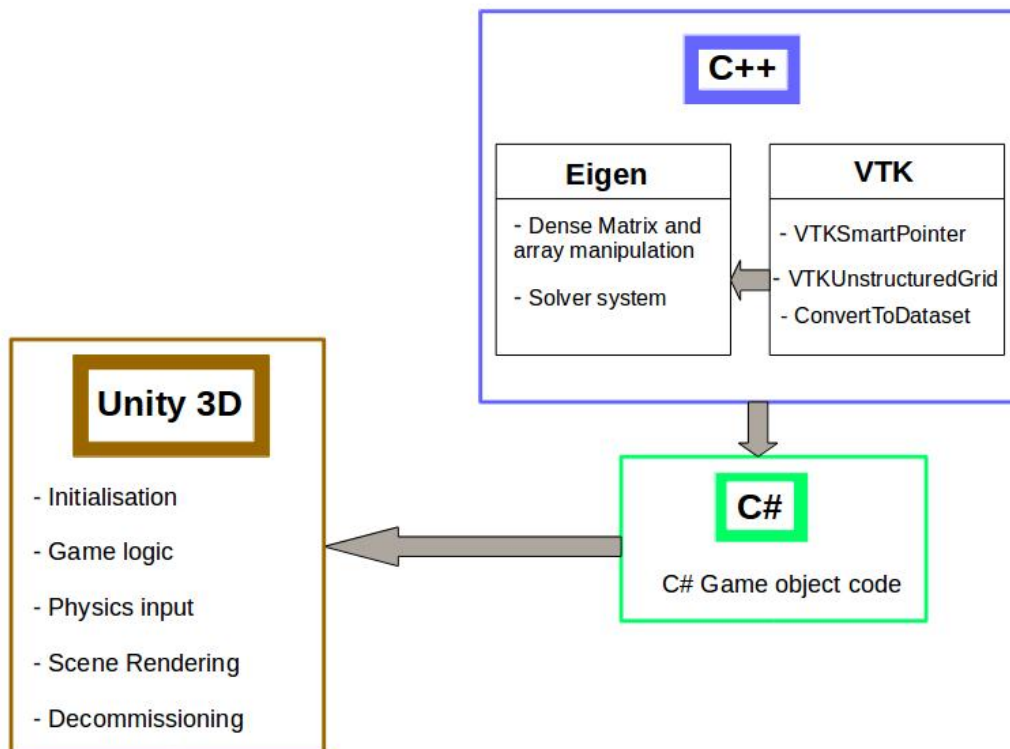
Figure 4.10: Functional architecture of the proposed simulator.

VTK library

VTK is a library for 2D and 3D data visualization and image processing. It contains over 1100 `C++` classes. We used this library to read and write ".vtk" format files. The mesh data studied are in ".vtk" format. As shown in figure 4.10 we get all data from the file with class "VTKSmartPointer". Then, we read the data with class "VTKUnstructuredGrid". To obtain the vector nodes and matrix of tetrahedron elements we use "ConvertToDataset" class which convert vtk file to Eigen vector and matrix. Afterwards, we process this data through the iterative process. At the end of this analysis, we save the results by writing them in ".vtk" file format.

Eigen

Eigen is a template `C++` library for numerical analysis, which includes a linear algebra tools, such as matrix and vector operations. This library allows the use of static or dynamic memory allocation for its matrices and a large number of solvers for sparse matrix. This space has help us a lot to achieve mathematical operations on matrices and vectors. We used the "Dense" class for arithmetic calculations such as the sum, the multiplication, the transpose of a vector or matrix using the function "transpose ()", the determinant and the inverse of a matrix by the functions "determinant ()", "inverse ()".
Also, to generate an identity matrix we used the function "Identity ()", matrix or vector zero by the function "Zero()". To allocate a memory space of a large matrix or vector we used the "Sparse" class. This class allows us to generate vector and matrix sparse using the functions "SparseVector <>", "SparseMatrix <>".

Description of the simulated surgical scene

The virtual operating room

The operating room represents one of the major sectors and certainly one of the most emblematic, as a centerpiece of the technical platform. In this room we find all the devices and tools necessary to perform a surgical operation (For example, multi-parameter monitoring monitor, diagnostic lamp and operating table) as shown in figure 4.9.

Organs

In the virtual scene, the human body exists with all of its virtual organs placed on the operating table. This helps the user to feel that he is in reality and undergo surgery on it (see figure 4.11).Of course, these organs can be easily covered by a numerical male or female body.
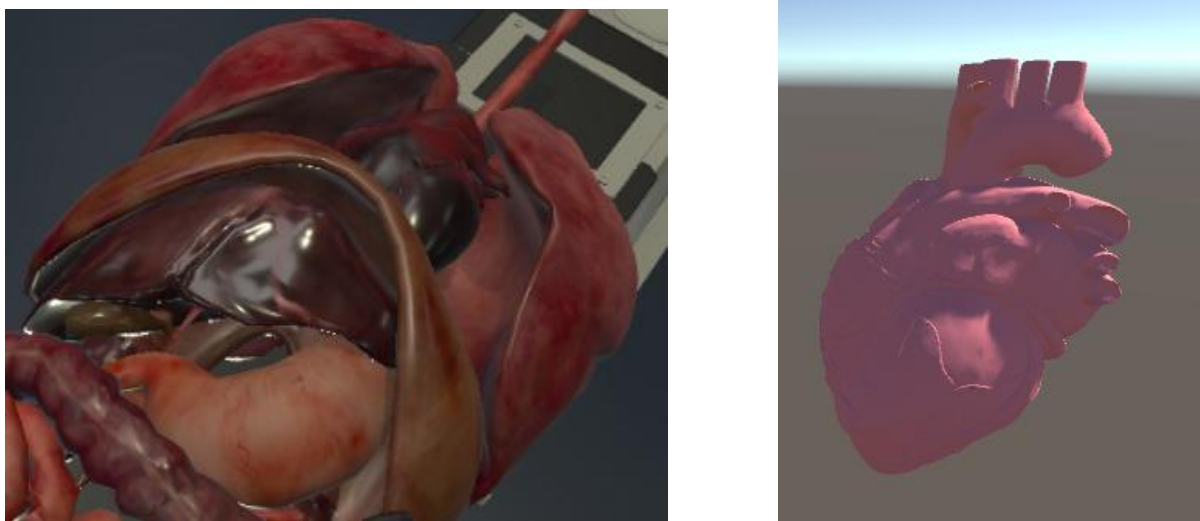

Figure 4.11: Virtual organs in our **VRSurge**.

Tools

Surgical instruments such as scissors and pincers (figures 4.12, 4.13) must serve the various functions useful to operators: palpation, grasping, section, dissection, suture and destruction.
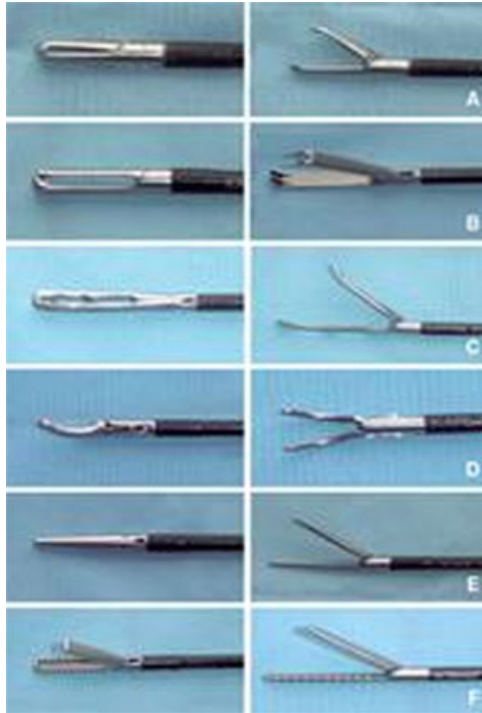
Figure 4.12: Pincers of surgical simulation. A) Grip pincer. B) Extraction pincer. C) Fenestrated digestive pincer. D) Dissector. E) Thin flat pincer. F) Biopsy pincer http://campus.cerimes.fr/ chirurgie-generale/enseignement/coelioscopie/site/html/6_2.html.
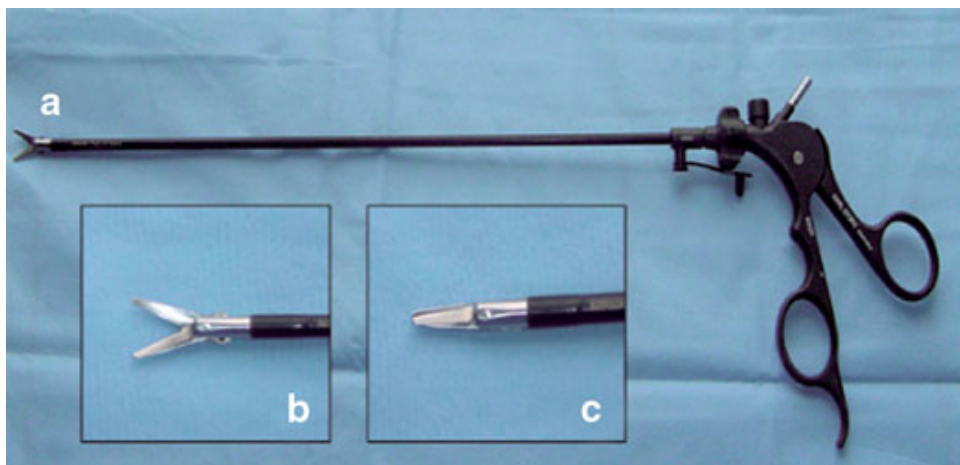

Figure 4.13: a) scissors. b) open scissors. c) closed scissors http://campus.cerimes.fr/chirurgie-generale/ enseignement/coelioscopie/site/html/6_2.html.

4.5 Use case on hepatobiliary surgery

Test on virtual liver tissue

In this experiment, we tested our proposed surgical platform as show in figure 4.14, 4.15 and 4.16. We pinched part of the liver with virtual surgical tools and we moved it.
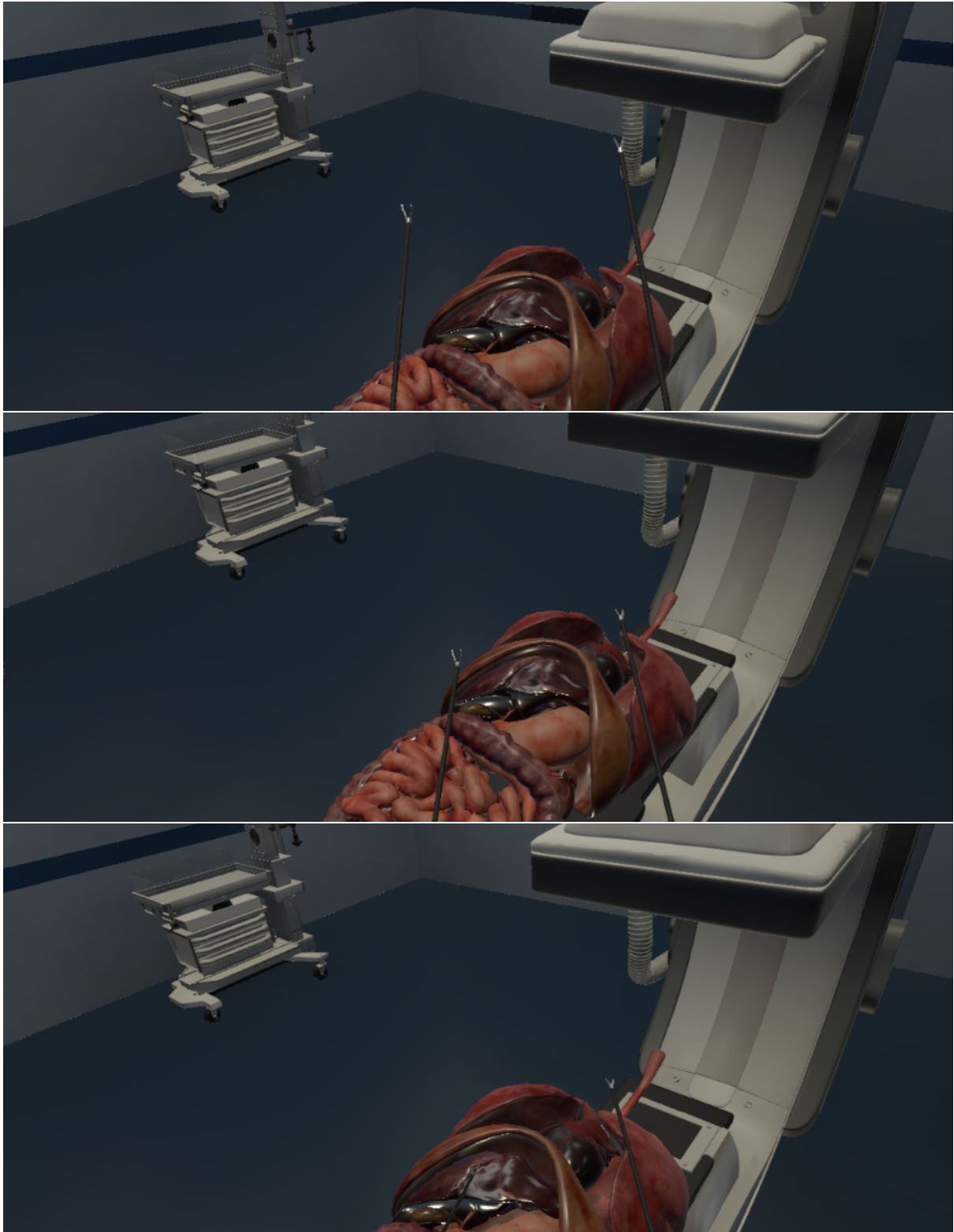
Figure 4.14: Pinch the liver in our **VRSurge**.
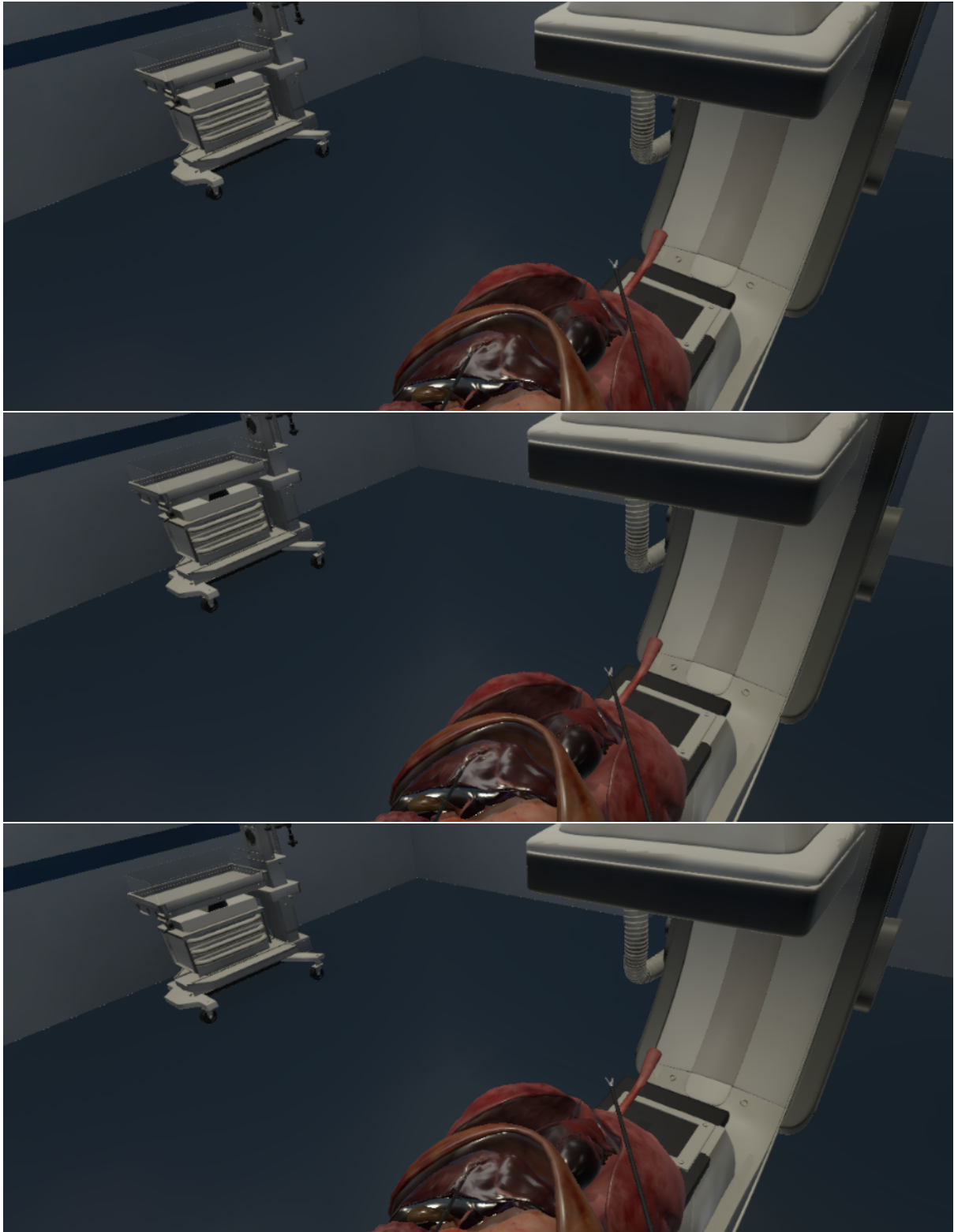
Figure 4.15: Steps of deforming the liver in our **VRSurge**.

Figure 4.16: Steps of deforming the liver in our **VRSurge**.

Test on virtual gallbladder tissue

We performed test on gallbladder tissue where we pinched one side of the tissue and with the scissor we cutting the other side. In the end, the gallbladder is eradicated (see figures 4.17, 4.18 and 4.19).

Figure 4.17: Pinch and cut the gallbladder in our **VRSurge**.
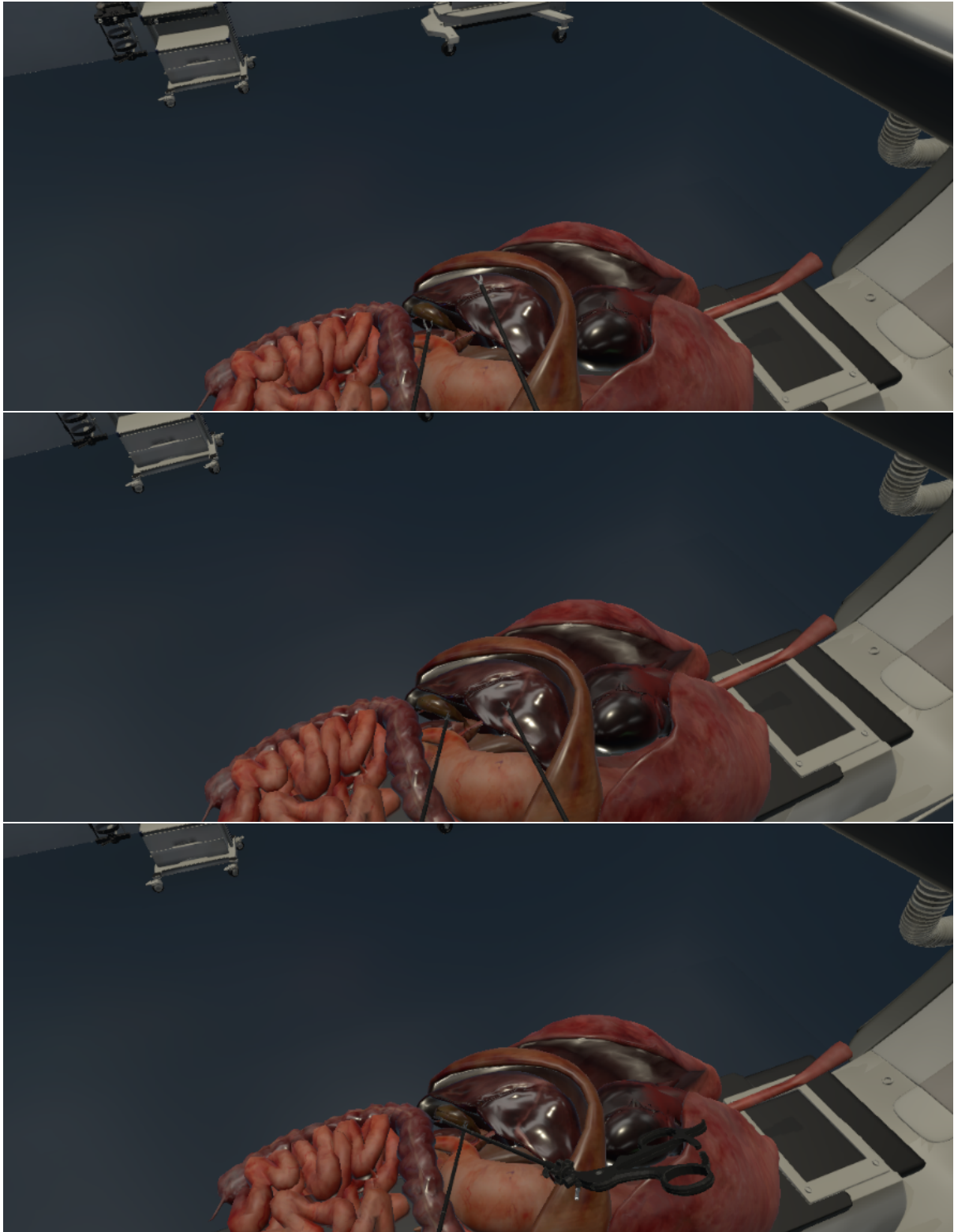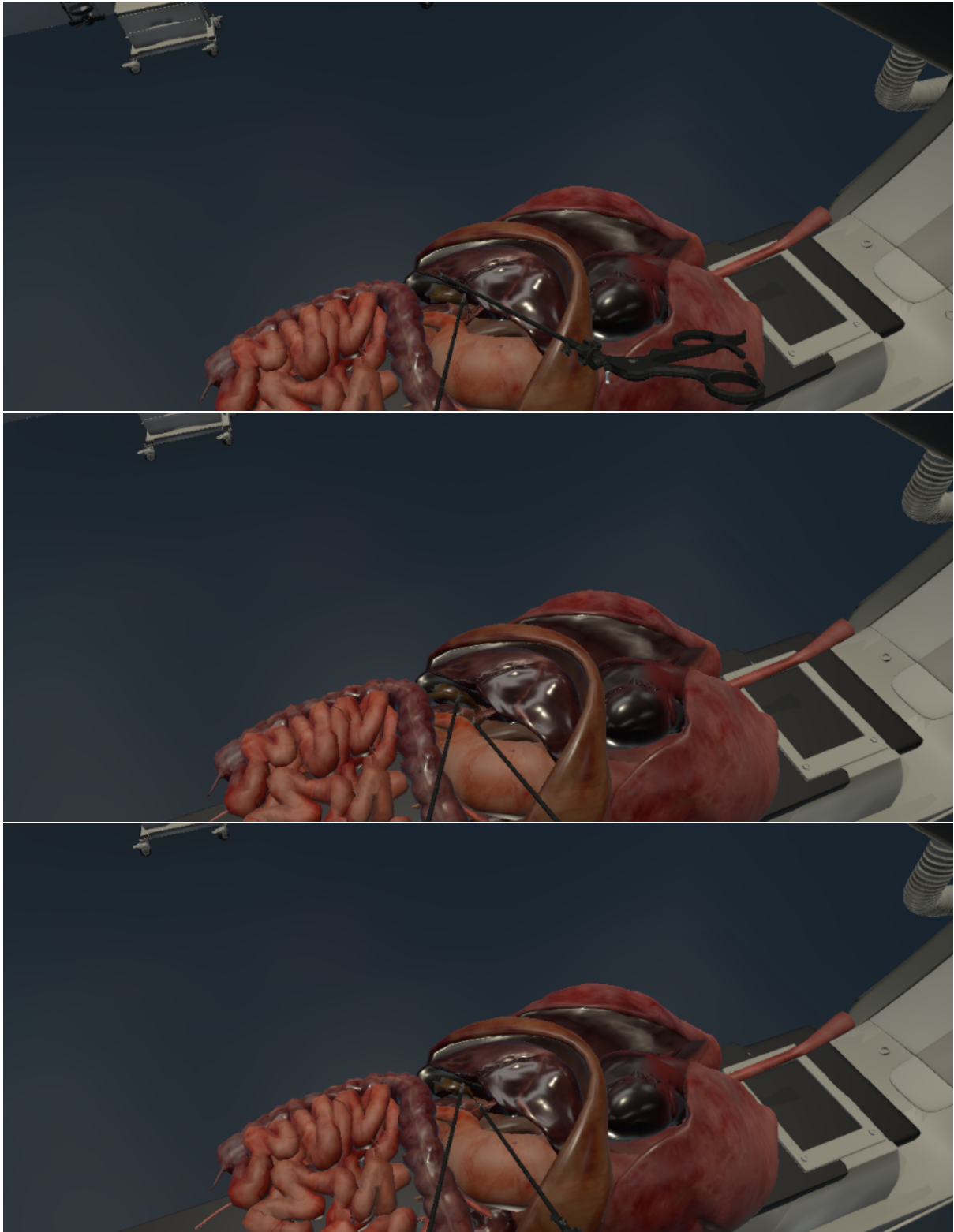
Figure 4.18: Steps of cutting the gallbladder in our **VRSurge**
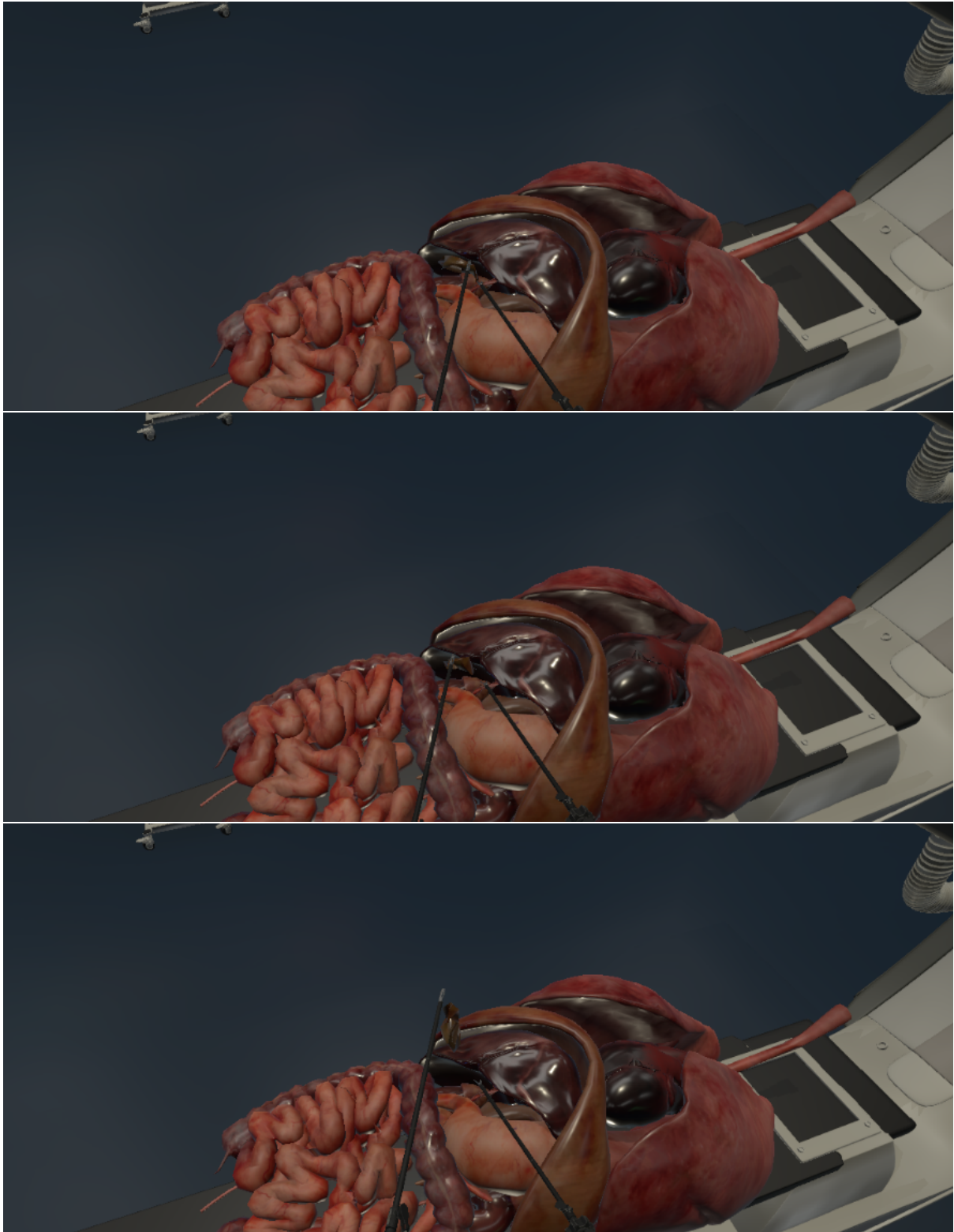
Figure 4.19: Steps of cutting the gallbladder in our **VRSurge**

4.6   conclusion

This chapter shows our designed surgical simulator. The components used to realize a simulator based on virtual reality such as material and software. Our method is integrated on unity 3D software with C#code which is the translated code of C++. The C++ code is realized using two libraries VTK and Eigen. The VTK library made it easy for us to read and write a data file. Eigen library allowe us to practice mathematical operations on large matrices and vectors. We perform test on virtual liver and gallbladder tissue. Finally, we prove the effectiveness of our proposed method with our surgical simulator. We showed the usefulness and the effectiveness of the proposed simulator. This design represent a starter prototype that will be further developed and commercialized for medical education purpose.

Conclusion

This thesis concerns the development of a surgery simulator. We identified the precise and fast computation of deformation as one of the critical problems of this development. We determine the biomechanical modeling of soft tissue which is a very sensitive step in the construction of a surgical simulator. Most soft tissues are described in the context of hyperelasticity to take into account the fibrous structure of these tissues. The modeling of hyperelastic tissues is studied in the continuous medium for its. A large deformation and displacement leads to a nonlinear structural mechanics. Nonlinearities are associated with material, geometry, applied forces and boundary conditions. We interested in this research to solve the nonlinear deformation of hyperelastic tissues. The resolution of these deformations by the nonlinear finite element method with the iterative process of Newton-Raphson poses a problem in real time. In the surgical simulation, the precision and the speed in resolution of the deformations are the main factors to realize a simulator imitated to reality. Solving deformation problems of hyperelastic tissue using Newton-Raphson method has an inconvenient, when the tissue is represented by a large mesh then the cost of computation and the speed resolution becomes very slow. Therefore, our objective is to improve the resolution time for nonlinear problems with the iterative Newton-Raphson process and to keep the deformation precision using the nonlinear finite element method. The Newton-Raphson method is known in theory by its quadratic convergence if the initial value is very close to a root. But in practice, this information is not sufficient. The famous hypothesis used as a sufficient condition for the convergence of the Newton-Raphson method is that of Kantorovich's.

In this work, we verify the convergence of solution by Kantorovich's theorem. The computation of the radius of convergence by using Kantorovich's theorem is a difficult task. In the continuous domain, there is no formal expression which help us to estimate the norm of the inverse Fréchet derivative of the residue. Hence, there exists a lemma that allows us to bound this inverse given the discretized Fréchet derivative is bounded and given that the difference of these two linear operators is also bounded. Then, we propose two proposition with three hypotheses to estimate the radius of convergence. The three hypotheses has a positive constants c_1, c_2 and c_3. Which c_1 control the bound of the L^2-norm of the functional's gradient by the norm of the functional, c_2 control the bound of the L^2-norm of the functional by the projection of the functional and c_3 control the limit bound of the volume of the organ by the approximated discretized volume. The two proposition estimate the upper bounds of the Fréchet derivative of the residue and its inverse. In surgery, the operation is performed on a specific region of an organ. Whereof, we propose two methods which decompose the organ domain Ω_0 into two sub-domains (Ω^* and $\Omega_0\backslash\Omega^*$). Ω^* represent the sub-domain which the stain and the important displacement are located and $\Omega_0\backslash\Omega^*$ represent the remaining of domain. The first proposed method ($Init\_0$) reduces the computation of the tangential stiffness matrix by initialize it with non-zero displacement only once at the first iteration. Ω^* is the sub-domain which will be treated at each iteration. The strain and the important displacement are located in this sub-domain. We carry out tests on regular meshed cubes and non-regular liver mesh of this proposed method by comparing their results with the classical method and the method of Wang et al.[72]. This subdivision of the domain will reduce the computation about 5 times compared to the classic method. We note that our method is the fastest in the computational

cost comparing to the classical method and Wang et al. method. It has nearly the same precision of the classical Newton-Raphson method with substantial improvement in convergence speed. We calculate the convergence radius of this method with experimentally defined control parameters. We notice that the constants $\mathbf{c}_1$ and $\mathbf{c}_2$ take small values and that is due to the norm of the inverse of the stiffness matrix which is high. This problem is caused to the bad conditioning of the stiffness matrix. This issue is an open problem and will be investigated in future work. The second proposed method ($Init\_L$) models the sub-domain $\Omega_0 \backslash \Omega^\star$ with linear elastic material. Ω^* is the sub-domain which will be treated at each iteration and it is considered as a nonlinear hyperelastic material. We perform tests on regular meshed cube and non-regular liver mesh. We compare the results obtained of this proposed method ($Init\_L$) with the classical method. For regular mesh test, we observe that for $\frac{|\Omega^\star|}{|\Omega_0|}$ upper than 30% the precision is lost. But, it also speed than the classic method. For liver mesh, we note that for $\frac{|\Omega^\star|}{|\Omega_0|}$ upper than 20% the solution lose the convergence. Also, the solution cannot converge with displacement upper than 1 mm. The results obtained during the previous tests are carried out by the Mooney-Rivlin model. Therefore, we perform tests with other constitutive models as Saint Venant-Kirchhoff and Neo-Hookean. For large displacement as 5mm Saint Venant-Kirchhoff do not convergence. The quantitative result show that Mooney-Rivilin is the best constitutive model for large deformation.

The proposed method $Init\_0$ is integrated in our surgical simulator. This method is coded by Matlab program. To integrat it in our simulator we coded it in `C++` language using two libraries (VTK and Eigen). VTK library help us to read data from ".vtk" file format. Eigen library allows us to perform an arithmetics operations on vectors and matrices. It has a sparse class for carry out the arithmetics operations on sparse vectors and matrices, and solving the sparce matrix. After building the `C++` library, we create the DLL file which can be called from the `C#` code. Then, we integrate the `C#` code in Unity 3D. We perform test in this latter on liver and gallbladder tissues.

In future work, we hope to improve our method for different geometric and organ shapes. Also, to improve still more the convergence of the solution and the calculate of radius of convergence. Find a better approach to selecting the particular part of an organ.

Appendix A

Appendix

Shape function

V is the volume of the element given by:

$$2V = \begin{vmatrix} 1 & x_1 & y_1 & z_1 \\ 1 & x_2 & y_2 & z_2 \\ 1 & x_3 & y_3 & z_3 \\ 1 & x_4 & y_4 & z_4 \end{vmatrix} \tag{A.1}$$

Where α_i, β_i, γ_i and δ_i $(i = 1, 2, 3, 4)$ are given by;

$$\alpha_1 = \begin{vmatrix} x_2 & y_2 & z_2 \\ x_3 & y_3 & z_3 \\ x_4 & y_4 & z_4 \end{vmatrix} \quad \alpha_2 = - \begin{vmatrix} x_1 & y_1 & z_1 \\ x_3 & y_3 & z_3 \\ x_4 & y_4 & z_4 \end{vmatrix}$$

$$\alpha_3 = \begin{vmatrix} x_1 & y_1 & z_1 \\ x_2 & y_2 & z_2 \\ x_4 & y_4 & z_4 \end{vmatrix} \quad \alpha_4 = - \begin{vmatrix} x_1 & y_1 & z_1 \\ x_2 & y_2 & z_2 \\ x_3 & y_3 & z_3 \end{vmatrix}$$

$$\beta_1 = - \begin{vmatrix} 1 & y_2 & z_2 \\ 1 & y_3 & z_3 \\ 1 & y_4 & z_4 \end{vmatrix} \quad \beta_2 = \begin{vmatrix} 1 & y_1 & z_1 \\ 1 & y_3 & z_3 \\ 1 & y_4 & z_4 \end{vmatrix}$$

$$\beta_3 = - \begin{vmatrix} 1 & y_1 & z_1 \\ 1 & y_2 & z_2 \\ 1 & y_4 & z_4 \end{vmatrix} \quad \beta_4 = \begin{vmatrix} 1 & y_1 & z_1 \\ 1 & y_2 & z_2 \\ 1 & y_3 & z_3 \end{vmatrix}$$

$$\gamma_1 = \begin{vmatrix} 1 & x_2 & z_2 \\ 1 & x_3 & z_3 \\ 1 & x_4 & z_4 \end{vmatrix} \quad \gamma_2 = - \begin{vmatrix} 1 & x_1 & z_1 \\ 1 & x_3 & z_3 \\ 1 & x_4 & z_4 \end{vmatrix}$$

$$\gamma_3 = \begin{vmatrix} 1 & x_1 & z_1 \\ 1 & x_2 & z_2 \\ 1 & x_4 & z_4 \end{vmatrix} \quad \gamma_4 = - \begin{vmatrix} 1 & x_1 & z_1 \\ 1 & x_2 & z_2 \\ 1 & x_3 & z_3 \end{vmatrix}$$

$$\delta_1 = - \begin{vmatrix} 1 & x_2 & y_2 \\ 1 & x_3 & y_3 \\ 1 & x_4 & y_4 \end{vmatrix} \qquad \delta_2 = \begin{vmatrix} 1 & x_1 & y_1 \\ 1 & x_3 & y_3 \\ 1 & x_4 & y_4 \end{vmatrix}$$

$$\delta_3 = - \begin{vmatrix} 1 & x_1 & y_1 \\ 1 & x_2 & y_2 \\ 1 & x_4 & y_4 \end{vmatrix} \qquad \delta_4 = \begin{vmatrix} 1 & x_1 & y_1 \\ 1 & x_2 & y_2 \\ 1 & x_3 & y_3 \end{vmatrix}$$

The minimum potential energy with total Lagrangian formulation

The variational equation for the nonlinear elastic system can be written as:

$$a(u, \hat{u}) = l(\hat{u}) \tag{A.2}$$

Where, $a(u, \hat{u})$ is the energy form

$$a(u, \hat{u}) = \oint_{_0\Omega} \mathscr{S}(u) : \hat{\mathscr{E}}(u, \hat{u}) d\Omega \tag{A.3}$$

$l(\hat{u})$ is the load form

$$l(\hat{u}) = \oint_{_0\Omega} \hat{u}^T f^B d\Omega \tag{A.4}$$

The eq. (A.2) is the weak form of nonlinear hyperelastic systems, it is called the material description or the total Lagrangian formulation. Nonlinearity comes from the fact that the stress and strain implicitly depend on u.

A general nonlinear equation can be solved using a Newton-Raphson iterative method through a sequence of linearization.
The linearization of energy form can be written as:

$$L[a(u, \hat{u})] = \oint_{\Omega_0} [\Delta\mathscr{S} : \hat{\mathscr{E}} + \mathscr{S} : \Delta\hat{\mathscr{E}}] d\Omega \tag{A.5}$$

Where

$$\Delta\mathscr{S} = \frac{\partial\mathscr{S}}{\partial\mathscr{E}} : \Delta\mathscr{E} = \mathscr{D} : \Delta\mathscr{E} \tag{A.6}$$

eq. (A.5) becomes:

$$L[a(u, \hat{u})] = \oint_{\Omega_0} [\hat{\mathscr{E}} : \mathscr{D} : \Delta\mathscr{E} + \mathscr{S} : \Delta\hat{\mathscr{E}}] d\Omega \tag{A.7}$$

To facilitate calculations by dividing the linearized energy form eq.(A.7) into two parts:

$$A(u; \Delta u, \hat{u}) = \int\int_{\Omega_0} (\hat{\mathscr{E}} : \mathscr{D} : \Delta\mathscr{E}) d\Omega \qquad \textbf{\color{blue}{The first term}} \tag{A.8}$$

$$G(u; \Delta u, \hat{u}) = \oint_{\Omega_0} (\mathscr{S} : \Delta\hat{\mathscr{E}}) d\Omega \qquad \textbf{\color{blue}{The second term}} \tag{A.9}$$

The first term

The displacement gradient, variation and the increment of displacement gradient are defined as follows:

$$\nabla_0 u = \begin{bmatrix} \frac{\partial u_1}{\partial x_1} & \frac{\partial u_1}{\partial x_2} & \frac{\partial u_1}{\partial x_3} \\ \frac{\partial u_2}{\partial x_1} & \frac{\partial u_2}{\partial x_2} & \frac{\partial u_2}{\partial x_3} \\ \frac{\partial u_3}{\partial x_1} & \frac{\partial u_3}{\partial x_2} & \frac{\partial u_3}{\partial x_3} \end{bmatrix} \tag{A.10}$$

$$
\nabla_0 \hat{u} \quad = \begin{bmatrix} \frac{\partial \hat{u}_1}{\partial x_1} & \frac{\partial \hat{u}_1}{\partial x_2} & \frac{\partial \hat{u}_1}{\partial x_3} \\ \frac{\partial \hat{u}_2}{\partial x_1} & \frac{\partial \hat{u}_2}{\partial x_2} & \frac{\partial \hat{u}_2}{\partial x_3} \\ \frac{\partial \hat{u}_3}{\partial x_1} & \frac{\partial \hat{u}_3}{\partial x_2} & \frac{\partial \hat{u}_3}{\partial x_3} \end{bmatrix} \tag{A.11}
$$

$$
\nabla_0 \Delta u \quad = \begin{bmatrix} \frac{\partial \Delta u_1}{\partial x_1} & \frac{\partial \Delta u_1}{\partial x_2} & \frac{\partial \Delta u_1}{\partial x_3} \\ \frac{\partial \Delta u_2}{\partial x_1} & \frac{\partial \Delta u_2}{\partial x_2} & \frac{\partial \Delta u_2}{\partial x_3} \\ \frac{\partial \Delta u_3}{\partial x_1} & \frac{\partial \Delta u_3}{\partial x_2} & \frac{\partial \Delta u_3}{\partial x_3} \end{bmatrix} \tag{A.12}
$$

The variation of Lagrangian strain can be obtained as:

$$
\hat{\mathscr{E}}(u,\hat{u}) \quad = sym(\nabla_0 \hat{u}^T F) \tag{A.13}
$$

$$
\hat{\mathscr{E}}(u,\hat{u}) = sym\left(\begin{bmatrix} \frac{\partial \hat{u}_1}{\partial x_1} & \frac{\partial \hat{u}_2}{\partial x_1} & \frac{\partial \hat{u}_3}{\partial x_1} \\ \frac{\partial \hat{u}_1}{\partial x_2} & \frac{\partial \hat{u}_2}{\partial x_2} & \frac{\partial \hat{u}_3}{\partial x_2} \\ \frac{\partial \hat{u}_1}{\partial x_3} & \frac{\partial \hat{u}_2}{\partial x_3} & \frac{\partial \hat{u}_3}{\partial x_3} \end{bmatrix} \begin{bmatrix} F_{11} & F_{12} & F_{13} \\ F_{21} & F_{22} & F_{23} \\ F_{31} & F_{32} & F_{33} \end{bmatrix} \right) \tag{A.14}
$$

$$
\nabla_0 \hat{u}^T F = \begin{bmatrix} \hat{u}_{1,1}F_{11} + \hat{u}_{2,1}F_{21} + \hat{u}_{3,1}F_{31} & \hat{u}_{1,1}F_{12} + \hat{u}_{2,1}F_{22} + \hat{u}_{3,1}F_{32} & \hat{u}_{1,1}F_{13} + \hat{u}_{2,1}F_{23} + \hat{u}_{3,1}F_{33} \\ \hat{u}_{1,2}F_{11} + \hat{u}_{2,2}F_{21} + \hat{u}_{3,2}F_{31} & \hat{u}_{1,2}F_{12} + \hat{u}_{2,2}F_{22} + \hat{u}_{3,2}F_{32} & \hat{u}_{1,2}F_{13} + \hat{u}_{2,2}F_{23} + \hat{u}_{3,2}F_{33} \\ \hat{u}_{1,3}F_{11} + \hat{u}_{2,3}F_{21} + \hat{u}_{3,3}F_{31} & \hat{u}_{1,3}F_{12} + \hat{u}_{2,3}F_{22} + \hat{u}_{3,3}F_{32} & \hat{u}_{1,3}F_{13} + \hat{u}_{2,3}F_{23} + \hat{u}_{3,3}F_{33} \end{bmatrix} \tag{A.15}
$$

Then

$$
\hat{\mathscr{E}}(u,\hat{u}) = \begin{bmatrix} \hat{\mathscr{E}}(u,\hat{u})_{11} & \hat{\mathscr{E}}(u,\hat{u})_{12} & \hat{\mathscr{E}}(u,\hat{u})_{13} \\ \hat{\mathscr{E}}(u,\hat{u})_{12} & \hat{\mathscr{E}}(u,\hat{u})_{22} & \hat{\mathscr{E}}(u,\hat{u})_{23} \\ \hat{\mathscr{E}}(u,\hat{u})_{13} & \hat{\mathscr{E}}(u,\hat{u})_{23} & \hat{\mathscr{E}}(u,\hat{u})_{33} \end{bmatrix} \tag{A.16}
$$

Where

$$
\hat{\mathscr{E}}(u,\hat{u})_{11} \quad = \hat{u}_{1,1}F_{11} + \hat{u}_{2,1}F_{21} + \hat{u}_{3,1}F_{31} \tag{A.17}
$$

$$
\hat{\mathscr{E}}(u,\hat{u})_{22} \quad = \hat{u}_{1,2}F_{12} + \hat{u}_{2,2}F_{22} + \hat{u}_{3,2}F_{32} \tag{A.18}
$$

$$
\hat{\mathscr{E}}(u,\hat{u})_{33} \quad = \hat{u}_{1,3}F_{13} + \hat{u}_{2,3}F_{23} + \hat{u}_{3,3}F_{33} \tag{A.19}
$$

$$
\hat{\mathscr{E}}(u,\hat{u})_{12} \quad = \frac{1}{2}(\hat{u}_{1,1}F_{12} + \hat{u}_{2,1}F_{22} + \hat{u}_{3,1}F_{32} + \hat{u}_{1,2}F_{12} + \hat{u}_{2,2}F_{22} + \hat{u}_{3,2}F_{32}) \tag{A.20}
$$

$$
\hat{\mathscr{E}}(u,\hat{u})_{13} \quad = \frac{1}{2}(\hat{u}_{1,1}F_{13} + \hat{u}_{2,1}F_{23} + \hat{u}_{3,1}F_{33} + \hat{u}_{1,3}F_{11} + \hat{u}_{2,3}F_{21} + \hat{u}_{3,3}F_{31}) \tag{A.21}
$$

$$
\hat{\mathscr{E}}(u,\hat{u})_{23} \quad = \frac{1}{2}(\hat{u}_{1,2}F_{13} + \hat{u}_{2,2}F_{23} + \hat{u}_{3,2}F_{33} + \hat{u}_{1,3}F_{12} + \hat{u}_{2,3}F_{22} + \hat{u}_{3,3}F_{32}) \tag{A.22}
$$

using shape functions :

$$
\hat{u}_{i,j} \quad = \sum_{I=1}^{N_e} N_{I,j}\hat{d}_{Ii} \tag{A.23}
$$

$$\begin{cases}
\hat{u}_{1,1}F_{11} = N_{1,1}\hat{d}_{11}F_{11} + N_{2,1}\hat{d}_{21}F_{11} + N_{3,1}\hat{d}_{31}F_{11} + N_{4,1}\hat{d}_{41}F_{11} \\
\hat{u}_{1,2}F_{12} = N_{1,2}\hat{d}_{11}F_{12} + N_{2,2}\hat{d}_{21}F_{12} + N_{3,2}\hat{d}_{31}F_{12} + N_{4,2}\hat{d}_{41}F_{12} \\
\hat{u}_{1,3}F_{13} = N_{1,3}\hat{d}_{11}F_{13} + N_{2,3}\hat{d}_{21}F_{13} + N_{3,3}\hat{d}_{31}F_{13} + N_{4,3}\hat{d}_{41}F_{13} \\
\hat{u}_{2,1}F_{21} = N_{1,1}\hat{d}_{12}F_{21} + N_{2,1}\hat{d}_{22}F_{21} + N_{3,1}\hat{d}_{32}F_{21} + N_{4,1}\hat{d}_{42}F_{21} \\
\hat{u}_{2,2}F_{22} = N_{1,2}\hat{d}_{12}F_{22} + N_{2,2}\hat{d}_{22}F_{22} + N_{3,2}\hat{d}_{32}F_{22} + N_{4,2}\hat{d}_{42}F_{22} \\
\hat{u}_{2,3}F_{23} = N_{1,3}\hat{d}_{12}F_{23} + N_{2,3}\hat{d}_{22}F_{23} + N_{3,3}\hat{d}_{32}F_{23} + N_{4,3}\hat{d}_{42}F_{23} \\
\hat{u}_{3,1}F_{31} = N_{1,1}\hat{d}_{13}F_{31} + N_{2,1}\hat{d}_{23}F_{31} + N_{3,1}\hat{d}_{33}F_{31} + N_{4,1}\hat{d}_{43}F_{31} \\
\hat{u}_{3,2}F_{32} = N_{1,2}\hat{d}_{13}F_{32} + N_{2,2}\hat{d}_{23}F_{32} + N_{3,2}\hat{d}_{33}F_{32} + N_{4,2}\hat{d}_{43}F_{32} \\
\hat{u}_{3,3}F_{33} = N_{1,3}\hat{d}_{13}F_{33} + N_{2,3}\hat{d}_{23}F_{33} + N_{3,3}\hat{d}_{33}F_{33} + N_{4,3}\hat{d}_{43}F_{33}
\end{cases} \tag{A.24}$$

So, in the first term we have the nonlinear displacement-strain matrix defined as

$$\mathcal{B}_N = \left[\begin{array}{cccccccc}
N_{1,1}F_{11} & N_{1,1}F_{21} & N_{1,1}F_{31} & N_{2,1}F_{11} & N_{2,1}F_{21} & N_{2,1}F_{31} & \cdots \\
N_{1,2}F_{12} & N_{1,2}F_{22} & N_{1,2}F_{32} & N_{2,2}F_{12} & N_{2,2}F_{22} & N_{2,2}F_{32} & \cdots \\
N_{1,3}F_{13} & N_{1,3}F_{23} & N_{1,3}F_{33} & N_{2,3}F_{13} & N_{2,3}F_{23} & N_{2,3}F_{33} & \cdots \\
N_{1,2}F_{11}+N_{1,1}F_{12} & N_{1,2}F_{21}+N_{1,1}F_{22} & N_{1,2}F_{31}+N_{1,1}F_{32} & N_{2,2}F_{11}+N_{2,1}F_{12} & N_{2,2}F_{21}+N_{2,1}F_{22} & N_{2,2}F_{31}+N_{2,1}F_{32} & \cdots \\
N_{1,2}F_{13}+N_{1,3}F_{12} & N_{1,2}F_{23}+N_{1,3}F_{22} & N_{1,2}F_{33}+N_{1,3}F_{32} & N_{2,2}F_{13}+N_{2,3}F_{12} & N_{2,2}F_{23}+N_{2,3}F_{22} & N_{2,2}F_{33}+N_{2,3}F_{32} & \cdots \\
N_{1,1}F_{13}+N_{1,3}F_{11} & N_{1,1}F_{23}+N_{1,3}F_{21} & N_{1,1}F_{33}+N_{1,3}F_{31} & N_{2,1}F_{13}+N_{2,3}F_{11} & N_{2,1}F_{23}+N_{2,3}F_{21} & N_{2,1}F_{33}+N_{2,3}F_{31} & \cdots
\end{array}\right.$$

$$\left.\begin{array}{cccccc}
N_{3,1}F_{11} & N_{3,1}F_{21} & N_{3,1}F_{31} & N_{4,1}F_{11} & N_{4,1}F_{21} & N_{4,1}F_{31} \\
N_{3,2}F_{12} & N_{3,2}F_{22} & N_{3,2}F_{32} & N_{4,2}F_{12} & N_{4,2}F_{22} & N_{4,2}F_{32} \\
N_{3,3}F_{13} & N_{3,3}F_{23} & N_{3,3}F_{33} & N_{4,3}F_{13} & N_{4,3}F_{23} & N_{4,3}F_{33} \\
N_{3,2}F_{11}+N_{3,1}F_{12} & N_{3,2}F_{21}+N_{3,1}F_{22} & N_{3,2}F_{31}+N_{3,1}F_{32} & N_{4,2}F_{11}+N_{4,1}F_{12} & N_{4,2}F_{21}+N_{4,1}F_{22} & N_{4,2}F_{31}+N_{4,1}F_{32} \\
N_{3,2}F_{13}+N_{3,3}F_{12} & N_{3,2}F_{23}+N_{3,3}F_{22} & N_{3,2}F_{33}+N_{3,3}F_{32} & N_{4,2}F_{13}+N_{4,3}F_{12} & N_{4,2}F_{23}+N_{4,3}F_{22} & N_{4,2}F_{33}+N_{4,3}F_{32} \\
N_{3,1}F_{13}+N_{3,3}F_{11} & N_{3,1}F_{23}+N_{3,3}F_{21} & N_{3,1}F_{33}+N_{3,3}F_{31} & N_{4,1}F_{13}+N_{4,3}F_{11} & N_{4,1}F_{23}+N_{4,3}F_{21} & N_{4,1}F_{33}+N_{4,3}F_{31}
\end{array}\right] \tag{A.25}$$

Then

$$\mathcal{B}_N = \begin{bmatrix}
0 & 0 & 0 & 0 & 0 & 0 & -F_{11} & -F_{21} & -F_{31} & F_{11} & F_{21} & F_{31} \\
F_{12} & F_{22} & F_{32} & 0 & 0 & 0 & -F_{12} & -F_{22} & -F_{32} & 0 & 0 & 0 \\
0 & 0 & 0 & F_{13} & F_{23} & F_{33} & -F_{13} & -F_{23} & -F_{33} & 0 & 0 & 0 \\
F_{11} & F_{21} & F_{31} & 0 & 0 & 0 & (-F_{11}-F_{12}) & (-F_{21}-F_{22}) & (-F_{31}-F_{32}) & F_{12} & F_{22} & F_{32} \\
F_{13} & F_{23} & F_{33} & F_{12} & F_{22} & F_{32} & (-F_{13}-F_{12}) & (-F_{23}-F_{22}) & (-F_{33}-F_{32}) & 0 & 0 & 0 \\
0 & 0 & 0 & F_{11} & F_{21} & F_{31} & (-F_{13}-F_{11}) & (-F_{23}-F_{21}) & (-F_{33}-F_{31}) & F_{13} & F_{23} & F_{33}
\end{bmatrix}$$

The variation of nodal displacements is defined as:

$$\hat{d} = \begin{bmatrix} \hat{d}_{11} & \hat{d}_{12} & \hat{d}_{13} & \hat{d}_{21} & \hat{d}_{22} & \hat{d}_{23} & \hat{d}_{31} & \hat{d}_{32} & \hat{d}_{33} & \hat{d}_{41} & \hat{d}_{42} & \hat{d}_{43} \end{bmatrix}^T \tag{A.26}$$

So

$$\hat{\mathscr{E}} = \mathcal{B}_N \hat{d} \tag{A.27}$$

The increment of Lagrangian strain is defined as:

$$\Delta\mathscr{E}(u, \Delta u) = sym(\nabla_0 \Delta u^T F) \tag{A.28}$$

$$\Delta\mathscr{E}(u, \hat{u}) = \begin{bmatrix}
\Delta\mathscr{E}(u,\hat{u})_{11} & \Delta\mathscr{E}(u,\hat{u})_{12} & \Delta\mathscr{E}(u,\hat{u})_{13} \\
\Delta\mathscr{E}(u,\hat{u})_{12} & \Delta\mathscr{E}(u,\hat{u})_{22} & \Delta\mathscr{E}(u,\hat{u})_{23} \\
\Delta\mathscr{E}(u,\hat{u})_{13} & \Delta\mathscr{E}(u,\hat{u})_{23} & \Delta\mathscr{E}(u,\hat{u})_{33}
\end{bmatrix} \tag{A.29}$$

$$\Delta\mathscr{E}(u,\hat{u})_{11} = \Delta u_{1,1}F_{11} + \Delta u_{2,1}F_{21} + \Delta u_{3,1}F_{31} \tag{A.30}$$

$$\Delta\mathscr{E}(u,\hat{u})_{22} = \Delta u_{1,2}F_{12} + \Delta u_{2,2}F_{22} + \Delta u_{3,2}F_{32} \tag{A.31}$$

$$\Delta\mathscr{E}(u,\hat{u})_{33} = \Delta u_{1,3}F_{13} + \Delta u_{2,3}F_{23} + \Delta u_{3,3}F_{33} \tag{A.32}$$

$$\Delta\mathscr{E}(u,\hat{u})_{12} = \frac{1}{2}(\Delta u_{1,1}F_{12} + \Delta u_{2,1}F_{22} + \Delta u_{3,1}F_{32} + \Delta u_{1,2}F_{12} + \Delta u_{2,2}F_{22} + \Delta u_{3,2}F_{32}) \tag{A.33}$$

$$\Delta\mathscr{E}(u,\hat{u})_{13} = \frac{1}{2}(\Delta u_{1,1}F_{13} + \Delta u_{2,1}F_{23} + \Delta u_{3,1}F_{33} + \Delta u_{1,3}F_{11} + \Delta u_{2,3}F_{21} + \Delta u_{3,3}F_{31}) \tag{A.34}$$

$$\Delta\mathscr{E}(u,\hat{u})_{23} = \frac{1}{2}(\Delta u_{1,2}F_{13} + \Delta u_{2,2}F_{23} + \Delta u_{3,2}F_{33} + \Delta u_{1,3}F_{12} + \Delta u_{2,3}F_{22} + \Delta u_{3,3}F_{32}) \tag{A.35}$$

The incremental Lagrangian strain has a similar expression as:

$$\Delta \mathscr{E} = \mathcal{B}_N \Delta d \tag{A.36}$$

The constitutive relation is defined as:

$$\mathscr{S} = \mathscr{D} : \mathscr{E} = \lambda tr(\mathscr{E})\mathbf{I} + 2\mu\mathscr{E} \tag{A.37}$$

Where $\mathbf{I}$ is a $(3X3)$ identity tensor, and (λ,μ) are two Lame's constants.
So we can write using eq. (A.6)

$$\Delta \mathscr{S} = \mathscr{D} : \Delta \mathscr{E} = \lambda tr(\Delta \mathscr{E})\mathbf{I} + 2\mu\Delta\mathscr{E} \tag{A.38}$$

$$tr(\Delta\mathscr{E}) = \Delta u_{1,1}F_{11} + \Delta u_{2,1}F_{21} + \Delta u_{3,1}F_{31} + \Delta u_{1,2}F_{12} + \Delta u_{2,2}F_{22} + \Delta u_{3,2}F_{32} + \Delta u_{1,3}F_{13} + \Delta u_{2,3}F_{23} + \Delta u_{3,3}F_{33} \tag{A.39}$$

$$\Delta\mathscr{S} = \begin{bmatrix} \lambda tr(\Delta\mathscr{E}) & 0 & 0 \\ 0 & \lambda tr(\Delta\mathscr{E}) & 0 \\ 0 & 0 & \lambda tr(\Delta\mathscr{E}) \end{bmatrix} + \begin{bmatrix} 2\mu\Delta\mathscr{E}(u,\hat{u})_{11} & 2\mu\Delta\mathscr{E}(u,\hat{u})_{12} & 2\mu\Delta\mathscr{E}(u,\hat{u})_{13} \\ 2\mu\Delta\mathscr{E}(u,\hat{u})_{12} & 2\mu\Delta\mathscr{E}(u,\hat{u})_{22} & 2\mu\Delta\mathscr{E}(u,\hat{u})_{23} \\ 2\mu\Delta\mathscr{E}(u,\hat{u})_{13} & 2\mu\Delta\mathscr{E}(u,\hat{u})_{23} & 2\mu\Delta\mathscr{E}(u,\hat{u})_{33} \end{bmatrix} \tag{A.40}$$

$$\Delta\mathscr{S} = \begin{bmatrix} \Delta\mathscr{S}_{11} & \Delta\mathscr{S}_{12} & \Delta\mathscr{S}_{13} \\ \Delta\mathscr{S}_{12} & \Delta\mathscr{S}_{22} & \Delta\mathscr{S}_{23} \\ \Delta\mathscr{S}_{13} & \Delta\mathscr{S}_{23} & \Delta\mathscr{S}_{33} \end{bmatrix} \tag{A.41}$$

$$\Delta\mathscr{S}_{11} = \lambda(\Delta u_{1,2}F_{12} + \Delta u_{2,2}F_{22} + \Delta u_{3,2}F_{32} + \Delta u_{1,3}F_{13} + \Delta u_{2,3}F_{23} + \Delta u_{3,3}F_{33}) + (\lambda + 2\mu)(\Delta u_{1,1}F_{11} + \Delta u_{2,1}F_{21} + \Delta u_{3,1}F_{31})$$

$$\Delta\mathscr{S}_{22} = \lambda(\Delta u_{1,1}F_{11} + \Delta u_{2,1}F_{21} + \Delta u_{3,1}F_{31} + \Delta u_{1,3}F_{13} + \Delta u_{2,3}F_{23} + \Delta u_{3,3}F_{33}) + (\lambda + 2\mu)(\Delta u_{1,2}F_{12} + \Delta u_{2,2}F_{22} + \Delta u_{3,2}F_{32})$$

$$\Delta\mathscr{S}_{33} = \lambda(\Delta u_{1,1}F_{11} + \Delta u_{2,1}F_{21} + \Delta u_{3,1}F_{31} + \Delta u_{1,2}F_{12} + \Delta u_{2,2}F_{22} + \Delta u_{3,2}F_{32}) + (\lambda + 2\mu)(\Delta u_{1,3}F_{13} + \Delta u_{2,3}F_{23} + \Delta u_{3,3}F_{33})$$

$$\Delta\mathscr{S}_{12} = \mu(\Delta u_{1,1}F_{12} + \Delta u_{2,1}F_{22} + \Delta u_{3,1}F_{32} + \Delta u_{1,2}F_{12} + \Delta u_{2,2}F_{22} + \Delta u_{3,2}F_{32})$$

$$\Delta\mathscr{S}_{13} = \mu(\Delta u_{1,1}F_{13} + \Delta u_{2,1}F_{23} + \Delta u_{3,1}F_{33} + \Delta u_{1,3}F_{11} + \Delta u_{2,3}F_{21} + \Delta u_{3,3}F_{31})$$

$$\Delta\mathscr{S}_{23} = \mu(\Delta u_{1,2}F_{13} + \Delta u_{2,2}F_{23} + \Delta u_{3,2}F_{33} + \Delta u_{1,3}F_{12} + \Delta u_{2,3}F_{22} + \Delta u_{3,3}F_{32})$$

Then

$$\hat{\mathscr{E}} : \mathscr{D} : \Delta\mathscr{E} = \hat{\mathscr{E}}(u,\hat{u})_{11}\Delta\mathscr{S}_{11} + \hat{\mathscr{E}}(u,\hat{u})_{22}\Delta\mathscr{S}_{22} + \hat{\mathscr{E}}(u,\hat{u})_{33}\Delta\mathscr{S}_{33} + 2\hat{\mathscr{E}}(u,\hat{u})_{12}\Delta\mathscr{S}_{12} + 2\hat{\mathscr{E}}(u,\hat{u})_{13}\Delta\mathscr{S}_{13} + 2\hat{\mathscr{E}}(u,\hat{u})_{23}\Delta\mathscr{S}_{23} \tag{A.42}$$

So

$$\hat{\mathscr{E}} : \mathscr{D} : \Delta\mathscr{E} = \begin{bmatrix} (\hat{u}_{1,1}F_{11} + \hat{u}_{2,1}F_{21} + \hat{u}_{3,1}F_{31}) \\ (\hat{u}_{1,2}F_{12} + \hat{u}_{2,2}F_{22} + \hat{u}_{3,2}F_{32}) \\ (\hat{u}_{1,3}F_{13} + \hat{u}_{2,3}F_{23} + \hat{u}_{3,3}F_{33}) \\ (\hat{u}_{1,1}F_{12} + \hat{u}_{2,1}F_{22} + \hat{u}_{3,1}F_{32} + \hat{u}_{1,2}F_{12} + \hat{u}_{2,2}F_{22} + \hat{u}_{3,2}F_{32}) \\ (\hat{u}_{1,1}F_{13} + \hat{u}_{2,1}F_{23} + \hat{u}_{3,1}F_{33} + \hat{u}_{1,3}F_{11} + \hat{u}_{2,3}F_{21} + \hat{u}_{3,3}F_{31}) \\ (\hat{u}_{1,2}F_{13} + \hat{u}_{2,2}F_{23} + \hat{u}_{3,2}F_{33} + \hat{u}_{1,3}F_{12} + \hat{u}_{2,3}F_{22} + \hat{u}_{3,3}F_{32}) \end{bmatrix}^T \mathscr{D}$$
$$\begin{bmatrix} (\Delta u_{1,1}F_{11} + \Delta u_{2,1}F_{21} + \Delta u_{3,1}F_{31}) \\ (\Delta u_{1,2}F_{12} + \Delta u_{2,2}F_{22} + \Delta u_{3,2}F_{32}) \\ (\Delta u_{1,3}F_{13} + \Delta u_{2,3}F_{23} + \Delta u_{3,3}F_{33}) \\ (\Delta u_{1,1}F_{12} + \Delta u_{2,1}F_{22} + \Delta u_{3,1}F_{32} + \Delta u_{1,2}F_{12} + \Delta u_{2,2}F_{22} + \Delta u_{3,2}F_{32}) \\ (\Delta u_{1,1}F_{13} + \Delta u_{2,1}F_{23} + \Delta u_{3,1}F_{33} + \Delta u_{1,3}F_{11} + \Delta u_{2,3}F_{21} + \Delta u_{3,3}F_{31}) \\ (\Delta u_{1,2}F_{13} + \Delta u_{2,2}F_{23} + \Delta u_{3,2}F_{33} + \Delta u_{1,3}F_{12} + \Delta u_{2,3}F_{22} + \Delta u_{3,3}F_{32}) \end{bmatrix} \tag{A.43}$$

Where

$$\mathscr{D} = \begin{bmatrix} (\lambda + 2\mu) & \lambda & \lambda & 0 & 0 & 0 \\ \lambda & (\lambda + 2\mu) & \lambda & 0 & 0 & 0 \\ \lambda & \lambda & (\lambda + 2\mu) & 0 & 0 & 0 \\ 0 & 0 & 0 & \mu & 0 & 0 \\ 0 & 0 & 0 & 0 & \mu & 0 \\ 0 & 0 & 0 & 0 & 0 & \mu \end{bmatrix} \tag{A.44}$$

Finally

$$\hat{\mathscr{E}} : \mathscr{D} : \Delta\mathscr{E} = \tilde{d}^T \mathcal{B}_N^T \mathscr{D} \mathcal{B}_N \Delta d \tag{A.45}$$

The first term in the structural energy form:

$$\int\int_{\Omega_0} \hat{\mathscr{E}} : \mathscr{D} : \Delta\mathscr{E} d\Omega = \tilde{d}^T \left(\int\int_{\Omega_0} \mathcal{B}_N^T D \mathcal{B}_N d\Omega\right) \Delta d \tag{A.46}$$

The second term

The variation of the increment of Lagrangian strain can be obtained as

$$\Delta\hat{\mathscr{E}}(\Delta u, \hat{u}) \quad = sym(\nabla_0 \hat{u}^T \nabla_0 \Delta u) \tag{A.47}$$

$$\Delta\hat{\mathscr{E}}(\Delta u, \hat{u}) = sym\left(\begin{bmatrix} \hat{u}_{1,1}\Delta u_{1,1} + \hat{u}_{2,1}\Delta u_{2,1} + \hat{u}_{3,1}\Delta u_{3,1} & \hat{u}_{1,1}\Delta u_{1,2} + \hat{u}_{2,1}\Delta u_{2,2} + \hat{u}_{3,1}\Delta u_{3,2} & \hat{u}_{1,1}\Delta u_{1,3} + \hat{u}_{2,1}\Delta u_{2,3} + \hat{u}_{3,1}\Delta u_{3,3} \\ \hat{u}_{1,2}\Delta u_{1,1} + \hat{u}_{2,2}\Delta u_{2,1} + \hat{u}_{3,2}\Delta u_{3,1} & \hat{u}_{1,2}\Delta u_{1,2} + \hat{u}_{2,2}\Delta u_{2,2} + \hat{u}_{3,2}\Delta u_{3,2} & \hat{u}_{1,2}\Delta u_{1,3} + \hat{u}_{2,2}\Delta u_{2,3} + \hat{u}_{3,2}\Delta u_{3,3} \\ \hat{u}_{1,3}\Delta u_{1,1} + \hat{u}_{2,3}\Delta u_{2,1} + \hat{u}_{3,3}\Delta u_{3,1} & \hat{u}_{1,3}\Delta u_{1,2} + \hat{u}_{2,3}\Delta u_{2,2} + \hat{u}_{3,3}\Delta u_{3,2} & \hat{u}_{1,3}\Delta u_{1,3} + \hat{u}_{2,3}\Delta u_{2,3} + \hat{u}_{3,3}\Delta u_{3,3} \end{bmatrix}\right) \tag{A.48}$$

$$\Delta\hat{\mathscr{E}}(\Delta u, \hat{u}) = \begin{bmatrix} \Delta\hat{\mathscr{E}}(\Delta u, \hat{u})_{11} & \Delta\hat{\mathscr{E}}(\Delta u, \hat{u})_{12} & \Delta\hat{\mathscr{E}}(\Delta u, \hat{u})_{13} \\ \Delta\hat{\mathscr{E}}(\Delta u, \hat{u})_{12} & \Delta\hat{\mathscr{E}}(\Delta u, \hat{u})_{22} & \Delta\hat{\mathscr{E}}(\Delta u, \hat{u})_{23} \\ \Delta\hat{\mathscr{E}}(\Delta u, \hat{u})_{13} & \Delta\hat{\mathscr{E}}(\Delta u, \hat{u})_{23} & \Delta\hat{\mathscr{E}}(\Delta u, \hat{u})_{33} \end{bmatrix} \tag{A.49}$$

$$\Delta\hat{\mathscr{E}}(\Delta u, \hat{u})_{11} \quad = \hat{u}_{1,1}\Delta u_{1,1} + \hat{u}_{2,1}\Delta u_{2,1} + \hat{u}_{3,1}\Delta u_{3,1} \tag{A.50}$$

$$\Delta\hat{\mathscr{E}}(\Delta u, \hat{u})_{22} \quad = \hat{u}_{1,2}\Delta u_{1,2} + \hat{u}_{2,2}\Delta u_{2,2} + \hat{u}_{3,2}\Delta u_{3,2} \tag{A.51}$$

$$\Delta\hat{\mathscr{E}}(\Delta u, \hat{u})_{33} \quad = \hat{u}_{1,3}\Delta u_{1,3} + \hat{u}_{2,3}\Delta u_{2,3} + \hat{u}_{3,3}\Delta u_{3,3} \tag{A.52}$$

$$\Delta\hat{\mathscr{E}}(\Delta u, \hat{u})_{12} \quad = \frac{1}{2}[\hat{u}_{1,1}\Delta u_{1,2} + \hat{u}_{2,1}\Delta u_{2,2} + \hat{u}_{3,1}\Delta u_{3,2} + \hat{u}_{1,2}\Delta u_{1,1} + \hat{u}_{2,2}\Delta u_{2,1} + \hat{u}_{3,2}\Delta u_{3,1}] \tag{A.53}$$

$$\Delta\hat{\mathscr{E}}(\Delta u, \hat{u})_{13} \quad = \frac{1}{2}[\hat{u}_{1,1}\Delta u_{1,3} + \hat{u}_{2,1}\Delta u_{2,3} + \hat{u}_{3,1}\Delta u_{3,3} + \hat{u}_{1,3}\Delta u_{1,1} + \hat{u}_{2,3}\Delta u_{2,1} + \hat{u}_{3,3}\Delta u_{3,1}] \tag{A.54}$$

$$\Delta\hat{\mathscr{E}}(\Delta u, \hat{u})_{23} \quad = \frac{1}{2}[\hat{u}_{1,2}\Delta u_{1,3} + \hat{u}_{2,2}\Delta u_{2,3} + \hat{u}_{3,2}\Delta u_{3,3} + \hat{u}_{1,3}\Delta u_{1,2} + \hat{u}_{2,3}\Delta u_{2,2} + \hat{u}_{3,3}\Delta u_{3,2}] \tag{A.55}$$

Using shape functions we obtain :

$$\hat{u}_{i,j} = \begin{bmatrix} N_{1,1} & 0 & 0 & N_{2,1} & 0 & 0 & N_{3,1} & 0 & 0 & N_{4,1} & 0 & 0 \\ N_{1,2} & 0 & 0 & N_{2,2} & 0 & 0 & N_{3,2} & 0 & 0 & N_{4,2} & 0 & 0 \\ N_{1,3} & 0 & 0 & N_{2,3} & 0 & 0 & N_{3,3} & 0 & 0 & N_{4,3} & 0 & 0 \\ 0 & N_{1,1} & 0 & 0 & N_{2,1} & 0 & 0 & N_{3,1} & 0 & 0 & N_{4,1} & 0 \\ 0 & N_{1,2} & 0 & 0 & N_{2,2} & 0 & 0 & N_{3,2} & 0 & 0 & N_{4,2} & 0 \\ 0 & N_{1,3} & 0 & 0 & N_{2,3} & 0 & 0 & N_{3,3} & 0 & 0 & N_{4,3} & 0 \\ 0 & 0 & N_{1,1} & 0 & 0 & N_{2,1} & 0 & 0 & N_{3,1} & 0 & 0 & N_{4,1} \\ 0 & 0 & N_{1,2} & 0 & 0 & N_{2,2} & 0 & 0 & N_{3,2} & 0 & 0 & N_{4,2} \\ 0 & 0 & N_{1,3} & 0 & 0 & N_{2,3} & 0 & 0 & N_{3,3} & 0 & 0 & N_{4,3} \end{bmatrix} \begin{bmatrix} \hat{d}_{11} \\ \hat{d}_{12} \\ \hat{d}_{13} \\ \hat{d}_{21} \\ \hat{d}_{22} \\ \hat{d}_{23} \\ \hat{d}_{31} \\ \hat{d}_{32} \\ \hat{d}_{33} \\ \hat{d}_{41} \\ \hat{d}_{42} \\ \hat{d}_{43} \end{bmatrix} \tag{A.56}$$

$$\Delta u_{i,j} = \mathcal{B}_G \begin{bmatrix} \Delta d_{11} & \Delta d_{12} & \Delta d_{13} & \Delta d_{21} & \Delta d_{22} & \Delta d_{23} & \Delta d_{31} & \Delta d_{32} & \Delta d_{33} & \Delta d_{41} & \Delta d_{42} & \Delta d_{43} \end{bmatrix}^T \tag{A.57}$$

So, the nonlinear displacement-strain matrix is defined as :

$$\mathcal{B}_G = \begin{bmatrix} 0 & 0 & 0 & 0 & 0 & 0 & -1 & 0 & 0 & 1 & 0 & 0 \\ 1 & 0 & 0 & 0 & 0 & 0 & -1 & 0 & 0 & 0 & 0 & 0 \\ 0 & 0 & 0 & 1 & 0 & 0 & -1 & 0 & 0 & 0 & 0 & 0 \\ 0 & 0 & 0 & 0 & 0 & 0 & 0 & -1 & 0 & 0 & 1 & 0 \\ 0 & 1 & 0 & 0 & 0 & 0 & 0 & -1 & 0 & 0 & 0 & 0 \\ 0 & 0 & 0 & 0 & 1 & 0 & 0 & -1 & 0 & 0 & 0 & 0 \\ 0 & 0 & 0 & 0 & 0 & 0 & 0 & 0 & -1 & 0 & 0 & 1 \\ 0 & 0 & 1 & 0 & 0 & 0 & 0 & 0 & -1 & 0 & 0 & 0 \\ 0 & 0 & 0 & 0 & 0 & 1 & 0 & 0 & -1 & 0 & 0 & 0 \end{bmatrix} \tag{A.58}$$

The second term becomes

$$\mathscr{S} : \Delta\hat{\mathscr{E}} = \mathscr{S}_{11}\Delta\hat{\mathscr{E}}_{1,1} + \mathscr{S}_{22}\Delta\hat{\mathscr{E}}_{22} + \mathscr{S}_{33}\Delta\hat{\mathscr{E}}_{33} + 2\mathscr{S}_{12}\Delta\hat{\mathscr{E}}_{12} + 2\mathscr{S}_{13}\Delta\hat{\mathscr{E}}_{13} + 2\mathscr{S}_{23}\Delta\hat{\mathscr{E}}_{23} \tag{A.59}$$

Where

$$\mathscr{S} : \Delta\hat{\mathscr{E}} = \begin{bmatrix} \hat{u}_{1,1} \\ \hat{u}_{1,2} \\ \hat{u}_{1,3} \\ \hat{u}_{2,1} \\ \hat{u}_{2,2} \\ \hat{u}_{2,3} \\ \hat{u}_{3,1} \\ \hat{u}_{3,2} \\ \hat{u}_{3,3} \end{bmatrix}^T \begin{bmatrix} \mathscr{S}_{11} & \mathscr{S}_{12} & \mathscr{S}_{13} & 0 & 0 & 0 & 0 & 0 & 0 \\ \mathscr{S}_{12} & \mathscr{S}_{22} & \mathscr{S}_{23} & 0 & 0 & 0 & 0 & 0 & 0 \\ \mathscr{S}_{13} & \mathscr{S}_{23} & \mathscr{S}_{33} & 0 & 0 & 0 & 0 & 0 & 0 \\ 0 & 0 & 0 & \mathscr{S}_{11} & \mathscr{S}_{12} & \mathscr{S}_{13} & 0 & 0 & 0 \\ 0 & 0 & 0 & \mathscr{S}_{12} & \mathscr{S}_{22} & \mathscr{S}_{23} & 0 & 0 & 0 \\ 0 & 0 & 0 & \mathscr{S}_{13} & \mathscr{S}_{23} & \mathscr{S}_{33} & 0 & 0 & 0 \\ 0 & 0 & 0 & 0 & 0 & 0 & \mathscr{S}_{11} & \mathscr{S}_{12} & \mathscr{S}_{13} \\ 0 & 0 & 0 & 0 & 0 & 0 & \mathscr{S}_{12} & \mathscr{S}_{22} & \mathscr{S}_{23} \\ 0 & 0 & 0 & 0 & 0 & 0 & \mathscr{S}_{13} & \mathscr{S}_{23} & \mathscr{S}_{33} \end{bmatrix} \begin{bmatrix} \Delta u_{1,1} \\ \Delta u_{1,2} \\ \Delta u_{1,3} \\ \Delta u_{2,1} \\ \Delta u_{2,2} \\ \Delta u_{2,3} \\ \Delta u_{3,1} \\ \Delta u_{3,2} \\ \Delta u_{3,3} \end{bmatrix} \tag{A.60}$$

So

$$\mathscr{S} : \Delta\hat{\mathscr{E}} = \tilde{d}^T \mathcal{B}_G^T \Sigma \mathcal{B}_G \Delta d \tag{A.61}$$

Where

$$\Sigma = \begin{bmatrix} \mathscr{S}_{11} & \mathscr{S}_{12} & \mathscr{S}_{13} & 0 & 0 & 0 & 0 & 0 & 0 \\ \mathscr{S}_{12} & \mathscr{S}_{22} & \mathscr{S}_{23} & 0 & 0 & 0 & 0 & 0 & 0 \\ \mathscr{S}_{13} & \mathscr{S}_{23} & \mathscr{S}_{33} & 0 & 0 & 0 & 0 & 0 & 0 \\ 0 & 0 & 0 & \mathscr{S}_{11} & \mathscr{S}_{12} & \mathscr{S}_{13} & 0 & 0 & 0 \\ 0 & 0 & 0 & \mathscr{S}_{12} & \mathscr{S}_{22} & \mathscr{S}_{23} & 0 & 0 & 0 \\ 0 & 0 & 0 & \mathscr{S}_{13} & \mathscr{S}_{23} & \mathscr{S}_{33} & 0 & 0 & 0 \\ 0 & 0 & 0 & 0 & 0 & 0 & \mathscr{S}_{11} & \mathscr{S}_{12} & \mathscr{S}_{13} \\ 0 & 0 & 0 & 0 & 0 & 0 & \mathscr{S}_{12} & \mathscr{S}_{22} & \mathscr{S}_{23} \\ 0 & 0 & 0 & 0 & 0 & 0 & \mathscr{S}_{13} & \mathscr{S}_{23} & \mathscr{S}_{33} \end{bmatrix} \tag{A.62}$$

The second term of the linearized energy form can be written as:

$$\iint_{\Omega_0} \mathscr{S} : \Delta\hat{\mathscr{E}} d\Omega = \tilde{d}^T \left(\iint_{\Omega_0} \mathcal{B}_G^T \Sigma \mathcal{B}_G d\Omega \right) \Delta d \tag{A.63}$$

Experiment results of substiffness matrix initialized with linear deformation

In this experience and for the two meshes A, B with deformed part of $\frac{|\Omega^\star|}{|\Omega_0|} = 10\%$, we chose a range of values for the two constants of assumptions 1 and 2. Where, We varied $\mathbf{c}_1$ from 10^{-2} to 50 with 200 steps

and $\mathbf{c}_2$ is varied from 10^{-5} to 10^{-3}. For assumption 3 we fix the control constant at $\mathbf{c}_3 = 2$. The figures A.1 and A.2, show the values of the products $\gamma\eta$ and $\alpha\beta$. We use the logarithm with the base 10 to display these values. We can see that the three constants chosen satisfy the conditions of proposition 2.2. Figure A.3 and A.4 shows the radius of convergence for the compared methods. We can say that for mesh A the radius of convergence of the proposed method is more better than the classical method. Mesh B shows the opposite that the mesh A where the classic method is better than our method.
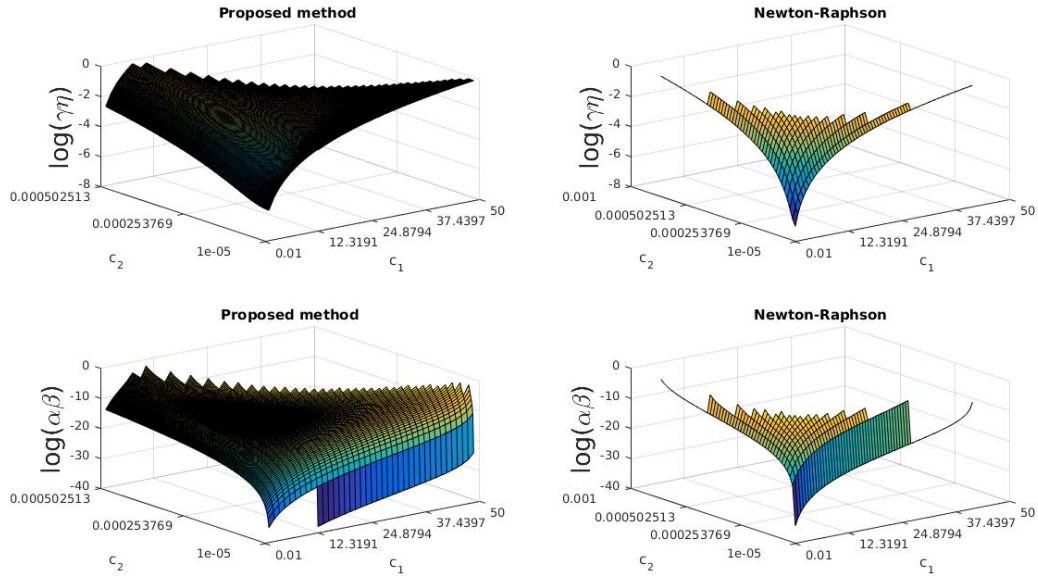

Figure A.1: The conditions $\gamma\eta < 1$ and $\alpha\beta \leq \frac{1}{2}$ of mesh A with $\frac{|\Omega^\star|}{|\Omega_0|} = 10\%$
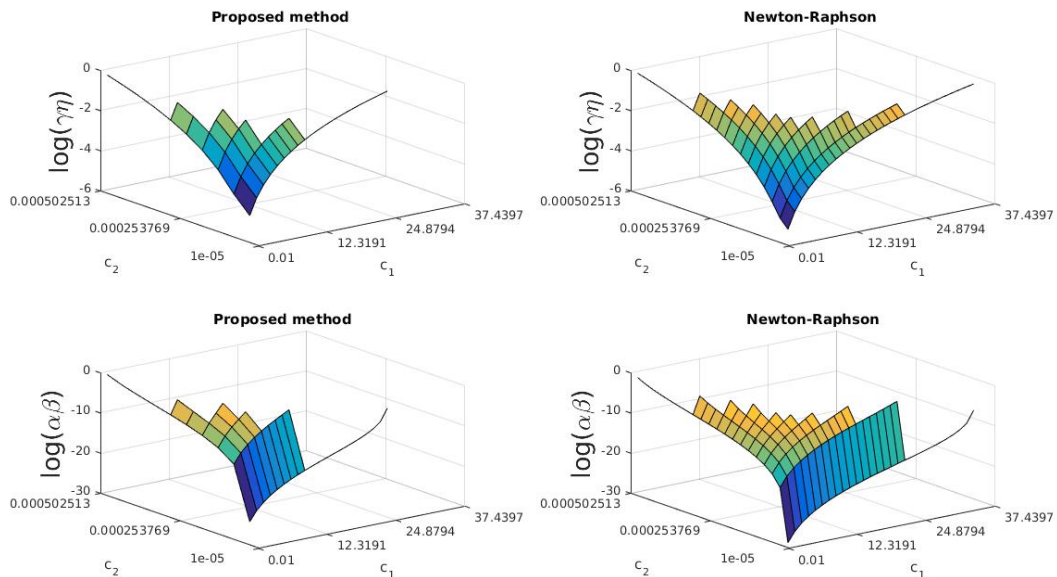

Figure A.2: The conditions $\gamma\eta < 1$ and $\alpha\beta \leq \frac{1}{2}$ of mesh B with $\frac{|\Omega^\star|}{|\Omega_0|} = 10\%$
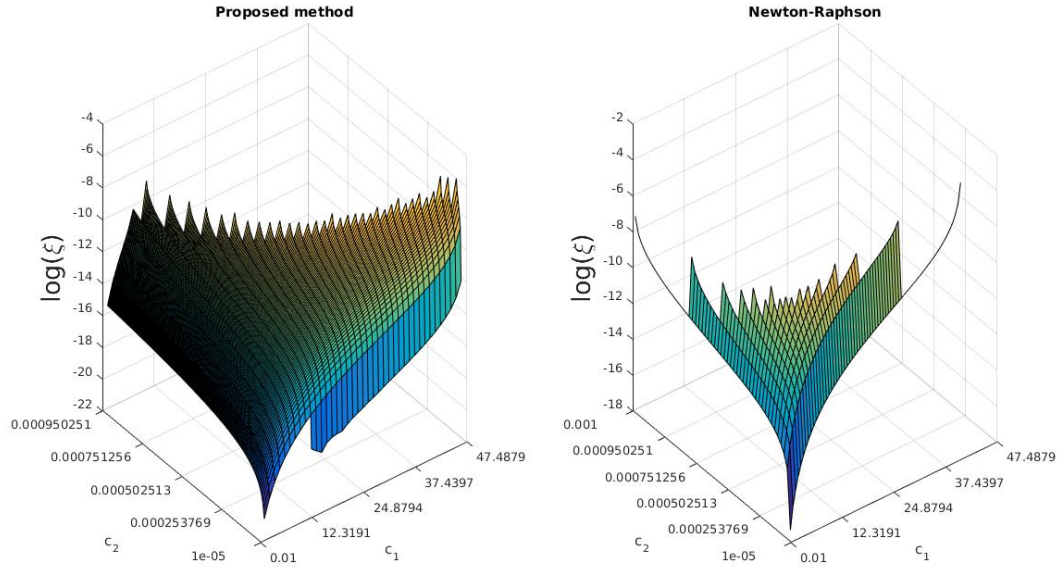
Figure A.3: The radius of convergence of mesh A with $\frac{|\Omega^\star|}{|\Omega_0|} = 10\%$
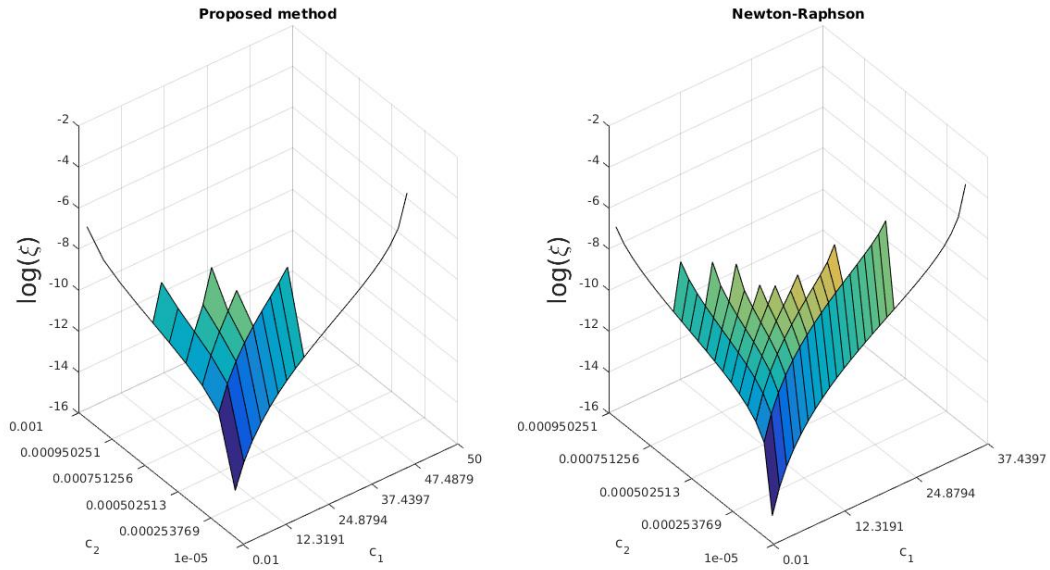

Figure A.4: The radius of convergence of mesh B with $\frac{|\Omega^\star|}{|\Omega_0|} = 10\%$

A comparative study with other constitutive models

In the experiment of a comparative study with Neo-Hookean, Saint Venant-Kirchhoff and Mooney-Rivlin models. Saint Venant-Kirchhoff model for large displacement lost the convergence so we study the radius of convergence for two remaining models. So, for the mesh A with deformed part of $\frac{|\Omega^\star|}{|\Omega_0|} = 10\%$, we

chose a range of values for the two constants of assumptions 1 and 2. Where, We varied $\mathbf{c}_1$ from 10^{-2} to 50 with 200 steps and $\mathbf{c}_2$ is varied from 10^{-6} to 10^{-4}. For assumption 3 we fix the control constant at $\mathbf{c}_3 = 2$. The figures A.5 and A.6, show the values of the products $\gamma\eta$ and $\alpha\beta$. We use the logarithm with the base 10 to display these values. We can see that the three constants chosen satisfy the conditions of proposition 2.2. Figure A.7 and A.8 shows the radius of convergence for our and Newton-Raphson method with Neo-Hookean and Mooney-Rivlin models. We can say that the radius of convergence of the proposed for the two models is similar to the classical Newton-Raphson method.
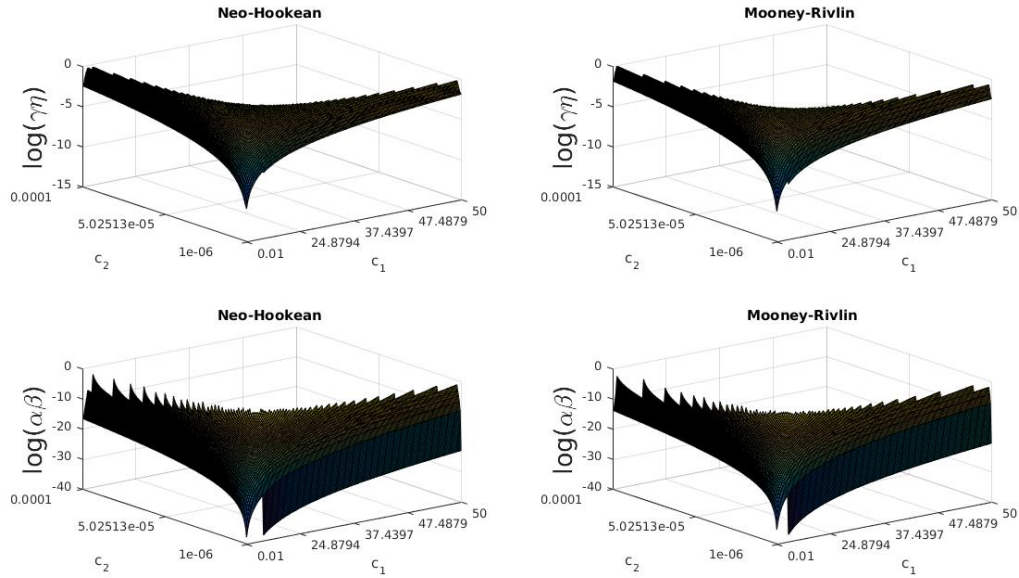

Figure A.5: The conditions $\gamma\eta < 1$ and $\alpha\beta \leq \frac{1}{2}$ of mesh A with classic method
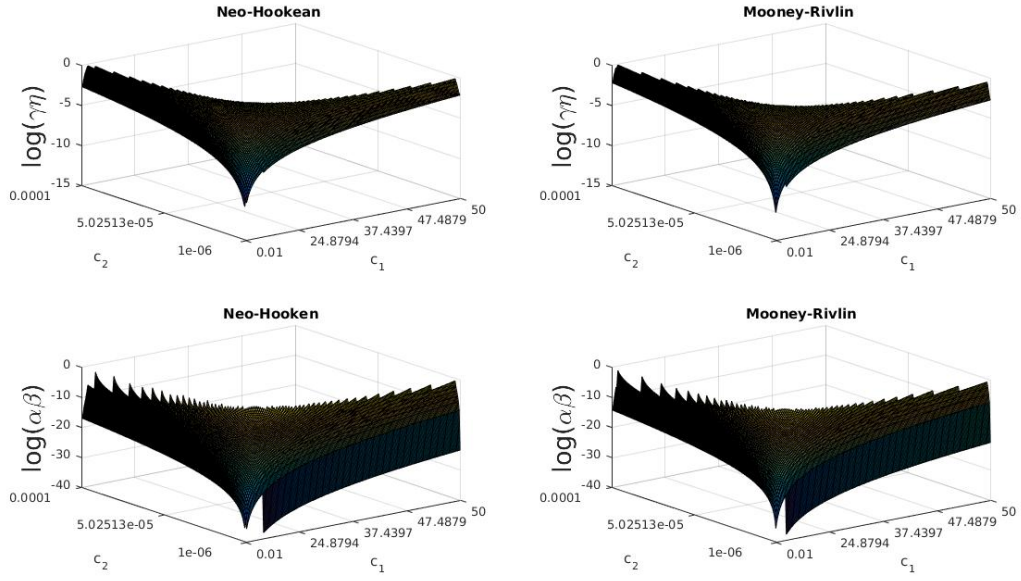
Figure A.6: The conditions $\gamma\eta < 1$ and $\alpha\beta \leq \frac{1}{2}$ of mesh A with the proposed method
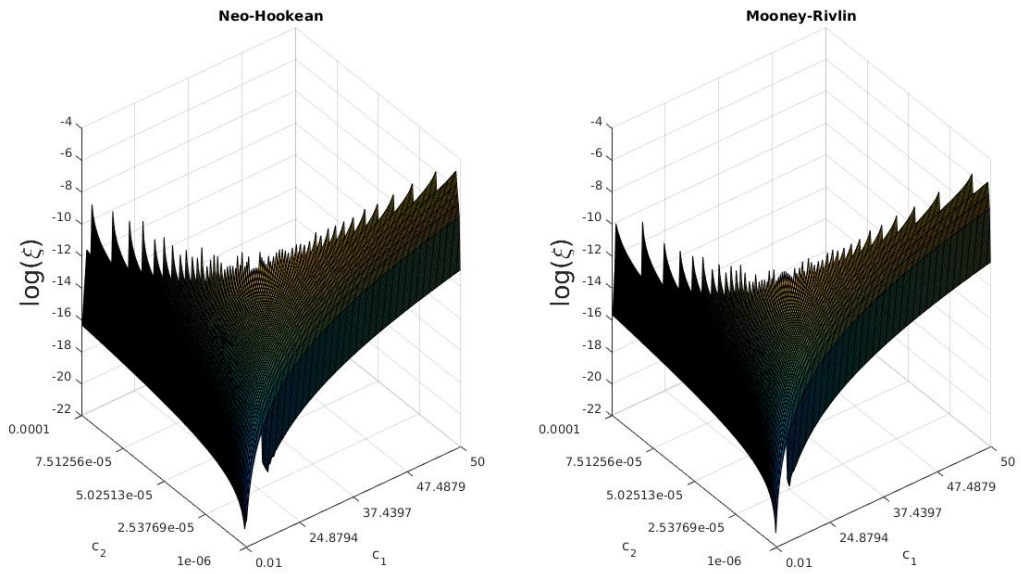

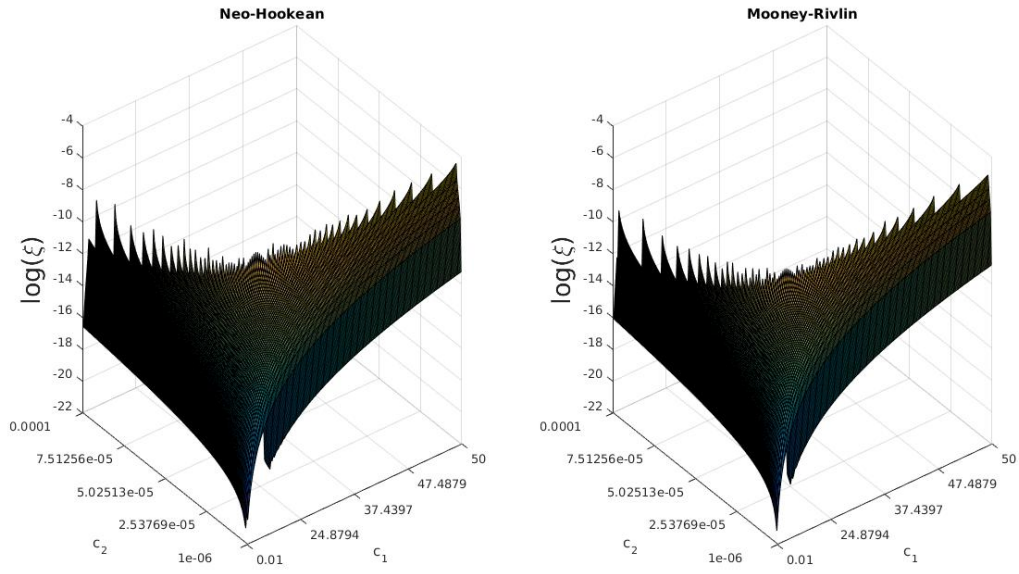Figure A.7: The radius of convergence of mesh A with the classic method

Figure A.8: The radius of convergence of mesh A with the proposed method

Bibliography

[1] Robert A. Adams and John J. F. Fournier. *Sobolev Spaces*, volume 140. Academic Press, 2003.

[2] Jean-Sébastien Affagard. *Identification des propriétés hyperélastiques des muscles de la cuisse à l'état passif : couplage des techniques de corrélation d'images aux techniques d'imagerie médicale.* Phd thesis, Université de Technologie de Compiègne, October 2013.

[3] Kendall Atkinson, Weimin Han, and David E Stewart. *Numerical solution of ordinary differential equations*, volume 108. John Wiley & Sons, 2011.

[4] Long Bai, Jianxing Yang, Xiaohong Chen, Pei Jiang, Fuqiang Liu, Fan Zheng, and Yuanxi Sun. Solving the time-varying inverse kinematics problem for the da vinci surgical robot. *Applied Sciences*, 9(3):546, 2019.

[5] Carlo Banditori, Paola Cappanera, and Filippo Visintin. A combined optimization?simulation approach to the master surgical scheduling problem. *IMA Journal of Management Mathematics*, 24(2):155–187, 2013.

[6] T. Beda. Modeling hyperelastic behavior of rubber: A novel invariant-based and a review of constitutive models. *Journal of Polymer Science Part B: Polymer Physics*, 45(13):1713–1732, 2007.

[7] Mohamed Bader Boubaker. *Contribution mécanique à la réduction des marges en radiothérapie de la prostate : modélisation et simulation numérique du mouvement et de la déformation des organes pelviens.* PhD thesis, Lorraine Université, 2009.

[8] Susanne Brenner and Ridgway Scott. *The Mathematical Theory of Finite Element Methods.* Texts in Applied Mathematics. Springer-Verlag, New York, 3 edition, 2008.

[9] Haim Brezis. *Functional Analysis, Sobolev Spaces and Partial Differential Equations.* Universitext. Springer-Verlag, New York, 2011.

[10] Aline Brunon. *Caractérisation et modélisation de la rupture des tissus hépatiques.* Phd thesis, INSA de Lyon, 2011.

[11] M. Cervera, M. Chiumenti, and R. Codina. Mixed stabilized finite element methods in nonlinear solid mechanics: Part ii: Strain localization. *Computer Methods in Applied Mechanics and Engineering*, 199(37):2571–2589, 2010.

[12] Matthieu Chabanas, Yohan Payan, Christophe Marecaux, Pascal Swider, and Franck Boutault. Comparison of linear and non-linear soft tissue models with post-operative ct scan in maxillofacial surgery. *Lecture Notes in Computer Science*, 3078:19–27, 2004.

[13] Grégory Chagnon, Jacques Ohayon, Jean-Louis Martiel, and Denis Favier. Chapter 1 - hyperelasticity modeling for incompressible passive biological tissues. In *Biomechanics of Living Organs*, volume 1, pages 3–30. 2017.

[14] Dominique Chamoret, Sébastien Roth, Samuel Gomes, François Peyraut, Xiu-Tian Yan, and Zhi-Qiang Feng. Création d'un modèle éléments finis 3d non-linéaire d'une main en contact. *CSMA*, 2011.

[15] Alaa Chateauneuf. La méthode des éléments finis-calcul non-linéaire géométrique. *Techniques de l'ingénieur Méthodes de calcul et conception*, base documentaire :825.(ref. article : c6003), 2016.

[16] Zhuo-Wei Chen and François Goulette. Fast computation of soft tissue deformations for real-time medical training simulators: The HEML method and open-source software. In *Proceedings of the 2016 Virtual Reality International Conference*, VRIC '16, pages 1:1–1:2. ACM. event-place: Laval, France.

[17] Safwan Chendeb. *Chirurgie virtuelle : modélisation temps réel des tissus mous, interactions et système haptique dédié*. Phd thesis, École Nationale Supérieure des Mines de Paris, December 2007.

[18] Cécile Conte. *Comportement mécanique du foie en contexte traumatique : rupture et endommagement des tissus*. Phd thesis, Aix-Marseille Université, 2012.

[19] Hadrien Courtecuisse, Jérémie Allard, Pierre Kerfriden, Stéphane P.A. Bordas, Stéphane Cotin, and Christian Duriez. Real-time simulation of contact and cutting of heterogeneous soft-tissues. *Medical Image Analysis*, 18(2):394–410, 2014.

[20] Maryam Mehdizadeh Dastjerdi, Ali Fallah, and Saeid Rashidi. An iterative method for estimating nonlinear elastic constants of tumor in soft tissue from approximate displacement measurements. *Journal of Healthcare Engineering*, 2019:12, 2019.

[21] Herve Delingette and Nicholas Ayache. Hepatic surgery simulation. *Commun. ACM*, 48(2):31–36, 2005.

[22] Peter Deuflhard. *Newton Methods for Nonlinear Problems: Affine Invariance and Adaptive Algorithms*. Springer Publishing Company, Incorporated, 2011.

[23] Majid Abdouss Farzaneh Safshekan, Mohammad Tafazzoli-Shadpour and Mohammad B. Shadmehr. Mechanical characterization and constitutive modeling of human trachea: Age and gender dependency. *Materials*, 9:456, 2016.

[24] B. Ghali and S. Sirouspour. Nonlinear finite element-based modeling of soft-tissue cutting. In *IEEE Toronto International Conference Science and Technology for Humanity (TIC-STH)*, 2009.

[25] Antonio J. Gil. Structural analysis of prestressed saint venant?kirchhoff hyperelastic membranes subjected to moderate strains. *Computers & Structures*, 84(15):1012–1028, 2006.

[26] David J. Hawkes, P. J. Edwards, D. Barratt, J. M. Blackall, G. P. Penney, and C. Tanner. Measuring and modeling soft tissue deformation for image guided interventions. In Nicholas Ayache and Hervé Delingette, editors, *Surgery Simulation and Soft Tissue Modeling*, pages 1–14, Berlin, Heidelberg, 2003. Springer Berlin Heidelberg.

[27] Amir Hooshiar, Siamak Najarian, and Javad Dargahi. Haptic telerobotic cardiovascular intervention: A review of approaches, methods, and future perspectives. *IEEE Reviews in Biomedical Engineering*, 13:32–50, 2020.

[28] Alexandre Hostettler, Daniel George, Yves Rémond, Stéphane André Nicolau, Luc Soler, and Jacques Marescaux. Bulk modulus and volume variation measurement of the liver and the kidneys in vivo using abdominal kinetics during free breathing. *Computer Methods and Programs in Biomedicine*, 100(2):149–157, 2010.

[29] Wenguo Hou, Peter X. Liu, and Minhua Zheng. A new model of soft tissue with constraints for interactive surgical simulation. *Computer Methods and Programs in Biomedicine*, 175:35–43, 2019.

[30] Fabrice Jaillet. *Modélisation géométrique et simulation bio-mécanique des tissus mous*. Habilitation à diriger des recherches, Université Claude Bernard - Lyon 1, June 2011.

[31] Stian F. Johnsen, Zeike A. Taylor, Matthew J. Clarkson, John Hipwell, Marc Modat, Bjoern Eiben, Lianghao Han, Yipeng Hu, Thomy Mertzanidou, David J. Hawkes, and Sebastien Ourselin. NiftySim: A GPU-based nonlinear finite element package for simulation of soft tissue biomechanics. *International Journal of Computer Assisted Radiology and Surgery*, 10(7):1077–1095.

[32] Tolgay Kara and Ahmad Soliman Masri. Modeling and analysis of a visual feedback system to support efficient object grasping of an emg-controlled prosthetic hand. *Current Directions in Biomedical Engineering*, 5(1):207–210, 2019.

[33] Nam-Ho Kim. *Introduction to Nonlinear Finite Element Analysis*. Springer US, 2015.

[34] Roger Kneebone. Simulation in surgical training: Educational issues and practical implications. *Medical education*, 37:267–77, 2003.

[35] Przemyslaw Korzeniowski, Ruth White, and Fernando Bello. Vcsim3: a vr simulator for cardiovascular interventions. *International Journal of Computer Assisted Radiology and Surgery*, 13, 2017.

[36] Vasileios Lahanas, Constantinos Loukas, Konstantinos Georgiou, Hani Lababidi, and Dania Al-Jaroudi. Virtual reality-based assessment of basic laparoscopic skills using the leap motion controller. 31(12):5012–5023.

[37] M. Landsberg. L. v. kantorovich ? g. p. akilov, functional analysis in normed spaces. (international series of monographs in pure and applied mathematics, volume 46). *ZAMM - Journal of Applied Mathematics and Mechanics / Zeitschrift für Angewandte Mathematik und Mechanik*, 45(4):274–274, 1965.

[38] Patrick Le Tallec. Numerical methods for nonlinear three-dimensional elasticity. volume 3 of *Handbook of Numerical Analysis*, pages 465–622. Elsevier, 1994.

[39] Grégoire Lecerf and Joelle Saadé. A short survey on kantorovich: Like theorems for newton's method. *ACM Commun. Comput. Algebra*, 50(1):1–11, 2016.

[40] Taiwei Liu, Min Shen, Laixin Huang, Yaoqi Xiang, Hongxun Li, Yan Zhang, and Yan Wang. Characterization of hyperelastic mechanical properties for youth corneal anterior central stroma based on collagen fibril crimping constitutive model. *Journal of the Mechanical Behavior of Biomedical Materials*, 103:103575, 2020.

[41] Tiantian Liu, Sofien Bouaziz, and Ladislav Kavan. Quasi-newton methods for real-time simulation of hyperelastic materials. *ACM Trans. Graph.*, 36(3), 2017.

[42] Lapointe Marc-Olivier. *Évaluation des propriétés mécanique du tissu cardiaque par échocardiographie*. Phd thesis, 2016.

[43] Stephanie Marchesseau, Tobias Heimann, Simon Chatelin, Remy Willinger, and Herve Delingette. Fast porous visco-hyperelastic soft tissue model for surgery simulation: Application to liver surgery. 103(2):185–196.

[44] Felix Meister, T. Passerini, Viorel Mihalef, A. Tuysuzoglu, A. Maier, and Tommaso Mansi. Towards fast biomechanical modeling of soft tissue using neural networks. *arXiv: Quantitative Methods*, 2018.

[45] Philippe Mestat. Modèles d'éléments finis et problèmes de convergence en comportement non linéaire . Laboratoires des ponts et chaussées, 1998.

[46] Karol Miller, Grand R. Joldes, George Bourantas, Simon K. Warfield, Damon E. Hyde, Ron Kikinis, and Adam Wittek. Biomechanical modeling and computer simulation of the brain during neurosurgery. *International Journal for Numerical Methods in Biomedical Engineering*, 35(10):e3250, 2019. e3250 CNM-Mar-19-0110.R1.

[47] Nicolas Moës. *Mécanique des milieux continus*. Engineering school, Nantes, France, 2011.

[48] Sergei Nikolaev and Stéphane Cotin. Estimation of boundary conditions for patient-specific liver simulation during augmented surgery. *International Journal of Computer Assisted Radiology and Surgery*, 15:1107–1115, 2020.

[49] R. W. Ogden. *Nonlinear Elasticity, Anisotropy, Material Stability and Residual Stresses in Soft Tissue*, pages 65–108. Springer, Vienna, 2003.

[50] Shin'ichi Oishi. Numerical verification of existence and inclusion of solutions for nonlinear operator equations. *Journal of Computational and Applied Mathematics*, 60(1):171–185, June 1995.

[51] Yukio Oshiro and Nobuhiro Ohkohchi. Three-Dimensional Liver Surgery Simulation: Computer-Assisted Surgical Planning with Three-Dimensional Simulation Software and Three-Dimensional Printing. *Tissue Engineering Part A*, 23(11-12):474–480, 2017.

[52] Yukio Oshiro, Hiroaki Yano, Jun Mitani, Sangtae Kim, Jaejeong Kim, Kiyoshi Fukunaga, and Nobuhiro Ohkohchi. Novel 3-dimensional virtual hepatectomy simulation combined with real-time deformation. *World Journal of Gastroenterology : WJG*, 21(34):9982–9992, 2015.

[53] Hervé Oudin. Méthode des éléments finis. page 63, 2008.

[54] Zhigeng Pan, Adrian David Cheok, Hongwei Yang, Jiejie Zhu, and Jiaoying Shi. Virtual reality and mixed reality for virtual learning environments. *Computers & Graphics*, 30(1):20–28, 2006.

[55] Christoph J. Paulus, Nazim Haouchine, David Cazier, and Stéphane Cotin. Surgical Augmented Reality with Topological Changes. In *Medical Image Computing and Computer Assisted Interventions*, München, Germany, 2015.

[56] Oscar J. Pellicer-Valero, María José Rupérez, Sandra Martínez-Sanchis, and José D. Martín-Guerrero. Real-time biomechanical modeling of the liver using machine learning models trained on finite element method simulations. *Expert Systems with Applications*, 143:113083, 2020.

[57] Patrick Pessaux, Riccardo Memeo, Vito De Blasi, Didier Mutter, Luc Soler, and Jacques Marescaux. Réalité augmentée...une nouvelle ère pour la chirurgie hépatique *La Lettre de l'Hépato-gastroentérologue*, XIX(3), 2016.

[58] Igor Peterlík, Mert Sedef, Cagatay Basdogan, and Ludek Matyska. Real-time visio-haptic interaction with static soft tissue models having geometric and material nonlinearity. *Computers & Graphics*, 34(1):43–54, 2010.

[59] Karan Rangarajan, Heather Davis, and Philip H. Pucher. Systematic review of virtual haptics in surgical simulation: A valid educational tool? *Journal of Surgical Education*, 77(2):337–347, 2020.

[60] R.A.Tapia. The kantorovich theorem for newton's method. *Mathematical Association of America*, 1971(4), 2013.

[61] Da Ren, Yiming Chen, Bojun Lin, Fanjin Zeng, Jiaming Huang, and Jinfeng Wang. Modelling and Simulation of Vessel Surgery based on Mass-spring. *MATEC Web of Conferences*, 108:13004, 2017.

[62] Alexander Safar and L. Angela Mihai. The nonlinear elasticity of hyperelastic models for stretch-dominated cellular structures. *International Journal of Non-Linear Mechanics*, 106:144–154, 2018.

[63] Jean-Marc Schwartz. *Calcul Rapide De Forces Et De Déformations Mécaniques Non-Linéaires Et Visco-Élastiques Pour La Simulation De Chirurgie*. Phd thesis, Université Laval, 2003.

[64] Røtnes JS Seymour NE. Challenges to the development of complex virtual reality surgical simulations. *Surg Endosc*, 20(10), 2006.

[65] Srinivas C Tadepalli, Ahmet Erdemir, and Peter R Cavanagh. Comparison of hexahedral and tetrahedral elements in finite element analysis of the foot and footwear. *Journal of biomechanics*, 44(12):2337–2343, 2011.

[66] Akitoshi Takayasu and Shin'ichi Oishi. A method of computer assisted proof for nonlinear two-point boundary value problems using higher order finite elements. *Nonlinear Theory and Its Applications, IEICE*, 2(1):74–89, 2011.

[67] Daniel A. Tortorelli Tyler E. Bruns. Topology optimization of non-linear elastic structures and compliant mechanisms. *Comput. Methods Appl. Mech. Engrg*, 1999.

[68] O. V. D. van der Meijden and M. Schijven. The value of haptic feedback in conventional and robot-assisted minimal invasive surgery and virtual reality training: a current review. *Surgical Endoscopy*, 23:1180–1190, 2009.

[69] Rosanna Viglialoro, Nicola Esposito, Sara Condino, Fabrizio Cutolo, Simone Guadagni, Marco Gesi, Mauro Ferrari, and Vincenzo Ferrari. Augmented reality to improve surgical simulation. lessons learned towards the design of a hybrid laparoscopic simulator for cholecystectomy. *IEEE Transactions on Biomedical Engineering*, 66:1–1, 2018.

[70] Emanuele Vignali, Emanuele Gasparotti, Katia Capellini, Benigno Marco Fanni, Luigi Landini, Vincenzo Positano, and Simona Celi. Modeling biomechanical interaction between soft tissue and soft robotic instruments: importance of constitutive anisotropic hyperelastic formulations. *The International Journal of Robotics Research*, 40(1):224–235, 2021.

[71] Laurent Vigouroux. *Modélisation biomécanique des système musculo-squelettique sous déterminés. Analyse statique des tensions des tendons mobilisant le doigt*. Phd thesis, Université Joseph-Fourier - Grenoble I, 2005.

[72] Monan Wang, Zhiyong Mao, and Xianjun An. A fast computation method for soft tissue deformations simulation based on self-selection algorithm for embedded operating area. *Journal of Mechanics in Medicine and Biology*, 17(7):1740016.

[73] Xinhong Wang, Zhengzheng Yan, Yi Jiang, and Rongliang Chen. Efficient finite element hyperelasticity solver for blood vessel simulations. *Journal of Algorithms & Computational Technology*, 14:1748302620931014, 2020.

[74] Hujin Xie, Jialu Song, Yongmin Zhong, Jiankun Li, Chengfan Gu, and Kup-Sze Choi. Extended kalman filter nonlinear finite element method for nonlinear soft tissue deformation. *Computer Methods and Programs in Biomedicine*, 200:105828, 2021.

[75] Davide Zerbato and Diego Dall'Alba. Role of virtual simulation in surgical training. *Journal of Visualized Surgery*, 3, 2017.

[76] Z.GAO, K.LISTER, and JAYDEV P. DESAI. Constitutive modeling of liver tissue: Experiment and theory. *Annals of Biomedical Engineering*, 38(2):505–516, 2010.

[77] Jinao Zhang and Sunita Chauhan. Fast computation of soft tissue thermal response under deformation based on fast explicit dynamics finite element algorithm for surgical simulation. *Computer Methods and Programs in Biomedicine*, 187:105244, 2020.

[78] Jinao Zhang, Yongmin Zhong, and Chengfan Gu. Deformable models for surgical simulation: A survey. *IEEE Reviews in Biomedical Engineering*, 11:143–164, 11 2017.

[79] Jinao Zhang, Yongmin Zhong, and Chengfan Gu. Neural network modelling of soft tissue deformation for surgical simulation. *Artificial Intelligence in Medicine*, 97:61–70, 2019.

[80] Hualiang Zhong and Terry Peters. A real time hyperelastic tissue model. *Computer Methods in Biomechanics and Biomedical Engineering*, 10(3):185–193, 2007.